AUDITOR – GA 687367

Advanced Multi-Constellation EGNSS Augmentation and Monitoring Network and its Application in Precision Agriculture

D6.2 Version 1.2

First AUDITOR System Validation from RT preprocessed measurements

Contractual Date of Delivery: 31/12/2017

Actual Date of Delivery: 21/02/2018

Editor: Alberto García-Rigo, Manuel Hernández-Pajares, David Roma-Dollase (UPC) Jacobo Domínguez, Esther López, David Abia (ACORDE), Carles Fernández-Prades, Marc Majoral, Javier Arribas (CTTC)

Author(s): Manuel Hernández-Pajares, Alberto García-Rigo, David Roma-Dollase (UPC) Jacobo Domínguez, Esther López, David Abia (ACORDE), Carles Fernández-Prades, Marc Majoral, Javier Arribas (CTTC)

Work package: WP6 - Integration and validation.

Security: CONFIDENTIAL

Nature: Report

Version: 1.2

Total number of pages: 93

Abstract:

This report is focused on the validation process of the AUDITOR front-end, the software receiver as well as the Central Processing Facility of AUDITOR precise positioning corrections. In addition, results of likely the main elements of the full AUDITOR correction system (which is already working in RT conditions) both the Central Processing Facility at the SE Europe, around Greece, and two permanent receivers treated as roving users, with induced cold starts each 3 hours. The measurements, preprocessed in RT, are reprocessed with the same software to assess the impact of the WARTK technique and characterizing in detail the CPF functioning and user performance, confirming the advantages of the technique.

Document Control

Version	Details of Change	Author	Approved	Date
0.1	First draft	Manuel Hernández-Pajares, David Roma-Dollase, Alberto García-Rigo		2018-01-30
0.2	Second draft	Carles Fernández-Prades, Marc Majoral Javier Arribas		2018-02-06
0.3	Third draft	Jacobo Domínguez, Esther López, David Abia		2018-02-20
1.0	Consolidated version	Alberto García-Rigo		2018-02-20
1.1	Reviewed version DRS	Alberto García-Rigo, Jacobo Domínguez, Carles Fernández-Pradres		2018-06-05
1.2	Reviewed version DRS	Alberto García-Rigo, Jacobo Domínguez, Carles Fernández-Pradres		2018-06-19

Executive Summary

This report is focused on the validation process of the AUDITOR front-end - software receiver as well as the Central Processing Facility of AUDITOR precise positioning corrections. In addition, and results of likely the main elements of the full AUDITOR correction system (which is already working in RT conditions), both the Central Processing Facility at the SE Europe, around Greece, and two permanent receivers treated as roving users, with induced cold starts each 3 hours. The measurements, preprocessed in RT, are reprocessed with the same software to assess the impact of the WARTK technique and characterizing in detail the CPF functioning and user performance, confirming the advantages of the technique. Moreover, future updates of the system are envisaged, by implementing some of mitigation techniques on Medium Scale Travelling Ionospheric Disturbances developed by the UPC-IonSAT authors. In addition, the possibility to use RTKLIB at the user side for applying WARTK corrections is currently under development.

Authors

Partner	Name	e-mail
UPC	Manuel Hernández-Pajares	manuel.hernandez@upc.edu
	Alberto García Rigo	alberto.garcia.rigo@upc.edu
	David Roma Dollase	droma@el.ub.edu
ACORDE	Jacobo Domínguez	jacobo.dominguez@acorde.com
	Esther López	esther.lopez@acorde.com
	David Abia	david.abia@acorde.com
CTTC	Carles Fernández-Prades	carles.fernandez@cttc.es
	Marc Majoral	marc.majoral@cttc.es
	Javier Arribas	javier.arribas@cttc.es

Table of Contents

Document Control 2
Executive Summary 3
Authors 4
Table of Contents 5
List of tables 6
List of figures 7
List of Acronyms and Abbreviations 13
1 AUDITOR GNSS-SDR validation 14
1.1 General Overview 14
1.1.1 Overall architecture from D6.1 (public) 14
1.1.2 Front-end architecture (confidential) 15
1.2 Front-end validation (confidential) 18
1.2.1 Support Tools 19
1.2.1.1 Hardware tools 19
1.2.1.2 Software tools 20
1.2.2 RF measurements and adjustments 22
1.2.2.1 Modification of PLL / OL settings 23
1.2.2.2 Adaptation of oscillator 24
1.2.2.3 Removing of unneeded circuitry 24
1.2.3 RF measurements 24
1.2.3.1 S-parameters 24
1.2.3.2 LO phase noise 26
1.2.3.3 Power measurements in RF chain 26
1.2.3.4 BPSK measurements 28
1.2.3.5 Noise figure 30
1.3 Front-end and Software-receiver integration results (confidential) 32
1.3.1 Setup #1 32
1.3.1.1 Noise generated by the microcontroller 32
1.3.1.2 Outdoor captures 33
1.3.2 Setup #2 35
1.3.2.1 Outdoor captures 35
1.3.3 Setup #3 38
1.3.3.1 Outdoor captures 39
2 AUDITOR corrections validation 44
2.1 TOMION working in real-time at the Central Processing Facility side (public) 44
2.1.1 Real-time WARTK network, users and dates 44

2.1.2 Triple differences of prefit residuals 45
2.1.3 RT GPS satellite clocks estimated by the AUDITOR CPF vs the IGS ones 46
2.1.4 RT Zenith Tropospheric Delay estimated by the AUDITOR CPF vs the IGS ones 52
2.1.5 RT Vertical Total Electron Content (VTEC) estimated by the AUDITOR CPF vs the presently more accurate IGS GIM (UQRG) 54
2.1.6 RT VTEC model fitted independently for each satellite in view from the RT WARTK AUDITOR estimation (broadcasted as message DSM) 55
2.1.7 RT double-differenced carrier phase ambiguity fixing for the roving user AUT1 and for one typical permanent receiver (ORID) 63
2.1.8 RT 3D-positioning error for the roving users (AUT1 and PVOG) 66
2.1.9 Trying to clarify the reason of the temporarily WARTK worsening starting 43200 sec of day 358, 2017: Single Receiver MSTID Index and MSTID footprints 70
2.1.10 Reprocessing by mitigating the MSTID effect on the temporarily WARTK worsening starting 43200 sec of day 358, 2017, by means of a more exigent threshold for the estimated standard deviation of the computed ionospheric carrier phase ambiguity corresponding to the WARTK user 72
3 AUDITOR corrections dissemination 77
3.1 VTEC dissemination via RTCM 1264 77
3.1.1 Process overview 77
3.1.2 Implementation description 77
3.1.2.1 IONEX to RTNET processing 79
3.1.3 Execution 79
3.2 Study on RTCM 1264 messages (public) 80
3.2.1 Distribution of relative errors 82
3.3 DSM corrections / User observations dissemination via netcat 83
4 AUDITOR GNSS-SDR with RTKLIB integration validation 85
5 Conclusions 89
5.1 Conclusions on Front-end and Software-receiver validation (confidential) 89
5.2 Conclusions on AUDITOR corrections validation (public) 89
5.3 Conclusions on dissemination corrections and RTKLIB integration (public) 90
6 References 91
7 Appendix 92
7.1 Post-fit residuals for the roving user AUT1 and the reference receiver SOFI (public) 92

List of tables

Table 1-1 LO phase noise 26
Table 1-2 Summary of measurements in RF chain 27
Table 1-3 Comparison between original TCXO and replacement 39

Table 3-1 RMS relative error in function of the SH degree/order for UQRG VTEC in day of year 148, 2017 83
Table 4-1 Configuration options for PVT computation in GNSS-SDR 85

List of figures

Figure 1.1 :GNSS-SDR receiver 14
Figure 1.2 Architecture of 2nd version of the front-end 15
Figure 1.3 Front-end (2nd version) connected to Zedboard 16
Figure 1.4 Adapter board 16
Figure 1.5 Complete setup with adapter board 17
Figure 1.6 Adapter board with custom USB interface for long captures 20
Figure 1.7 Application for configuration of the front-end 21
Figure 1.8 Custom Windows application for USB captures 22
Figure 1.9 Evolution of PLL / OL settings for mitigation of spurious 24
Figure 1.10 S11 parameter of L2/L5 branch of the front-end 25
Figure 1.11 S11 parameter of final downconverter MAX2769 according to datasheet 25
Figure 1.12 S11 parameter of tri-band antenna 26
Figure 1.13 Baseband signal of a test carrier visualized in spectrum analizer 27
Figure 1.14 Processing of test carrier at L1 28
Figure 1.15 BPSK decoded affter the first downconversion stage for L2 29
Figure 1.16 BPSK in baseband (IF=1MHz) after digitalization at the output of the front-end 29
Figure 1.17 Noise figure and gain of L2 band 30
Figure 1.18 Noise figure and gain of L5 band 30
Figure 1.19 Noise generated by the microcontroller 32
Figure 1.20 Noise generated by the microcontroller 33
Figure 1.21 Setup for outdoor tests 34
Figure 1.22 Architecture of 2nd version of the front-end (setup #2) 35
Figure 1.23 PVT results obtained with GNSS-SDR after processing a L1 band capture 37
Figure 1.24 Architecture of 2nd version of the front-end (setup #3) 38
Figure 1.25 Additional board utilized for external TCXO 38
Figure 1.26 Tracking example in L2 band with GNSS-SDR processing 40
Figure 1.27 Tracking of L2 satellite with configuration #05 42
Figure 2.1 Map of the AUDITOR RT permanent GPS stations (green squares), including the reference one (red square) and permanent GPS receivers treated as rover users (magenta circles). 44
Figure 2.2 Number of continuous arc transmitter-receiver vs time, for the reference GPS receiver SOFI (first row) and for one of the roving users, AUT1 (second row), during the first

(starting-up), second and third, and last, days of this RT experiment (days 23, 24 and 25 December 2017, respectively)..... 45

Figure 2.3 Triple differences of ionospheric-free combination of carrier phases for the permanent receiver ORID, vs elevation (first row) and vs time (second row), during the first (starting-up), second and third, and last, days of this RT experiment (days 23, 24 and 25 December 2017, respectively)..... 46

Figure 2.4 Triple differences of ionospheric-free combination of carrier phases for the roving user AUT1, versus elevation (first row) and versus time (second row), during the first (starting-up), second and third, and last, days of this RT experiment (days 23, 24 and 25 December 2017, respectively)..... 46

Figure 2.5 Satellite clock offsets for GPS satellites (PRN01, 02, 03, 05, 06 and 07 from left to right and from top to bottom) estimated by the CPF for the different satellites in view (green points) versus the final values computed and combined in post-processed by IGS analysis centers. during the second day of this RT experiment (day 24 December 2017)..... 47

Figure 2.6 Satellite clock offsets for GPS satellites (PRN08, 09, 10, 11, 12 and 13 from left to right and from top to bottom) estimated by the CPF for the different satellites in view (green points) versus the final values computed and combined in post-processed by IGS analysis centers. during the second day of this RT experiment (day 24 December 2017)..... 48

Figure 2.7 Satellite clock offsets for GPS satellites (PRN14, 15, 16, 17, 18 and 19 from left to right and from top to bottom) estimated by the CPF for the different satellites in view (green points) versus the final values computed and combined in post-processed by IGS analysis centers. during the second day of this RT experiment (day 24 December 2017)..... 49

Figure 2.8 Satellite clock offsets for GPS satellites (PRN20, 21, 22, 23, 24 and 25 from left to right and from top to bottom) estimated by the CPF for the different satellites in view (green points) versus the final values computed and combined in post-processed by IGS analysis centers. during the second day of this RT experiment (day 24 December 2017)..... 50

Figure 2.9 Satellite clock offsets for GPS satellites (PRN26, 27, 28, 29, 30 and 31 from left to right and from top to bottom) estimated by the CPF for the different satellites in view (green points) versus the final values computed and combined in post-processed by IGS analysis centers. during the second day of this RT experiment (day 24 December 2017)..... 51

Figure 2.10 Satellite clock offsets for GPS satellites (PRN32 from left to right and from top to bottom) estimated by the CPF for the different satellites in view (green points) versus the final values computed and combined in post-processed by IGS analysis centers. during the second day of this RT experiment (day 24 December 2017)..... 52

Figure 2.11 Zenith Tropospheric Delay estimated in RT by the AUDITOR CPF (red) for permanent receivers with available final IGS estimation (blue), from left to right and from top to bottom the receivers ISTA, MATE, ORID and SOFI, during the second day of this RT experiment (24 December 2017). 53

Figure 2.12 Zenith Tropospheric Delay estimated in RT by the WARTK users of AUDITOR, AUT1 (left) and PVOG (right), during the second day of this RT experiment (day 24 December 2017). 53

Figure 2.13 In the left-hand plot the VTEC estimated in RT by the CPF (vertical axis) vs the reference value provided by the post-processed Global Ionospheric Map (GIM) UQRG (horizontal axis, both in meters of LI=L1-L2) is represented, and the corresponding time evolution (in green and red, respectively) is shown at the right-hand plot, both during the second day of this RT experiment (day 24 December 2017). 54

Figure 2.14 STEC estimated in RT by the CPF (vertical axis in meters of LI=L1-L2) vs time (horizontal axis in modified julian days) is represented, during the whole RT experiment (days 23, 24 and 25 December 2017). 55

Figure 2.15 STEC estimated in RT by the CPF (vertical axis in meters of LI=L1-L2) vs elevation angle above the horizon (horizontal axis in degrees) is represented, during the whole RT experiment (days 23, 24 and 25 December 2017). 55

Figure 2.16 The bias of the residuals of the VTEC fitting per satellite (vertical axis in meters of LI=L1-L2) vs time (horizontal axis in seconds of the day) is represented, during the second day of the RT experiment (day 24 December 2017). 56

Figure 2.17 The RMS of the residuals of the VTEC fitting per satellite (vertical axis in meters of LI=L1-L2) vs time (horizontal axis in seconds of the day) is represented, during the second day of the RT experiment (day 24 December 2017). 56

Figure 2.18 Residuals of the VTEC fitting per satellite (vertical axis in meters of LI=L1-L2) vs time (horizontal axis in seconds of the day) is represented, during the second day of the RT experiment (day 24 December 2017). 57

Figure 2.19 Coefficients of the VTEC fitting per satellite (vertical axis) vs time (horizontal axis in seconds of the day) is represented, from left to right and from top to bottom, for satellites PRN01, 02, 03, 05, 06 and 07, during the second day of the RT experiment (day 24 December 2017). 58

Figure 2.20 Coefficients of the VTEC fitting per satellite (vertical axis) vs time (horizontal axis in seconds of the day) is represented, from left to right and from top to bottom, for satellites PRN08, 09, 10, 11, 12 and 13, during the second day of the RT experiment (day 24 December 2017). 59

Figure 2.21 Coefficients of the VTEC fitting per satellite (vertical axis) vs time (horizontal axis in seconds of the day) is represented, from left to right and from top to bottom, for satellites PRN14, 15, 16, 17, 18 and 19, during the second day of the RT experiment (day 24 December 2017). 60

Figure 2.22 Coefficients of the VTEC fitting per satellite (vertical axis) vs time (horizontal axis in seconds of the day) is represented, from left to right and from top to bottom, for satellites PRN20, 21, 22, 23, 24 and 25, during the second day of the RT experiment (day 24 December 2017). 61

Figure 2.23 Coefficients of the VTEC fitting per satellite (vertical axis) vs time (horizontal axis in seconds of the day) is represented, from left to right and from top to bottom, for

satellites PRN26, 27, 28, 29, 30 and 31, during the second day of the RT experiment (day 24 December 2017). 62

Figure 2.24 Coefficients of the VTEC fitting per satellite (vertical axis) vs time (horizontal axis in seconds of the day) is represented, from left to right and from top to bottom, for satellite PRN32, during the second day of the RT experiment (day 24 December 2017)..... 63

Figure 2.25 PRN of the GPS reference satellite selected in RT to form the double differences (the one available with maximum elevation seen from the reference receiver SOFI) versus time during the second day of the RT experiment (day 24 December 2017). 63

Figure 2.26 Double differenced widelane ambiguity, derived from the ionospheric-free and geometric-free double-differenced ambiguities, versus the value provided by the double-differenced ionospheric and geometric-free Melbourne-Wübbena combination, in cycles: left-hand plot correspond to the roving receiver AUT1 and the right-hand plot to the permanent receiver ORID, both during the second day of the RT experiment (day 24 December 2017). 64

Figure 2.27 Difference of the double differenced widelane ambiguity, derived from the ionospheric-free and geometric-free double-differenced ambiguities, minus the value provided by the double-differenced ionospheric and geometric-free Melbourne-Wübbena combination, in cycles, versus elevation angle: left-hand plot correspond to the roving receiver AUT1 and the right-hand plot to the permanent receiver ORID, both during the second day of the RT experiment (day 24 December 2017)..... 64

Figure 2.28 Difference of the double differenced widelane ambiguity, derived from the ionospheric-free and geometric-free double-differenced ambiguities, minus the value provided by the double-differenced ionospheric and geometric-free Melbourne-Wübbena combination, in cycles, versus time: left-hand plot correspond to the roving receiver AUT1 and the right-hand plot to the permanent receiver ORID, both during the second day of the RT experiment (day 24 December 2017)..... 65

Figure 2.29 Percentage of RT double differenced carrier phase ambiguity fixing (widelane in green, narrowlane in red), and number of available double-differences (in magenta) are represented versus time: left-hand plot correspond to the roving receiver AUT1 and the right-hand plot to the permanent receiver ORID, both during the second day of the RT experiment (day 24 December 2017). 65

Figure 2.30 3D RT positioning error of the WARTK (i.e. fixing wide- and narrow-lane ambiguities) roving GPS receivers AUT1 (first column) and PVOG (second column) during the overall Christmas days experiment (days 23, 24 and 25 December 2017, in first, second and third row respectively). 67

Figure 2.31 3D RT carrier-phase based differential positioning error (i.e. no fixing carrier phase ambiguities) for the roving GPS receivers AUT1 (first column) and PVOG (second column) during the overall Christmas days experiment (days 23, 24 and 25 December 2017, in first, second and third row respectively)..... 68

Figure 2.32 3D RT carrier-phase based differential positioning error (i.e. fixing wide- and narrow-lane ambiguities, with higher requirements of bias error estimates to fix both double-

differences) for the roving GPS receivers AUT1 (first column) and PVOG (second column) during the overall Christmas days experiment (days 23, 24 and 25 December 2017, in first, second and third row respectively)..... 69

Figure 2.33 3D RT positioning error for roving receiver AUT1 with WARTK (i.e. constraining the wide- and narrow-lane ambiguities with the ionospheric corrections, left) and without ionospheric corrections, i.e. without constraining the ambiguities (right), during the overall Christmas days experiment (days 23, 24 and 25 December 2017). 70

Figure 2.34 3D RT positioning error for roving receiver PVOG with WARTK (i.e. constraining the wide- and narrow-lane ambiguities with the ionospheric corrections, left) and without ionospheric corrections, i.e. without constraining the ambiguities (right), during the overall Christmas days experiment (days 23, 24 and 25 December 2017). 70

Figure 2.35 Single Receiver MSTID Index for roving receiver AUT1, versus time in Julian days for the overall RT experiment (left-hand plot) and versus seconds of day 358, 2017 (central day of the RT experiment). 71

Figure 2.36 Zoom of Li=L1-L2 carrier phase measurements in length units for satellite PRN07 and PRN30 taken from receivers AUT1 and SOFI during 24 December, 2017. 71

Figure 2.37 The RMS of the residuals of the VTEC fitting per satellite (vertical axis in meters of LI=L1-L2) vs time (horizontal axis in seconds of the day) is represented, during the second day of the RT experiment (day 24 December 2017), with the initial set of thresholds for user carrier phase ambiguity fixing (left) and with a more exigent one (right). 72

Figure 2.38 Residuals of the VTEC fitting per satellite (vertical axis in meters of LI=L1-L2) vs time (horizontal axis in seconds of the day) is represented, during the second day of the RT experiment (day 24 December 2017), with the initial set of thresholds for user carrier phase ambiguity fixing (left) and with a more exigent one (right). 73

Figure 2.39 3D RT positioning error of the WARTK (i.e. fixing wide- and narrow-lane ambiguities) roving GPS receivers for AUT1 with previous threshold for ambiguity fixing (first column) and with the most exigent one (second column) during the overall Christmas days experiment (days 23, 24 and 25 December 2017, in first, second and third row respectively). 74

Figure 2.40 3D RT positioning error of the WARTK (i.e. fixing wide- and narrow-lane ambiguities) roving GPS receivers for AUT1 with previous threshold for ambiguity fixing (first column) and with the most exigent one (second column) during the overall Christmas days experiment (days 23, 24 and 25 December 2017, in first, second and third row respectively). 75

Figure 2.41 3D RT positioning error for roving receiver AUT1 (first column) and PVOG (second column), without ionospheric corrections i.e. without constraining the ambiguities (first row), with WARTK (i.e. constraining the wide- and narrow-lane ambiguities with the ionospheric corrections) in second row (former threshold for widelane and narrowlane ambiguity fixing) and in third row (for new more exigent ambiguity fixing

thresholds), during the overall Christmas days experiment (days 23, 24 and 25 December 2017). 76

Figure 2.42 Post-fit residual for the ionospheric combination of the pseudoranges corresponding to the roving receiver AUT1 (first column) and the reference receiver SOFI (second column), versus time (first row) and versus elevation (second row), during day 25 December 2017. 76

Figure 3.1 VTEC dissemination flow chart 77

Figure 3.2: Configuration used in the implementation of the VTEC dissemination 78

Figure 3.3 IONEX to BNC RTNET flow chart 79

Figure 3.4 SNIP Caster used for testing the VTEC dissemination distributing URTG GIMs uninterruptedly for more than 10 days 80

Figure 3.5 Original UQRG 15-minute VTEC GIM (UQRG1480.17i, 00UT) 81

Figure 3.6 Reconstructed UQRG GIM considering SH of degree 8 and order 8, of day of year 148, 2017. Accounting for 13% RMS relative error. 81

Figure 3.7 Reconstructed UQRG GIM considering SH of degree 16 and order 16, of day of year 148, 2017. Accounting for 5.8% RMS relative error. 82

Figure 3.8 Reconstructed UQRG GIM considering SH of degree 64 and order 32, of day of year 148, 2017. Accounting for 1.8% RMS relative error. 82

Figure 7.1 Post-fit residual for the Melbourne-Wübbena combination corresponding to the roving receiver AUT1 (first column) and the reference receiver SOFI (second column), versus time (first row) and versus elevation (second row), during day 25 December 2017. 92

Figure 7.2 Post-fit residual for the ionospheric-free combination of the carrier phases corresponding to the roving receiver AUT1 (first column) and the reference receiver SOFI (second column), versus time (first row) and versus elevation (second row), during day 25 December 2017. 93

Figure 7.3 Post-fit residual for the ionospheric-free combination of the pseudoranges corresponding to the roving receiver AUT1 (first column) and the reference receiver SOFI (second column), versus time (first row) and versus elevation (second row), during day 25 December 2017. 94

Figure 7.4 Post-fit residual for the ionospheric combination of the carrier phases corresponding to the roving receiver AUT1 (first column) and the reference receiver SOFI (second column), versus time (first row) and versus elevation (second row), during day 25 December 2017. 95

List of Acronyms and Abbreviations

Term	Description
BNC	BKG Ntrip Client
BS	B-spline
CPF	Central Processing Facility
dSTEC	Differential STEC
FE	Front-End
GIM	Global Ionospheric Maps
GNSS	Global Navigation Satellite System
GUI	Graphical User Interface
KPI	Key Performance Indicator
MSTID	Medium Scale TID
NABS	Non-uniform Adaptive B-splines
NTRIP	Network Transport RTCM via Internet Protocol
PVT	Position-Velocity-Time
RMS	Root Mean Square
RT	Real Time
RTK	Real Time Kinematic
SH	Spherical Harmonic
SSR	RTCM's State Space Representation
STEC	Slant TEC
SW	Software
TEC	Total Electron Content
TID	Travelling Ionospheric Disturbance
TOMION	TOmographic Model of the IONosphere
UPC	Universitat Politècnica de Catalunya
VTEC	Vertical TEC
WARTK	Wide Area RTK
ZTD	Zenith Tropospheric Delays

1 AUDITOR GNSS-SDR validation

1.1 General Overview

1.1.1 Overall architecture from D6.1 (public)

Figure 1.1, presented in D6.1 [1], depicts the architecture of the RF Front-End (FE) and the full GNSS-SDR receiver.

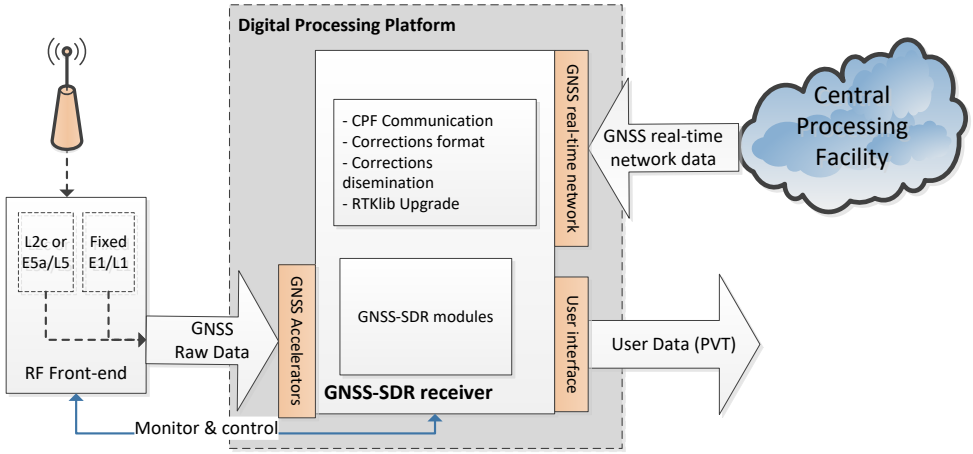

Figure 1.1 :GNSS-SDR receiver

As stated in D6.1 [1], the workflow of signal is:

- The **GNSS-SDR receiver** acquires the GNSS Raw data (L1, L2c or L5) **through the FE**.
- The GNSS-SDR receiver consumes the **CPF** real-time network data in order to obtain and take into account the iBOGART corrections information.
- The final PVT information needs to be calculated and provided to the end user.

Two versions of the FE have been designed, manufactured and tested v1.0 and v2.0. Taking into account the software-defined radio implementation of the presented GNSS receiver, the validation of the FE is tightly coupled to the GNSS-SDR baseband processing.

Early validation of the FE v2.0, while the GNSS-SDR real-time accelerators for the proposed bands (E1/L1, L2C, E5a/L5) were being implemented and tested, was possible thanks to initial Linux implementation of the GNSS-SDR software that could process FE measurements in an offline model with a standard computer. In this section the activities related to this early validation of the FE are presented.

The full GNSS-SDR receiver implementation details and validation tests will be included in D3.2/D3.3 ([3]/[4]) were more details about the integration of the final FE and real-time GNSS-SDR are included.

In D3.1 [2] an initial RF assessment of v1.0 was detailed. This assessment lead to the upgrades implemented in v2.0 which was manufactured at the time of D3.1[2] submission.

1.1.2 Front-end architecture (confidential)

FE v2.0 consists of a dedicated branch for E1/L1 band and another dedicated branch for L2 or L5/E5a band as show in Figure 1.2. The optional bands in the second branch share the RF path and the appropriate filter for each case is selected by means of 2 multiplexers.

A microcontroller is devoted to the configuration of the different elements if the FE and implements the custom AGC. It also monitors the system for detecting alarms mainly related to the different PLLs status (locked/not locked).

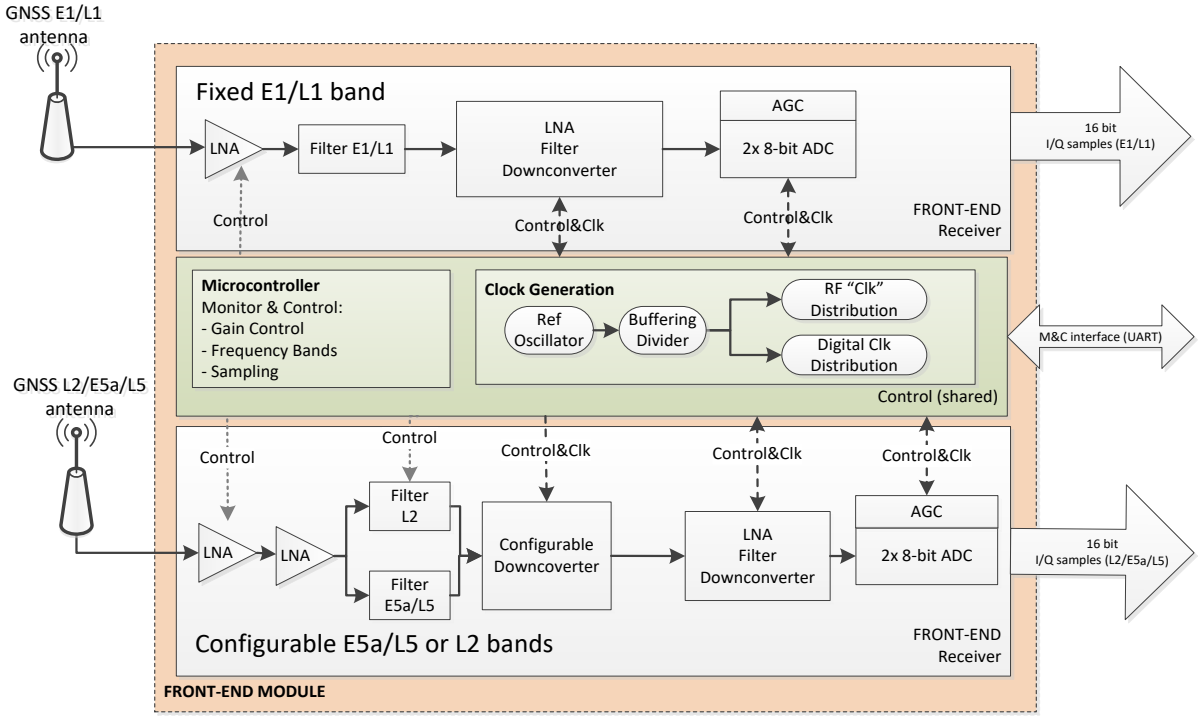

Figure 1.2 Architecture of 2nd version of the front-end

The GNSS-SDR accelerators and embedded SDR Linux receiver are hosted in a Zynq-based board. The ZedBoard is the reference Zynq-based board selected. Figure 1.3 shows the original concept of FE v2.0 presented in D3.1 now manufactured, directly plugged to the reference ZedBoard. In this picture, both the front-end, the development board and the tri-band antenna (with the ground plane provided by its manufacturer) are shown.

Several PCB units of the FE v2.0 were manufactured, while only three where fully mounted and tested in the laboratory with different configurations.

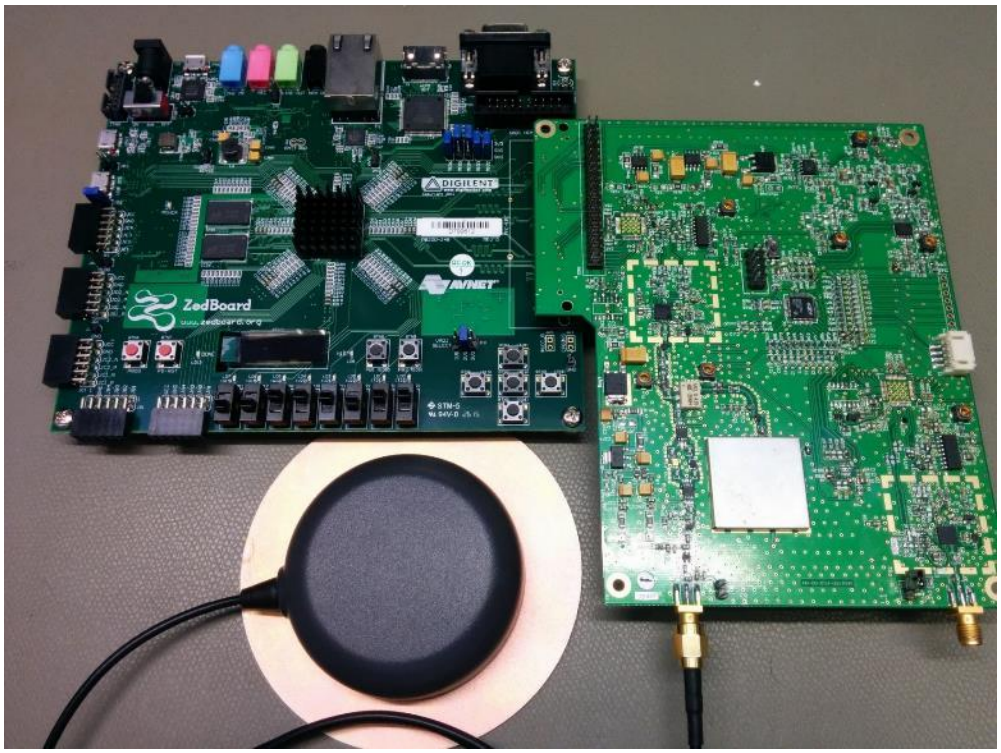

Figure 1.3 Front-end (2nd version) connected to Zedboard

In the initial ZedBoard integration and evaluation of high performance Zynq-based boards, such as the Zynq ZC706, which offer an FMC standard connector, an additional FE requirement to offer lower level voltages was identified. Therefore, in order to add more flexibility to the FE design and adapt its voltage levels to the lower FMC standard, a small adapter board was designed and assembled.

Figure 1.4 Adapter board

This adapter not only provides the required FMC voltage levels but also integrates an on-chip digital to USB capturer to ease the offline validation of the FE. Several support activities were required to properly capture the FE baseband signal to feed the GNSS-SDR Linux receiver and provide an end-to-end receiver validation. Figure 1.5 shows the final setup, including the adapter board

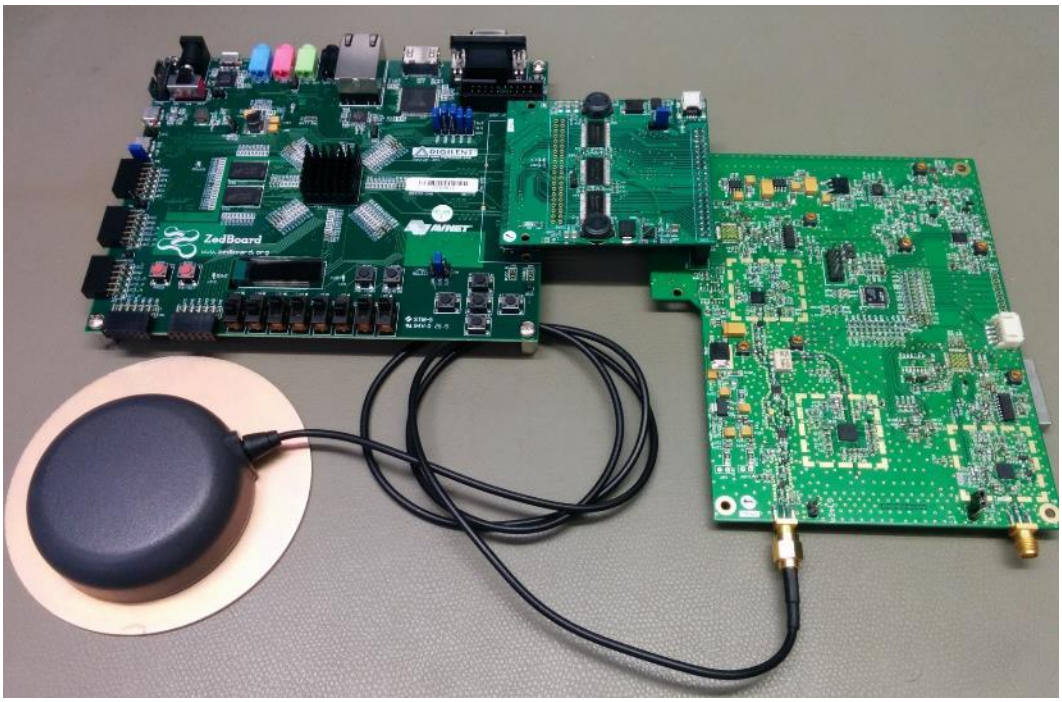

Figure 1.5 Complete setup with adapter board

This full setup was modified during the tests and validation phase, in order to correct and improve the performance of the front-end. Thus, 3 different setups were actually tested during this phase, which are detailed in the next sections devoted to the FE validation with the GNSS-receiver.

1.2 Front-end validation (confidential)

In order to validate the FE, the following test were performed:

- RF components laboratory tests: evaluation of the phase noise of the LO and the main parameters of the RF chain components (power levels, clock signals levels, proper grounding and DC voltages).
- RF end-to-end validation laboratory tests: evaluation of the system performance with both pure carrier and BPSK signals.
- RF end-to-end validation output tests: outdoor captures with GNSS signals in open sky and validation with offline GNSS-SDR post-processing.

The following sections detail the tools utilized during the tests, including the laboratory equipment and custom hardware designed as well as the firmware/software developed for executing and processing the captures. The use and implementation of these tools was an additional challenge considering the different possible configurations of the FE to test and the high raw data throughput that can be generated.

The data throughput for an I/Q 8-bits capture sampled at 13MHz leads to a minimum data stream of 2*8*13MHz = 208Mbits for a single channel. This high throughput implies that an USB 2.0 standard interface (200Mbits) can be easily overflow and disk logging needs to be performed using more aggressive techniques, i.e. heavy volatile buffering, burst optimizations, higher priorities processes…. Moreover, a 60 seconds raw data capture will require ~1.5GB of high performance memory, if data is optimally packed, which is not always possible depending on the acquisition tools and the need performance optimizations to achieve ~200Mbits in a regular laptop computer (for outdoor measurements).

For several minutes, the required memory size and raw data stream could be easily prohibitive for regular computers. Therefore, for practical measurements and post-processing analysis several reductions need to be applied in order to minimize the raw data stream and ease the post-processing activities without compromising the validity of the analysis. The more direct strategies adopted, and their effect of the validation are:

- Sampling one channel only: assumes independent analysis of both channels that could be correct for the baseband generation but need to be further study to identify RF interferences between channels.
- Reducing bits per sample (using 2-bits): it reduces the actual performance of the receiver; however, 2-bits is an accepted valid value used in commercial GNSS receivers.
- Reducing sampling frequency to other multiples Clock/2, Clock/3…: depends heavily on the band analyzed, narrow bandwidths may affect negatively in the performance, in the case of E5a/L5 there is not much margin for reduction. In L2 is possible to reduce the sampling frequency to 26/3MHz, 26/4 MHz without compromising the validation.
- Reducing capture time: reduces the maximum signal length which is easier to manipulate but impacts the length of the processing. One minute is a good tradeoff between capture size and data length to be able to lock to multiple satellites, keep tracking and receive at least one subframe. In order to estimate PVT and better asses the receiver performance several minutes are desirable, moreover for the final validation continuous 24-hours runs need to be analyzed, this is only possible with the GNSS-SDR real-time implementation.

While the procedures described in the next sections are applicable to both L1/E1 and L2C|E5a/L5 band, the descriptions are focused on the L2C|E5a/L5 bands due to its higher complexity in terms of the implemented receiver architecture.

1.2.1 Support Tools

1.2.1.1 Hardware tools

The following standard laboratory equipment were utilized for testing RF and digital parameters:

- Spectrum analyzer with phase noise and NF add-ons.
- Digital Oscilloscope
- Logic analyzer
- Vector signal generator
- Vector signal analyzer
- Network analyzer

Due to the high raw data bandwidth and memory constraints, to collect more than a few seconds of data, custom solutions were implemented that enabled long outdoor captures.

Three different hardware setups were used to capture the FE raw data:

- ZedBoard.
- Logic Analyzer.
- Custom USB adapter with on-chip capturer.

1.2.1.1.1 ZedBoard

The ZedBoard (with logging software provided by CTTC) can be used to perform captures up to several dozens of seconds, with some restrictions in bandwidth that affect the maximum sampling frequency supported (max ~8MHz). This was the initial capture method that offered early evaluation of the FE raw data while also evaluating the actual ZedBoard interface via the FMC connector that is also used by the real-time implementation of the GNSS-SDR.

1.2.1.1.2 Logic Analyzer

Several commercial logic analyzers were used to assess the quality of the digital signals in the FE interface:

- 1680A Logic Analyzer from Agilent (older model)
- 16862A 68-Channel Portable Logic Analyzer (provided by Agilent free of charge during the tests).

These analyzers enabled to evaluate the correctness of timing and voltage levels for digital signals, however these equipments are more targeting to analyze multiple high frequency digital signals than long captures scenarios. Due to its internal memory size limitation it was not possible to capture of more than 30-40 seconds of raw GNSS data with the newer model.

1.2.1.1.3 USB interface of the adapted board

The design of the adapter board also included a custom USB interface based on a dedicated microcontroller that makes possible to perform captures using a laptop to store the data (the only

restriction for the size of the data collected is the available computer memory). This custom board allows performing longer captures and using higher sampling frequencies (~13MHz) which are required for the validation of the L2C|E5a/L5 band.

The front-end can be directly powered from the adapter board, which can be fed by a 12V battery for outdoor testing. Both boards are shown in Figure 1.6.

Figure 1.6 Adapter board with custom USB interface for long captures

1.2.1.2 Software tools

In order to support the testing and validation activities in an agile way, several software/firmware tools were developed that monitor and control the different IC (downconverters, oscillator, microcontroller with AGC control…) in the FE and also adapt the captured baseband signal for offline post-processing with the GNSS-SDR.

1.2.1.2.1 Utility for configuration of the front-end

A custom application for configuration of the downconverters of the front-end was developed in order to test quickly multiple configuration options and evaluate their performance tradeoffs. Thus, different configurations could be easily loaded and tested on the fly.

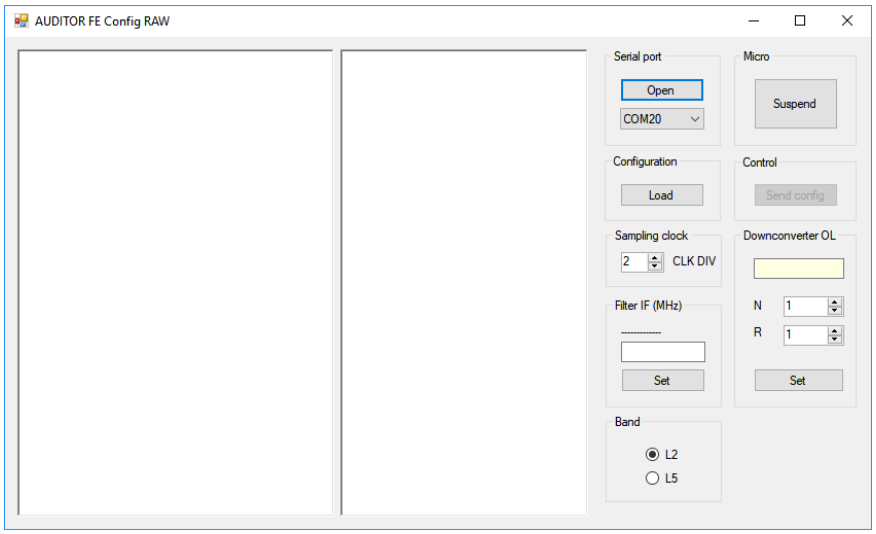

Figure 1.7 Application for configuration of the front-end

The application allows, on one side, to load complete configurations of all elements of the front-end, and on the other side, to modify certain parameters of a previously loaded configuration for fine adjustment (like the final downconverter PLL configuration, filter IF or sampling clock divider) to compare multiple settings performance.

1.2.1.2.2 Utility for USB adapter capturer

The developed custom USB adapter that integrates an embedded capturer is used from a standard computer using a custom software that was developed within this project:

- A custom firmware for the dedicated microcontroller in charge of sampling the IQ output of the front-end and sending it through USB.
- A Windows console application for acquiring and storing the data.

An example of a short capture performed using the USB interface is shown in Figure 1.8.

```
C:\usb>usbfeapp.exe
GNSS FE USB application by ACORDE (APPLICATION = 0.3.4, LIBRARY = 0.3.7)

Application set to HIGH_PRIORITY_CLASS
   [device_start] ERROR: VID=04B4 | PID=1003 not found!
   [device_start] trying to load firmware.........................loaded
   [device_start] VID 04B4 | PID 1003 found
:> help
------------------------------------------------------------
[h] Help
[q] Quit
[0] Capture data into an interleaved IQ file
[1] Infinite loop test
[e] Enable ethernet
   [ethernet_start] control port = 966, data port = 967, agc port = 968
   [ethernet_start] WSAStartup OK
   [control_thread_start]
   [data_thread_start]
thread_control: running...
   [agc_info_thread_start]
   [thread_data] running...
   [agc_info_thread] running...
:> 0
Enter capture length (milliseconds):>2000
Capture configuration: id_frequency = 0 length = 2000 ms
Application set to REALTIME_PRIORITY_CLASS
   [device_get_data] target size = 2000 ms --> 26000000 bytes
   [device_get_data] size of capture will be of 24 MB
   [device_get_data] aqcuiring data...
   [device_get_data] 26000000 bytes are allocated
   [stream_configure] interface=0
   [stream_configure] endpoint=82
   [stream_configure] PPX=128
   [stream_transfer_loop] transfer size = 65536 bytes
   [stream_transfer_loop] 13.238 MB in 1.031 s (102.722 Mbits/s)
   [stream_show_stats] 90 Mbits/s | 396 success | 0 error
Application set to HIGH_PRIORITY_CLASS
<save> dumping data into 'data_20180214_101204.log'...done
Capture finished
:> :>
```

Figure 1.8 Custom Windows application for USB captures

The validation of the USB capture method was done by generating cyclic pseudorandom sequences with known seeds e.g. PRBS9, during several seconds and comparing the captured data afterwards. This allows to verify the integrity of the data collected for multiple clock frequencies, by confirming that no data is lost during the transfer a therefore in this digital process there are not bit errors.

1.2.1.2.3 Utility for 2-bit to IQ file conversion

In case of using an output with 2 bits instead of the original 8 bits, the capture must be pre-processed using a custom console application that converts it to an equivalent interleaved IQ format. This format is one of the source data options of the GNSS-SDR implementation, so the data can be directly feed without additional transformations for its post-processing.

1.2.2 RF measurements and adjustments

The laboratory and outdoor measurements allowed to identify the main issues that need to be solved. Several measurements were performed in the following section, where only the most relevant analyses and adjustments are summarized; they can be divided in the following areas:

- PLL/OL configuration: there are three phase-locked loops (PLLs) that need to be configurable in the FE to provide the main local oscillators (OL), one for L1 band and two for the L2C|E5a/L5 band. For each PLL there are many parameters that could lead to a similar frequency plan,

however many of this configuration causes in-band interference spurious that need to be avoided. These frequencies and the oscillators power need to be carefully selected to minimize the in-band interferences.

- RF Parameters:
    - Small signal analysis (S-Parameters): basic antenna and RF chain S-parameters are measured to evaluate their power adaptation. This can be easily compared to the commercial L1 downconverter IC performance.
    - Phase Noise: phase noise is an important parameter in GNSS SDR receivers as they do not have a hardware loop to lock the RF oscillators to the received carrier and perform most of their phase locking operations in the software domain. Therefore, a good phase noise performance is even more important than in non-SDR GNSS receivers.
    - Power/Gain balance: due to the low power levels of the GNSS signal a proper power balance need to be achieve. Particularly for the L2C|E5a/L5 band, this need to be tested for each RF component and the RF/LO signals, to check that the components are working in their nominal region while the proper gain in the needed RF band.
    - Noise figure (NF): the low GNSS signal levels requires to minimize as much as possible the receiver impact in the already low signal-to-noise ratio (SNR). This is already analyzed in the design phase mainly by selecting low noise amplifiers and a GNSS active antenna that offers low NF values.

Regarding the input signals that can serve as base to perform the system validation, they can be summarized as:

- Single tone: a single tone analysis is a quick a very convenient to evaluate the correctness of the frequency plan and power levels in different points of the RF chain. Moreover, a linear frequency sweep in a given band could quickly provide a good overview of possible receiver issues in a given band.
- Digital Modulation: to better evaluate the receiver response to wide band signals (similar to GNSS signals) without the full complexity of GNSS signals, BPSK modulated signals have been used with different data sequences and bandwidths, to analyze power and phase issues. This could only be evaluated for higher power levels than the average GNSS signal as the spectrum was not de-spread
- Thermal noise: using as input the thermal noise provided by a 50 ohm load as input signal.
- Outdoor antenna measure: using a triple-band active antenna ~35dB gain with the actual GNSS signal, which required an offline post-processing phase using the GNSS-SDR software.

1.2.2.1 Modification of PLL / OL settings

The modification of the PLL settings and the different OLs in the front-end, intend to displace the harmonics and spurious out of the band of interest and filter them as much as possible, to avoid affecting the AGC and later baseband processing.

To illustrate the importance of a good configuration of the PLL/OL downconverters,

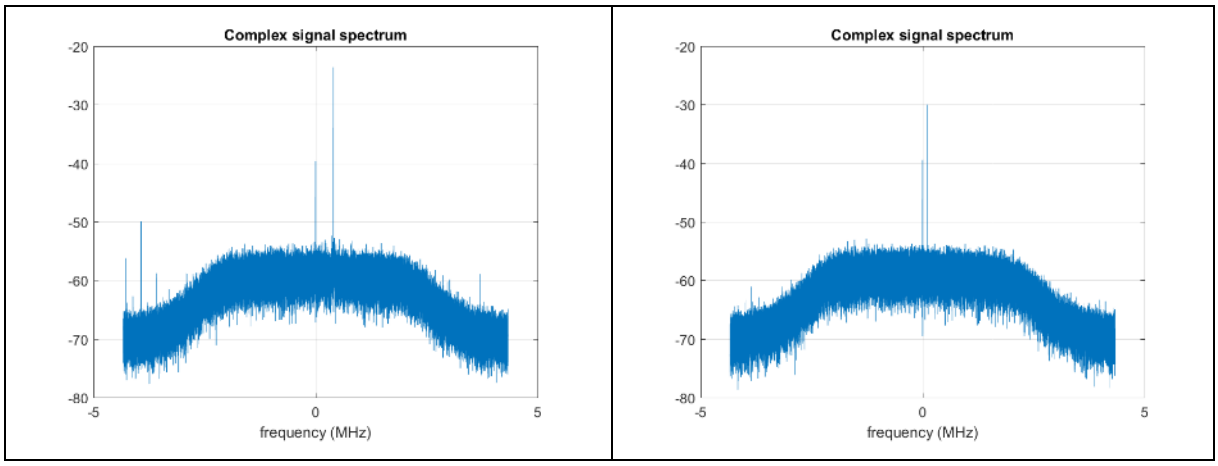

Figure 1.9 shows multiple configurations of the PLL/OL and their effect on the output spectrum. A single tone at the center of L2 is introduced, for each PLL/OL configuration tested the final IF is slightly modified.

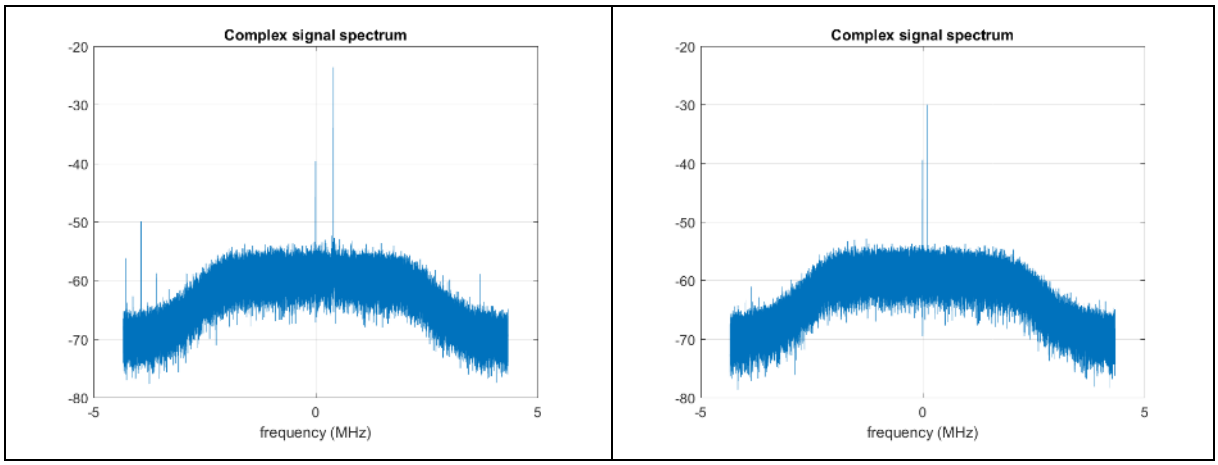

Figure 1.9 Evolution of PLL / OL settings for mitigation of spurious

In this figure several spurious frequencies are easily identified together with the single tone close to 0 Hz. These spurious are different mixes between the different frequencies included, i.e. the PLLs intermediate frequencies, RF input tone, board reference clock harmonics, microcontroller clock generator pulses ...

In the lower figure the selected configuration shows clearly the input single tone displaced 100KHz from DC, the baseband filter of ~4MHz bandwidth and no noticeable in-band spurious.

1.2.2.2 Adaptation of oscillator

The oscillator goes through a buffer and amplification circuit, before passing through a dedicated clock divider for their distribution to the different elements in the board.

The amplification circuit was adjusted in order to provide a signal with optimal amplitude avoiding too high levels, not only for causing saturation problems but for avoiding interference or coupling with the rest of the circuit; also trying to work in the middle of the voltage limits required by the downconverters.

1.2.2.3 Removing of unneeded circuitry

Any circuitry not used was removed from the board. Those sections intended for testing or as alternatives to certain modules in the board were finally unmounted after the adjustment done to the rest of the circuit.

1.2.3 RF measurements

1.2.3.1 S-parameters

S11 parameter was measured for the L2/L5 band of the front-end. Besides, the S22 parameter for the tri-band antenna was also measured.

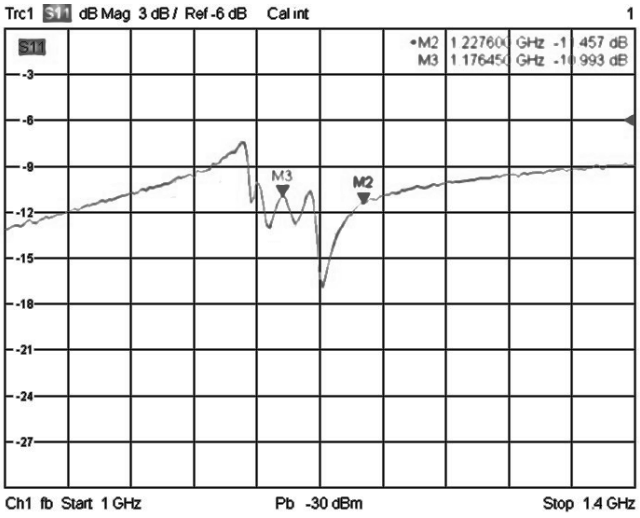

Figure 1.10 S11 parameter of L2/L5 branch of the front-end

As shown in Figure 1.10, the results for L2 and L5 frequency marker points in the FE measurement, although not excellent, are still acceptable in the order of the L1 downconverter shown in Figure 1.11.

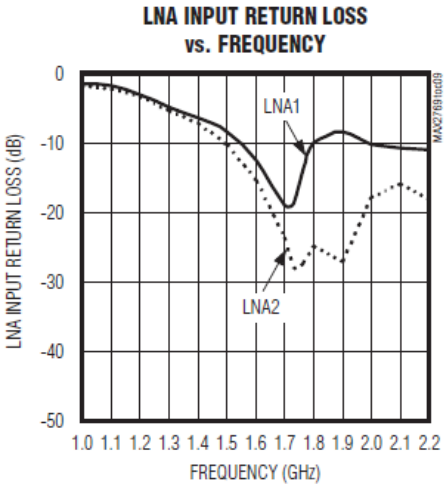

Figure 1.11 S11 parameter of final downconverter MAX2769 according to datasheet

On the other hand, the measurements of the L1 branch of the front-end are quite similar, and match the values provided by the manufacturer in the datasheet of the downconverter.

With respect to the tri-band antenna, the S22 parameter shows good values, as shown in Figure 1.12.

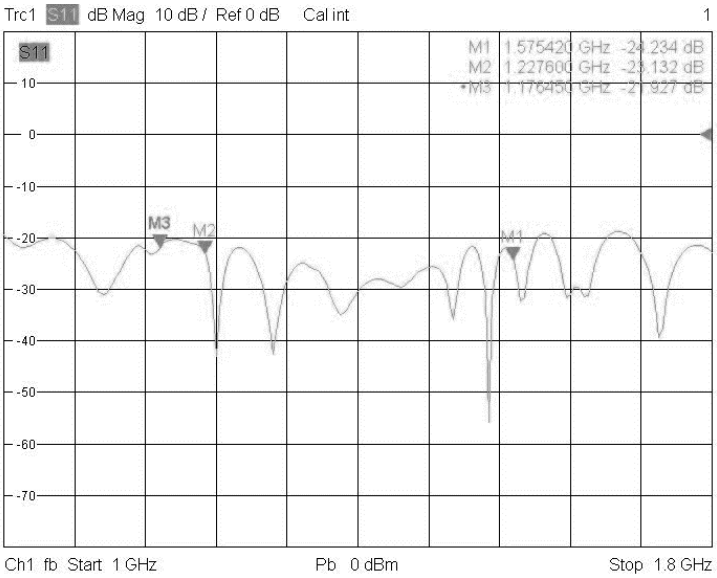

Figure 1.12 S11 parameter of tri-band antenna

1.2.3.2 LO phase noise

Several TCXO were mounted and measured in order to identify the optimal candidate. The L2/L5 OL phase noise obtained with each TCXO was measured. The following table shows the optimal values obtained for the primary LO generated when using the 26MHz TCXO selected for the 2nd front-end version with configured loop filter.

Table 1-1 LO phase noise

Frequency offset	dBc/Hz
100 Hz	-74
1 kHz	-85
10 kHz	-90
100 kHz	-107
1 MHz	-133

1.2.3.3 Power measurements in RF chain

The whole amplification chain of the front-end in L2/L5 band was analyzed. A signal generator was connected to the RF L2/L5 input of the front-end, the power level of this signal was set in the range -115dBm to -90 dBm during tests.

In both cases (L2 and L5), the steps followed consist of:

- Visualizing the signals with a standard spectrum analyzer using a laboratory probe to take measurements in every intermediate point of the amplification chain. The actual measurements can actually vary around 3 dB due to the effect of the probe in the circuit depending on the test point utilized in the PCB. The summary of one set of this measurement is shown in Table 1-2, matching the actual gain to the designed value.

Table 1-2 Summary of measurements in RF chain

After point	Design	Actual measurement
Input	-100 dBm (reference signal)	-124 dBm (reference signal)
1st LNA	-86 dBm	-110 dBm
2nd LNA	-72 dBm	-99 dBm
1st Mux	-73 dBm	-
1st filter	-76 dBm	-102 dBm
2nd Mux	-77 dBm	-103 dBm
First mix	-85 dBm	-110 dBm
2nd filter	-87 dBm	-112 dBm
Total gain	*+13 dB*	*+12 dB*

- Visualizing the baseband signal by configuring the final downconverter output in differential analog mode, and connecting it to a differential-to-single transceiver (MAX444) to measure the output spectrum, see Figure 1.13.

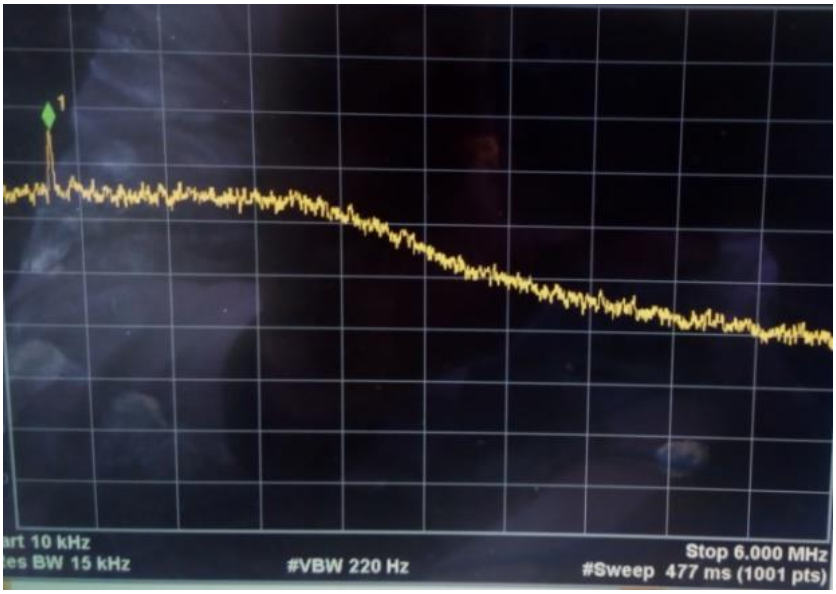

Figure 1.13 Baseband signal of a test carrier visualized in spectrum analizer

- Visualizing the spectrum after the final downconverter, by performing captures with the support tools mentioned in section 1.2.1 (ZedBoard, Logic Analyzers or custom USB adapter board), see Figure 1.14.

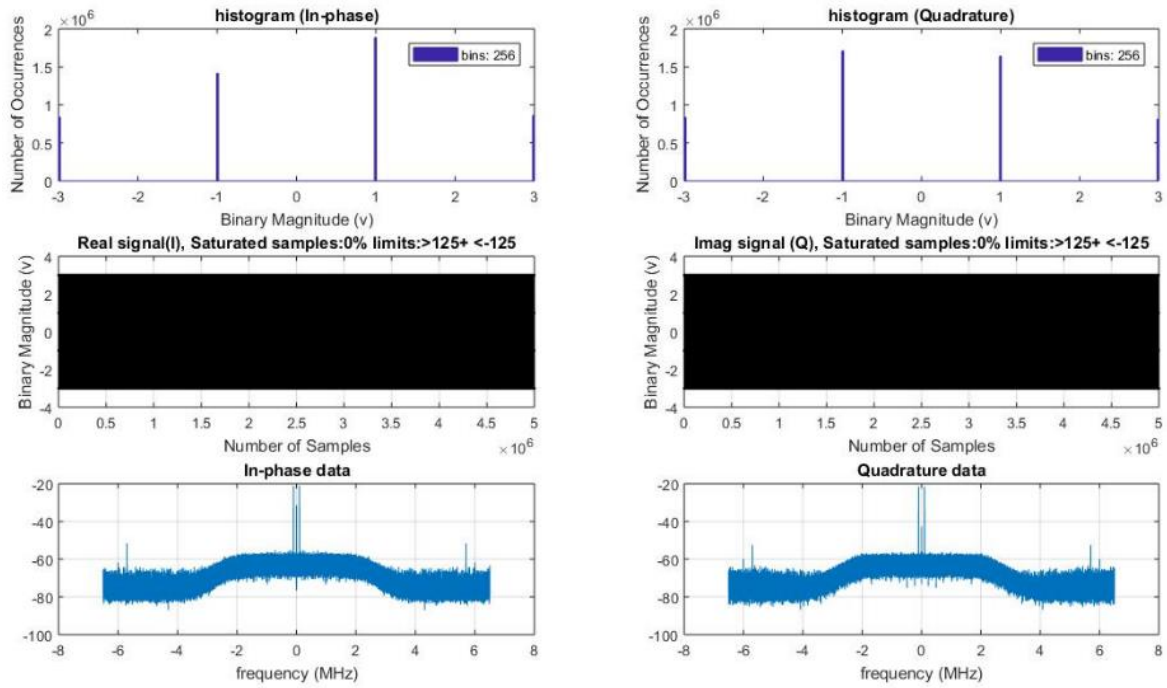

Figure 1.14 Processing of test carrier at L1

1.2.3.4 BPSK measurements

After the RF measurements and tests with single tone signals, a BPSK signal is utilized in order to better evaluate the effects of wide band signals similar to the real GNSS scenario.

A vector signal generator is used to generate and inject a 1Msps BPSK to the front-end. The signal is monitored after the first down-conversion stage and connected to a vector signal generator to decode the BPSK. This test evaluates if there are problems with the phase of the signal after the first part of the RF chain.

It must be noticed that the power level of the input signal required to make the BPSK visible with the laboratory equipment in this case is much higher (around -50 dBm) than in a real GNSS scenario, in order to be able to demodulate the symbols clearly with the laboratory equipment without de-spreading the signal.

Figure 1.15 shows the results of the reception of the BPSK in a vector signal analyzer. The constellation diagram shows two clean symbols and no problems with the phase stability seems to exist.

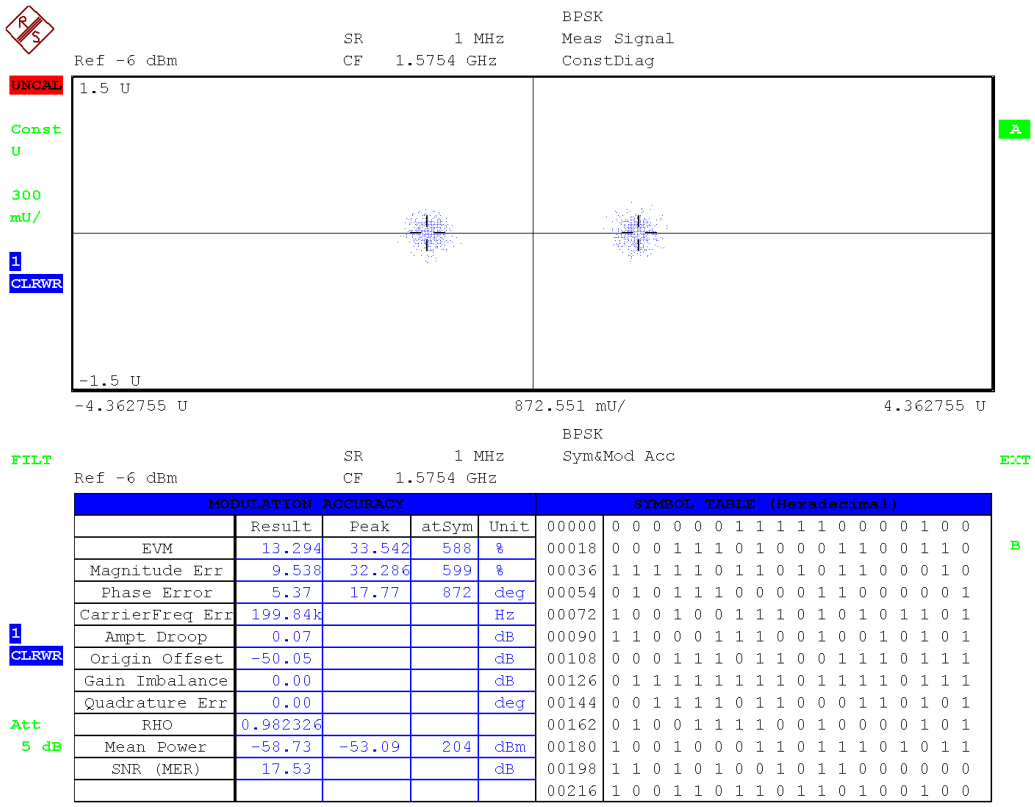

MODULATION ACCURACY

	Result	Peak	atSym	Unit
EVM	13.294	33.542	588	%
Magnitude Err	9.538	32.286	599	%
Phase Error	5.37	17.77	872	deg
CarrierFreq Err	199.84k			Hz
Ampt Droop	0.07			dB
Origin Offset	-50.05			dB
Gain Imbalance	0.00			dB
Quadrature Err	0.00			deg
RHO	0.982326			
Mean Power	-58.73	-53.09	204	dBm
SNR (MER)	17.53			dB

SYMBOL TABLE (Hexadecimal)

00000	0	0	0	0	0	0	1	1	1	1	1	0	0	0	0	1	0	0
00018	0	0	0	1	1	1	0	1	0	0	0	1	1	0	0	1	1	0
00036	1	1	1	1	1	0	1	1	0	1	0	1	1	0	0	0	1	0
00054	0	1	0	1	1	1	0	0	0	0	1	1	0	0	0	0	0	1
00072	1	0	0	1	0	0	1	1	1	0	1	0	1	0	1	1	0	1
00090	1	1	0	0	0	1	1	1	0	0	1	0	0	1	0	1	0	1
00108	0	0	0	1	1	1	0	1	1	0	0	1	1	1	0	1	1	1
00126	0	1	1	1	1	1	1	1	1	0	1	1	1	1	0	1	1	1
00144	0	0	1	1	1	1	0	1	1	0	0	0	0	1	1	0	1	0	1
00162	0	1	0	0	1	1	1	1	0	0	1	0	0	0	0	1	0	1
00180	1	0	0	1	0	0	0	1	1	0	1	1	1	1	0	1	0	1	1
00198	1	1	0	1	0	1	0	0	1	0	1	1	0	0	0	0	0	0
00216	1	0	0	1	1	0	1	1	0	1	1	0	1	0	0	1	0	0

Figure 1.15 BPSK decoded affter the first downconversion stage for L2

The BPSK spectrum of an input signal with much less power (around -115 dBm) can be made visible when performing a USB capture, that is sampled after the last down-conversion which includes an additional amplification and filter stage. Figure 1.16 shows the I/Q BPSK spectrum barely noticeable in the ±2MHz bandwidth.

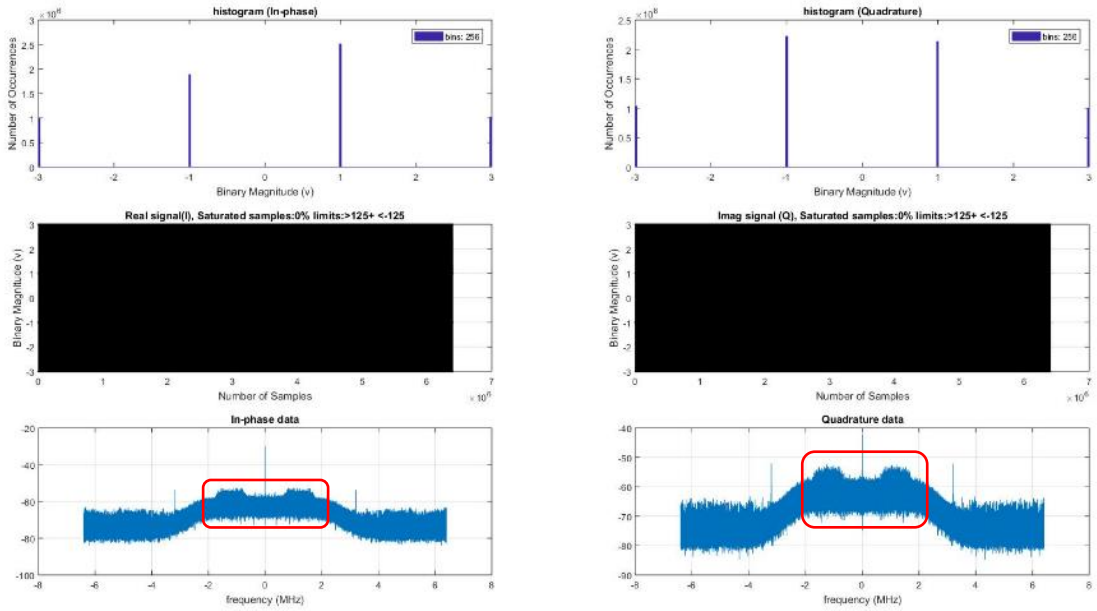

Figure 1.16 BPSK in baseband (IF=1MHz) after digitalization at the output of the front-end

1.2.3.5 Noise figure

Finally, the Noise figure of the front-end for both L2 and L5/E5a bands is measured. NF of L1 is not measured as this branch consist in a direct down-conversion using the MAX2769 reference design.

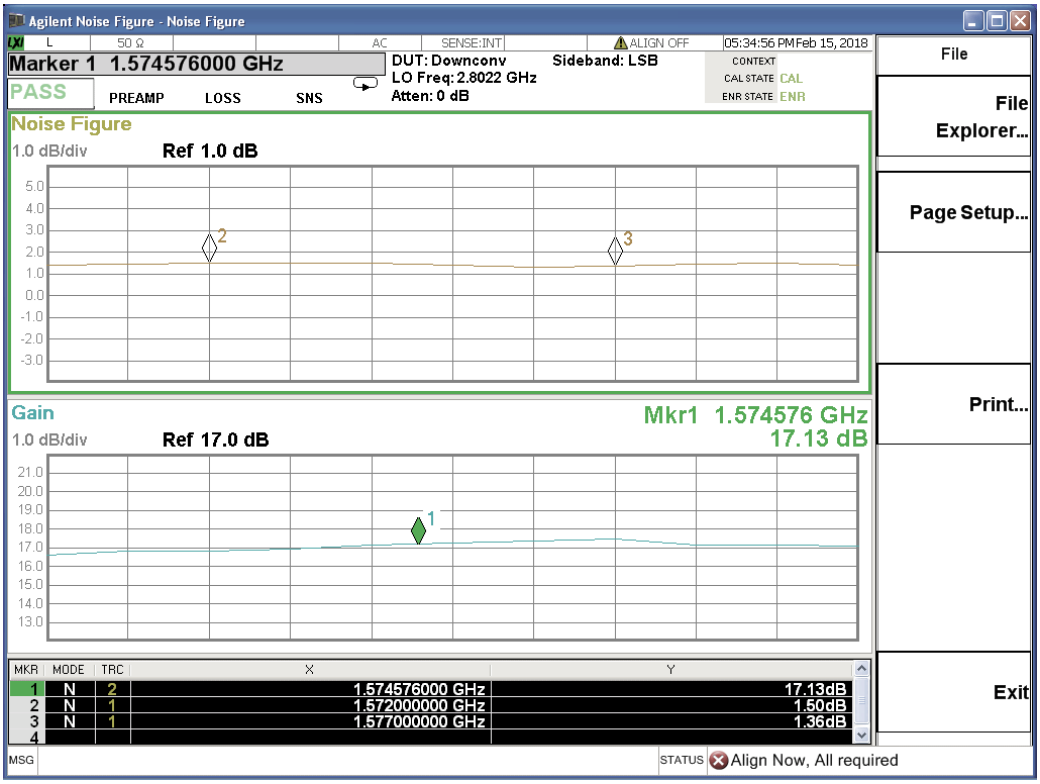

Figure 1.17 Noise figure and gain of L2 band

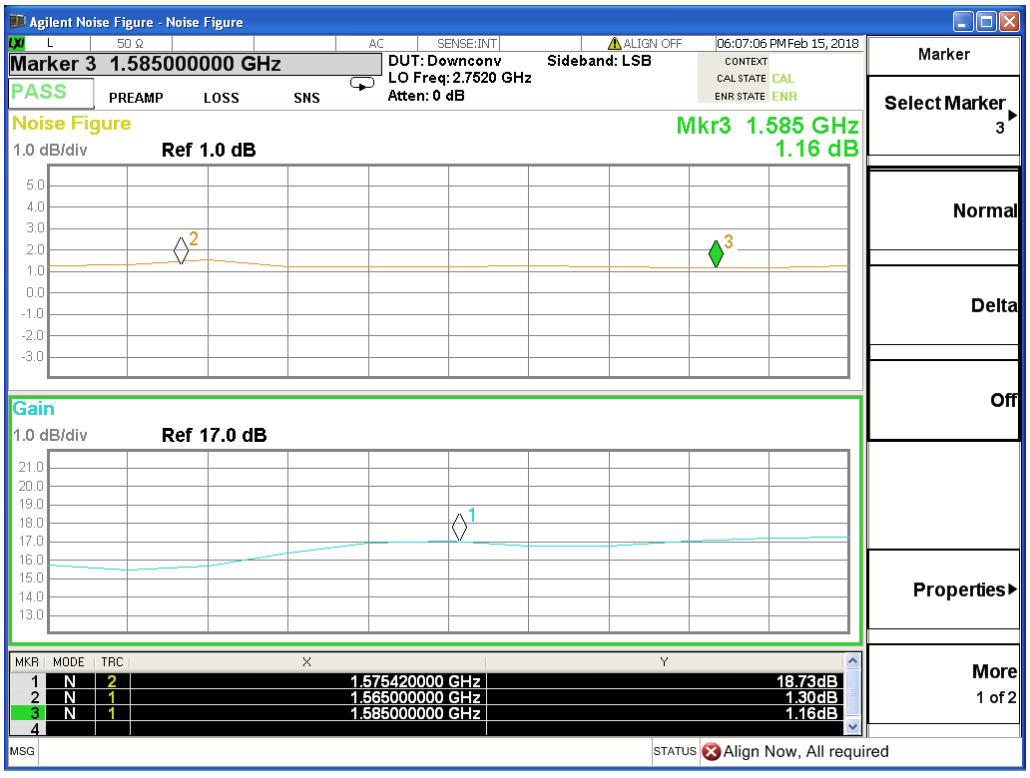

Figure 1.18 Noise figure and gain of L5 band

Figure 1.17 shows the measurements obtained for L2 band, after the first down-conversion stage. In addition, the gain of the RF chain until that point is also estimated.

Marker 1 depicts the gain at the center frequency and markers 2 and 3 show the noise figure at the preconfigured band limits. Due to the measurement method, the gain obtained can slightly vary with respect to the actual gain.

The same measurements are done for L5 band, with the results presented in Figure 1.18.

1.3 Front-end and Software-receiver integration results (confidential)

In the FE GNSS-SDR validation several setups were tested. These setups were evolutions from the original FE architecture to overcome issues detected after applying the GNSS-SDR post-processing of the captured baseband signal:

- Setup #1: original FE architecture already presented in D3.1/D6.1 ([2]/[1]) and in section 1.1.
- Setup #2: setup #1 downgraded from 8-bit to 2-bit per I/Q signal and with internal AGC.
- Setup #3: setup #2 with external clock reference.
- Setup #4: setup based on new transceiver.

In the following sections one set of representative measurements for each setup are presented and the rationale behind this evolution of the design is described.

In all cases the captures are analyzed with custom scripts (spectrum and histogram) and GNSS-SDR (acquisition and tracking).

1.3.1 Setup #1

Setup #1 corresponds to the original design of the FE v2.0. It provides 8-bits samples per I/Q channel and utilizes a custom external AGC managed by the onboard microcontroller through dedicated circuitry.

1.3.1.1 Noise generated by the microcontroller

In this setup the noise generated by the microcontroller was heavily reduced from FE v1.0. However its interference with the capture of the base band signal still was very noticeable.

Figure 1.19 shows the effect of the microcontroller noise in the spectrum of the input signal, a single tone at L1, visible at IF=420 kHz. This noise can actually vary in time as its related to the microcontroller execution tasks related to the AGC implementation, which are asynchronous to the data capture and GNSS signals.

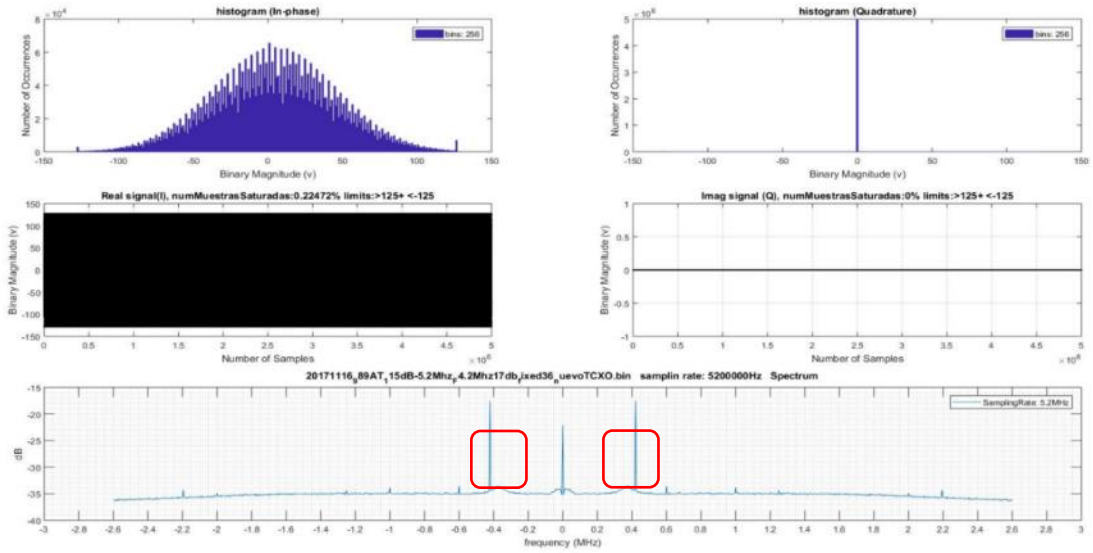

Figure 1.19 Noise generated by the microcontroller

Different combinations of the internal reference clock generated by the microcontroller were tested in order to minimize the noise generated.

The analysis performed indicate that the noise cannot be entirely removed unless the microcontroller is powered off or is suspended state. As the AGC can only work if the microcontroller is running, the following procedure is required when performing a capture:

1. An initial running state for some seconds were the microcontroller is active, so that the AGC sets an appropriate gain.
2. Suspending the microcontroller
3. Performing the actual capture

This approach is useful for short or medium-term captures in open sky scenarios, in which no large variations in the signal level are expected, but it is likely to be a problem for long term captures.

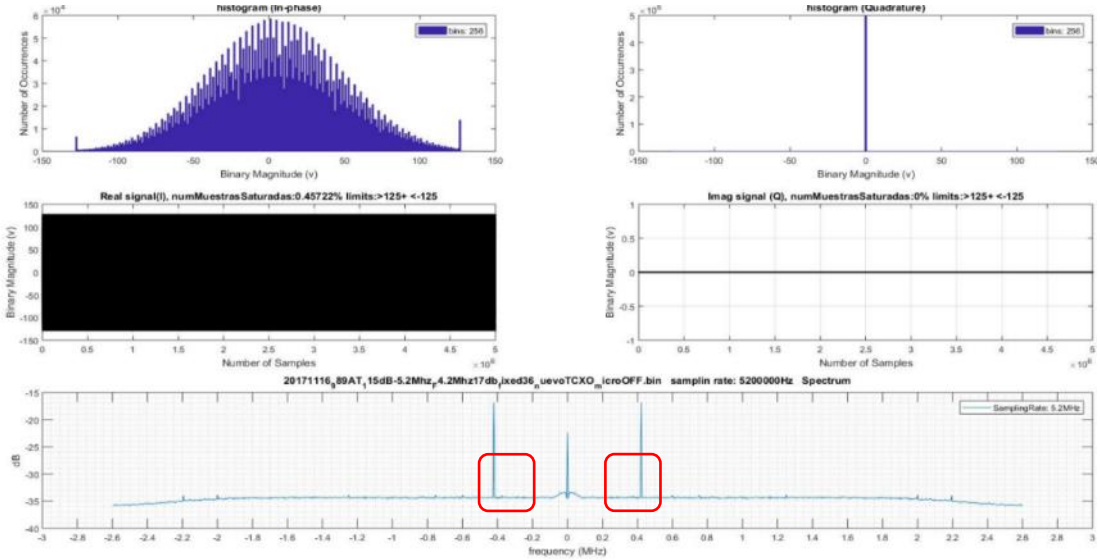

Figure 1.20 Noise generated by the microcontroller

1.3.1.2 Outdoor captures

The data collected during the open sky tests can be, after a conversion to interleaved I/Q format, directly processed by GNSS-SDR.

The outdoor captures, as shown in Figure 1.21, are performed in open and clean sky, far away from buildings. The ground plane provided by the manufacturer of the antenna (with optimal geometry and size) was utilized. The FE was powered by batteries.

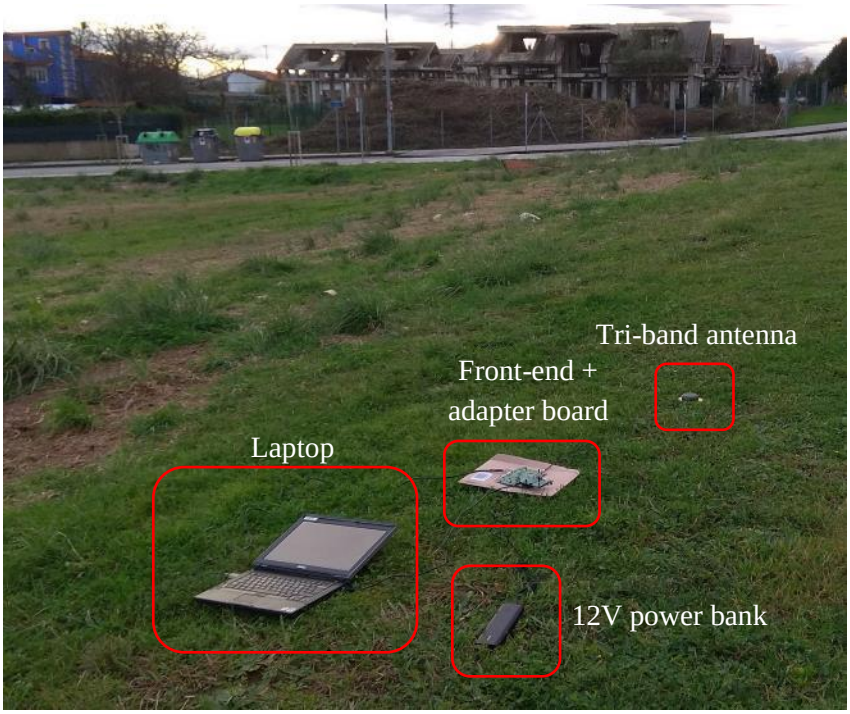

Figure 1.21 Setup for outdoor tests

The analysis of several outdoor captures provided the following conclusions:

- L1/E1 band:
  - Acquisition and tracking of satellite work.
  - PVT can be obtained.
  - Spectrum is not entirely clean.
- L2 band:
  - Acquisition of satellites is not stable (lock is easily lost)

1.3.2 Setup #2

This setup, depicted in Figure 1.22, consists in a modification to the setup #1 by removing the external AGC and associated microcontroller.

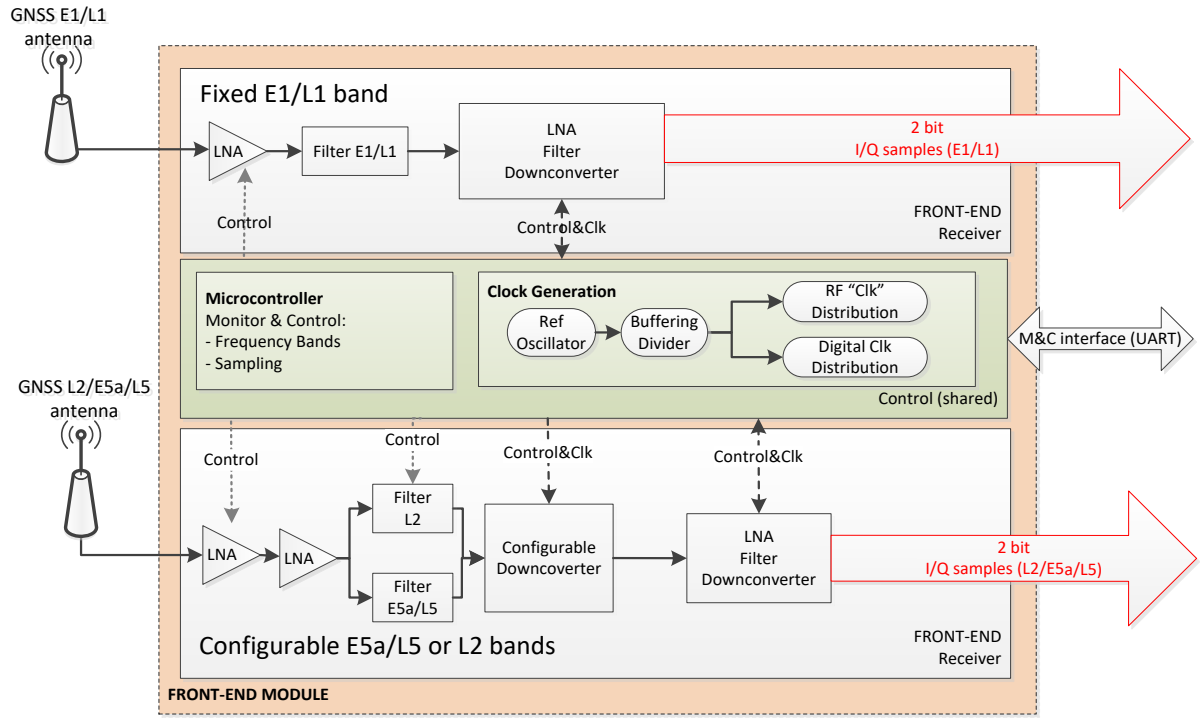

Figure 1.22 Architecture of 2nd version of the front-end (setup #2)

The outputs resolution changes from the original 8-bit to 2-bit (the default ADC integrated into the downconverter in used instead of the external 8-bit ADC), which allows to reduce the noise and interferences caused by the external AGC circuitry that can now be removed from the board.

The utilization of the internal AGC of the downconverter solves the problem caused by the suspension of the microcontroller required to remove its noise. The microcontroller can be utilized to configure the different elements in the front-end (synthesizer, downconverters, multiplexers and clock distribution chips), and afterwards it can be suspended, but in this case with the internal AGC active.

The main drawback of this modification, apart for the decreasing of the number of bits in the output, whose impact in the solution should be small, is that the value of the gain currently applied to the AGC is not externally available. Despite this, the impact is negligible as gain value is currently not heavily utilized by the baseband processing.

1.3.2.1 Outdoor captures

The outdoor captures are performed with open and clean sky, far away from buildings. A ground plane provided by the manufacturer of the antenna was utilized. The front-end was powered by batteries.

Several outdoor captures analysis provided the following conclusions:

- L1/E1 band:
  - Acquisition and tracking of satellite work.
  - PVT can be obtained.
- L2 band:
  - Acquisition of satellites works but tracking not.

- Some punctual messages (UTC correction and IONO parameters) are decoded in some captures.

- L5 band:
  - Acquisition of satellites does not work.

A cleaner spectrum than the previous 8-bit version is obtained in all cases.

The results of an outdoor L1 band capture processed with GNSS-SDR are shown in Figure 1.14, where some excerpts of the application output of GNSS-SDR application have been removed for clearness.

```
linux; GNU C++ version 5.3.1 20151219; Boost_105800; UHD_003.009.002-0-unknown
Initializing GNSS-SDR v0.0.9.git-next-bb098ef ... Please wait.
Processing file ./20171205_1240_790AT_L1_6.5Mhz_F4.2_antenaexterior2bitsmicrooff_toma2.L1.ibyter,
which contains 737280000 [bytes]
GNSS signal recorded time to be processed: 56.7128 [s]
Tracking of GPS L1 C/A signal started on channel 0 for satellite GPS PRN 06 (Block IIF)
Tracking of GPS L1 C/A signal started on channel 1 for satellite GPS PRN 09 (Block IIF)
Tracking of GPS L1 C/A signal started on channel 2 for satellite GPS PRN 17 (Block IIR-M)
Tracking of GPS L1 C/A signal started on channel 3 for satellite GPS PRN 19 (Block IIR)
Tracking of GPS L1 C/A signal started on channel 4 for satellite GPS PRN 23 (Block IIR)
Current receiver time: 4 [s]
Tracking of GPS L1 C/A signal started on channel 5 for satellite GPS PRN 13 (Block IIR)
Tracking of GPS L1 C/A signal started on channel 6 for satellite GPS PRN 01 (Block IIF)
Current receiver time: 6 [s]
Loss of lock in channel 6!
Loss of lock in channel 5!
Current receiver time: 10 [s]
Tracking of GPS L1 C/A signal started on channel 7 for satellite GPS PRN 15 (Block IIR-M)
Current receiver time: 12 [s]
Loss of lock in channel 7!
Tracking of GPS L1 C/A signal started on channel 5 for satellite GPS PRN 10 (Block IIF)
Current receiver time: 14 [s]
Loss of lock in channel 5!
Current receiver time: 15 [s]
New GPS NAV message received: subframe 4 from satellite GPS PRN 09 (Block IIF)
New GPS NAV message received: subframe 4 from satellite GPS PRN 06 (Block IIF)
Current receiver time: 21 [s]
New GPS NAV message received: subframe 5 from satellite GPS PRN 09 (Block IIF)
New GPS NAV message received: subframe 5 from satellite GPS PRN 06 (Block IIF)
Current receiver time: 26 [s]
Tracking of GPS L1 C/A signal started on channel 6 for satellite GPS PRN 03 (Block IIF)
Current receiver time: 27 [s]
New GPS NAV message received: subframe 1 from satellite GPS PRN 09 (Block IIF)
New GPS NAV message received: subframe 1 from satellite GPS PRN 23 (Block IIR)
New GPS NAV message received: subframe 1 from satellite GPS PRN 06 (Block IIF)
New GPS NAV message received: subframe 1 from satellite GPS PRN 17 (Block IIR-M)
Current receiver time: 33 [s]
New GPS NAV message received: subframe 2 from satellite GPS PRN 09 (Block IIF)
New GPS NAV message received: subframe 2 from satellite GPS PRN 23 (Block IIR)
New GPS NAV message received: subframe 2 from satellite GPS PRN 06 (Block IIF)
New GPS NAV message received: subframe 2 from satellite GPS PRN 03 (Block IIF)
New GPS NAV message received: subframe 2 from satellite GPS PRN 19 (Block IIR)
New GPS NAV message received: subframe 2 from satellite GPS PRN 17 (Block IIR-M)
Current receiver time: 34 [s]
Tracking of GPS L1 C/A signal started on channel 5 for satellite GPS PRN 11 (Block IIR)
Current receiver time: 36 [s]
Loss of lock in channel 5!
Current receiver time: 39 [s]
New GPS NAV message received: subframe 3 from satellite GPS PRN 09 (Block IIF)
New GPS NAV message received: subframe 3 from satellite GPS PRN 23 (Block IIR)
New GPS NAV message received: subframe 3 from satellite GPS PRN 06 (Block IIF)
New GPS NAV message received: subframe 3 from satellite GPS PRN 03 (Block IIF)
New GPS NAV message received: subframe 3 from satellite GPS PRN 19 (Block IIR)
New GPS NAV message received: subframe 3 from satellite GPS PRN 17 (Block IIR-M)
First position fix at 2017-Dec-05 11:45:59.839103 UTC is Lat = 43.4514 [deg], Long = -3.86046 [deg],
Height= 73.7901 [m]
Position at 2017-Dec-05 11:45:59.839103 UTC using 4 observations is Lat = 43.4514 [deg], Long = -
3.86046 [deg], Height= 73.7901 [m]
Position at 2017-Dec-05 11:45:59.939103 UTC using 4 observations is Lat = 43.4514 [deg], Long = -
3.86046 [deg], Height= 71.7619 [m]
Position at 2017-Dec-05 11:46:00.039103 UTC using 4 observations is Lat = 43.4514 [deg], Long = -
3.86045 [deg], Height= 70.362 [m]
```

```
Position at 2017-Dec-05 11:46:00.139103 UTC using 4 observations is Lat = 43.4514 [deg], Long = -
3.86045 [deg], Height= 68.8593 [m]
Current receiver time: 40 [s]
Position at 2017-Dec-05 11:46:00.239103 UTC using 4 observations is Lat = 43.4514 [deg], Long = -
3.86046 [deg], Height= 68.5908 [m]
Position at 2017-Dec-05 11:46:00.339103 UTC using 4 observations is Lat = 43.4514 [deg], Long = -
3.86046 [deg], Height= 67.6988 [m]
Position at 2017-Dec-05 11:46:00.439103 UTC using 4 observations is Lat = 43.4514 [deg], Long = -
3.86045 [deg], Height= 66.4026 [m]
Position at 2017-Dec-05 11:46:00.539103 UTC using 4 observations is Lat = 43.4514 [deg], Long = -
3.86045 [deg], Height= 65.3207 [m]
Position at 2017-Dec-05 11:46:00.639103 UTC using 0 observations is Lat = 43.4514 [deg], Long = -
3.86045 [deg], Height= 64.8344 [m]
Position at 2017-Dec-05 11:46:00.739103 UTC using 4 observations is Lat = 43.4514 [deg], Long = -
3.86045 [deg], Height= 64.9972 [m]
Position at 2017-Dec-05 11:46:00.839104 UTC using 4 observations is Lat = 43.4514 [deg], Long = -
3.86046 [deg], Height= 65.3242 [m]
Position at 2017-Dec-05 11:46:00.939104 UTC using 4 observations is Lat = 43.4514 [deg], Long = -
3.86046 [deg], Height= 65.7532 [m]
Position at 2017-Dec-05 11:46:01.039104 UTC using 4 observations is Lat = 43.4514 [deg], Long = -
3.86046 [deg], Height= 66.5013 [m]
Position at 2017-Dec-05 11:46:01.139104 UTC using 4 observations is Lat = 43.4514 [deg], Long = -
3.86047 [deg], Height= 67.3374 [m]
Current receiver time: 41 [s]
Position at 2017-Dec-05 11:46:01.239104 UTC using 4 observations is Lat = 43.4514 [deg], Long = -
3.86047 [deg], Height= 68.2483 [m]
Position at 2017-Dec-05 11:46:01.339104 UTC using 0 observations is Lat = 43.4514 [deg], Long = -
3.86047 [deg], Height= 68.9373 [m]
Position at 2017-Dec-05 11:46:01.439104 UTC using 4 observations is Lat = 43.4514 [deg], Long = -
3.86047 [deg], Height= 69.1711 [m]
Position at 2017-Dec-05 11:46:01.539104 UTC using 4 observations is Lat = 43.4514 [deg], Long = -
3.86048 [deg], Height= 69.3894 [m]
Position at 2017-Dec-05 11:46:01.639104 UTC using 4 observations is Lat = 43.4514 [deg], Long = -
3.86048 [deg], Height= 69.6711 [m]
Position at 2017-Dec-05 11:46:01.739104 UTC using 4 observations is Lat = 43.4514 [deg], Long = -
3.86048 [deg], Height= 70.0333 [m]
Position at 2017-Dec-05 11:46:01.839104 UTC using 4 observations is Lat = 43.4514 [deg], Long = -
3.86048 [deg], Height= 70.4265 [m]
Position at 2017-Dec-05 11:46:01.939104 UTC using 4 observations is Lat = 43.4514 [deg], Long = -
3.86048 [deg], Height= 70.594 [m]
```

Figure 1.23 PVT results obtained with GNSS-SDR after processing a L1 band capture

1.3.3 Setup #3

Setup #3 is similar to setup #2 but includes an external TCXO, see Figure 1.24, with better frequency stability. Several external TCXOs were evaluated with the same clock frequency (26MHz) or lower (12.8MHz):

- TSEAMCSANF-26.000000 (26MHz 0.1ppm)
- LFTCXO075793Cutt (12.800MHz 0.28ppm)
- LFMCXO064082 (12.8 MHz 0.05ppm)

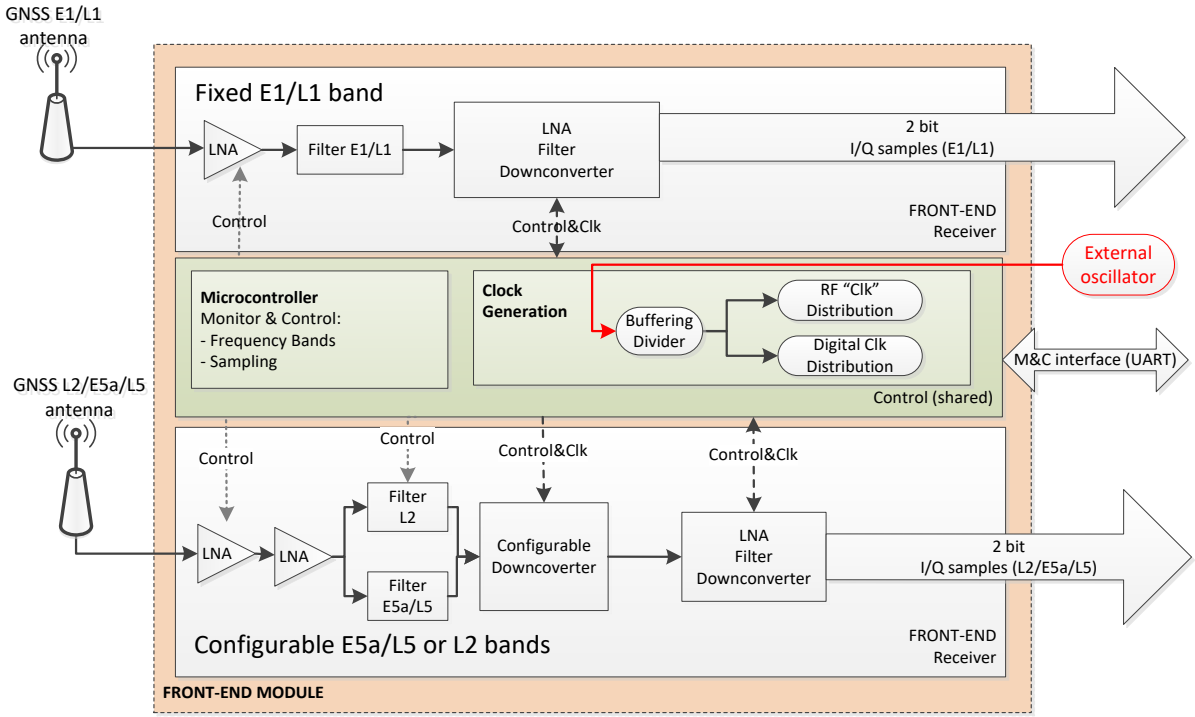

Figure 1.24 Architecture of 2nd version of the front-end (setup #3)

Some of the TCXO were mounted into a commercial evaluation board specially designed for testing TCXOs, see Figure 1.25. This board is required to integrate the new TCXO with the front-end as its footprint is not suitable for the PCB. The old TCXO integrated into the FE PCB was disconnected to avoid further interference with the new TCXO of the TCXO evaluation board.

Figure 1.25 Additional board utilized for external TCXO

Table 1-3 shows a comparison between the original TCXO and one of the 26MHz replacement. It must be noticed that in case of the replacement, the phase noise in the datasheet is measured for a TCXO of the same series with different nominal frequency.

Table 1-3 Comparison between original TCXO and replacement

	Original TCXO	Replacement
Frequency stability	0.5 ppm	0.1 ppm
Phase noise (manufacturer info)	-130 dBc/Hz @ 1kHz *@ frequency=**26MHz***	-120 dBc/Hz @ 100Hz -140 dBc/Hz @ 1kHz -148 dBc/Hz @ 10kHz *@ frequency=**19.2MHz***

1.3.3.1 Outdoor captures

As in the previous setups, the outdoor captures are performed with open and clean sky, far away from buildings (in the same position than in the previous tests) and using the same ground plane for the antenna and batteries for powering the devices.

The analysis of several outdoor captures provides the following conclusions for L2:

- L2 band:
  - Acquisition and tracking of satellites work fine for one of the tested configurations (configuration #05).
  - This configuration works when working with one of the 26MHz replacement both 6.5MHz and 13MHz sampling frequencies.

Figure 1.26 shows the tracking results of an L2 band capture processed with GNSS-SDR. In addition, Figure 1.28 shows the detailed results for the tracking of a satellite in an outdoor L2 capture done with "configuration #05" after an offline low-level processing performed by CTTC.

The receiver configuration used in Figure 1.26 was setting a very low acquisition threshold, which causes frequent false detections (as it was the case for satellite PRN 22), plus very relaxed lock detection thresholds, so the receiver keeps the tracking loop locked to the non-existing signal during a few seconds before declaring the signal lost. This configuration is not practical for a real deployment, and it was corrected in following trials. A more strict configuration was tested that reduced the false positives, as shown in Figure 1.27. The receiver is now validated with live L2C(M) signals and, as expected, only satellites belonging to Block IIR-M and IIF are detected, tracked and used for the PVT solution, both as a standalone signal and using dual-band combinations with L1. The details about this validation will be included in D3.2 [3].

```
linux; GNU C++ version 5.3.1 20151219; Boost_105800; UHD_003.009.002-0-unknown
Initializing GNSS-SDR v0.0.9.git-next-bb098ef ... Please wait.
Processing file data_20180206_165723_790AT_05_L2_IF100kHz_Fs6.5MHz_FBW4.2MHz_OSCext26MHz-
10dB.L25.ibyte, which contains 1429995520 [bytes]
GNSS signal recorded time to be processed: 109.999 [s]
Current receiver time: 2 [s]
Tracking of GPS L2CM signal started on channel 0 for satellite GPS PRN 06 (Block IIF)
Current receiver time: 4 [s]
Tracking of GPS L2CM signal started on channel 1 for satellite GPS PRN 12 (Block IIR-M)
Current receiver time: 6 [s]
Tracking of GPS L2CM signal started on channel 2 for satellite GPS PRN 15 (Block IIR-M)
Current receiver time: 9 [s]
Tracking of GPS L2CM signal started on channel 3 for satellite GPS PRN 22 (Block IIR)
Current receiver time: 13 [s]
Loss of lock in channel 0!
Current receiver time: 14 [s]
Tracking of GPS L2CM signal started on channel 0 for satellite GPS PRN 06 (Block IIF)
Current receiver time: 21 [s]
Loss of lock in channel 3!
Current receiver time: 22 [s]
Tracking of GPS L2CM signal started on channel 3 for satellite GPS PRN 24 (Block IIF)
Current receiver time: 25 [s]
Loss of lock in channel 0!
Current receiver time: 26 [s]
Tracking of GPS L2CM signal started on channel 0 for satellite GPS PRN 25 (Block IIF)
Current receiver time: 33 [s]
New GPS CNAV message received: iono model parameters from satellite GPS PRN 15 (Block IIR-M)
Current receiver time: 38 [s]
Loss of lock in channel 0!
Current receiver time: 39 [s]
Tracking of GPS L2CM signal started on channel 0 for satellite GPS PRN 25 (Block IIF)
Current receiver time: 51 [s]
Loss of lock in channel 0!
Current receiver time: 52 [s]
Tracking of GPS L2CM signal started on channel 0 for satellite GPS PRN 25 (Block IIF)
Current receiver time: 56 [s]
New GPS CNAV message received: ephemeris from satellite GPS PRN 15 (Block IIR-M)
Current receiver time: 65 [s]
Loss of lock in channel 0!
Current receiver time: 66 [s]
Tracking of GPS L2CM signal started on channel 0 for satellite GPS PRN 25 (Block IIF)
Current receiver time: 78 [s]
Loss of lock in channel 0!
Current receiver time: 79 [s]
Tracking of GPS L2CM signal started on channel 0 for satellite GPS PRN 25 (Block IIF)
Current receiver time: 80 [s]
New GPS CNAV message received: iono model parameters from satellite GPS PRN 15 (Block IIR-M)
Current receiver time: 91 [s]
Loss of lock in channel 0!
Tracking of GPS L2CM signal started on channel 0 for satellite GPS PRN 25 (Block IIF)
New GPS CNAV message received: UTC model parameters from satellite GPS PRN 15 (Block IIR-M)
Current receiver time: 98 [s]
Loss of lock in channel 1!
Tracking of GPS L2CM signal started on channel 1 for satellite GPS PRN 12 (Block IIR-M)
Current receiver time: 102 [s]
Loss of lock in channel 0!
Current receiver time: 103 [s]
Current receiver time: 104 [s]
New GPS CNAV message received: ephemeris from satellite GPS PRN 15 (Block IIR-M)
```

Figure 1.26 Tracking example in L2 band with GNSS-SDR processing showing false IIR positives

```
linux; GNU C++ version 5.3.1 20151219; Boost_105800; UHD_003.009.002-0-unknown

Initializing GNSS-SDR v0.0.9.git-next-36ac696 ... Please wait.
Logging will be written at "/tmp"
Use gnss-sdr --log_dir=/path/to/log to change that.
Processing file data_20180206_165153_790AT_05_L2_IF100kHz_Fs13MHz_FBW4.2MHz_OSCext26MHz-
10dB.L25.ibyte, which contains 1429995520 [bytes]
GNSS signal recorded time to be processed: 54.9988 [s]
Using Volk machine: avx2_64_mmx_orc
Current receiver time: 1 s
Current receiver time: 2 s
Current receiver time: 3 s
Tracking of GPS L2C signal started on channel 0 for satellite GPS PRN 10 (Block IIF)
Tracking of GPS L2C signal started on channel 1 for satellite GPS PRN 12 (Block IIR-M)
Current receiver time: 4 s
Tracking of GPS L2C signal started on channel 2 for satellite GPS PRN 15 (Block IIR-M)
Current receiver time: 5 s
Current receiver time: 6 s
Current receiver time: 7 s
Tracking of GPS L2C signal started on channel 3 for satellite GPS PRN 24 (Block IIF)
Current receiver time: 8 s
Current receiver time: 9 s
Current receiver time: 10 s
Current receiver time: 11 s
Current receiver time: 12 s
Current receiver time: 13 s
Current receiver time: 14 s
Current receiver time: 15 s
Current receiver time: 16 s
Current receiver time: 17 s
Current receiver time: 18 s
Current receiver time: 19 s
Current receiver time: 20 s
Current receiver time: 21 s
Current receiver time: 22 s
Current receiver time: 23 s
Current receiver time: 24 s
Current receiver time: 25 s
Loss of lock in channel 1!
Tracking of GPS L2C signal started on channel 1 for satellite GPS PRN 12 (Block IIR-M)
Current receiver time: 26 s
Current receiver time: 27 s
New GPS CNAV message received in channel 2: iono model parameters from satellite GPS PRN 15 (Block
IIR-M)
Current receiver time: 28 s
Current receiver time: 29 s
Current receiver time: 30 s
Current receiver time: 31 s
Current receiver time: 32 s
Current receiver time: 33 s
Current receiver time: 34 s
Current receiver time: 35 s
Current receiver time: 36 s
Current receiver time: 37 s
Current receiver time: 38 s
Current receiver time: 39 s
New GPS CNAV message received in channel 2: UTC model parameters from satellite GPS PRN 15 (Block
IIR-M)
Current receiver time: 40 s
Current receiver time: 41 s
Current receiver time: 42 s
Current receiver time: 43 s
Current receiver time: 44 s
Current receiver time: 45 s
Current receiver time: 46 s
Current receiver time: 47 s
Current receiver time: 48 s
Current receiver time: 49 s
Current receiver time: 50 s
Current receiver time: 51 s
Current receiver time: 52 s
Current receiver time: 53 s
Current receiver time: 54 s
Current receiver time: 55 s
Stopping GNSS-SDR, please wait!
Total GNSS-SDR run time: 103.788 [seconds]
```

```
GNSS-SDR program ended.
```

Figure 1.27 Tracking example in L2 band with GNSS-SDR processing

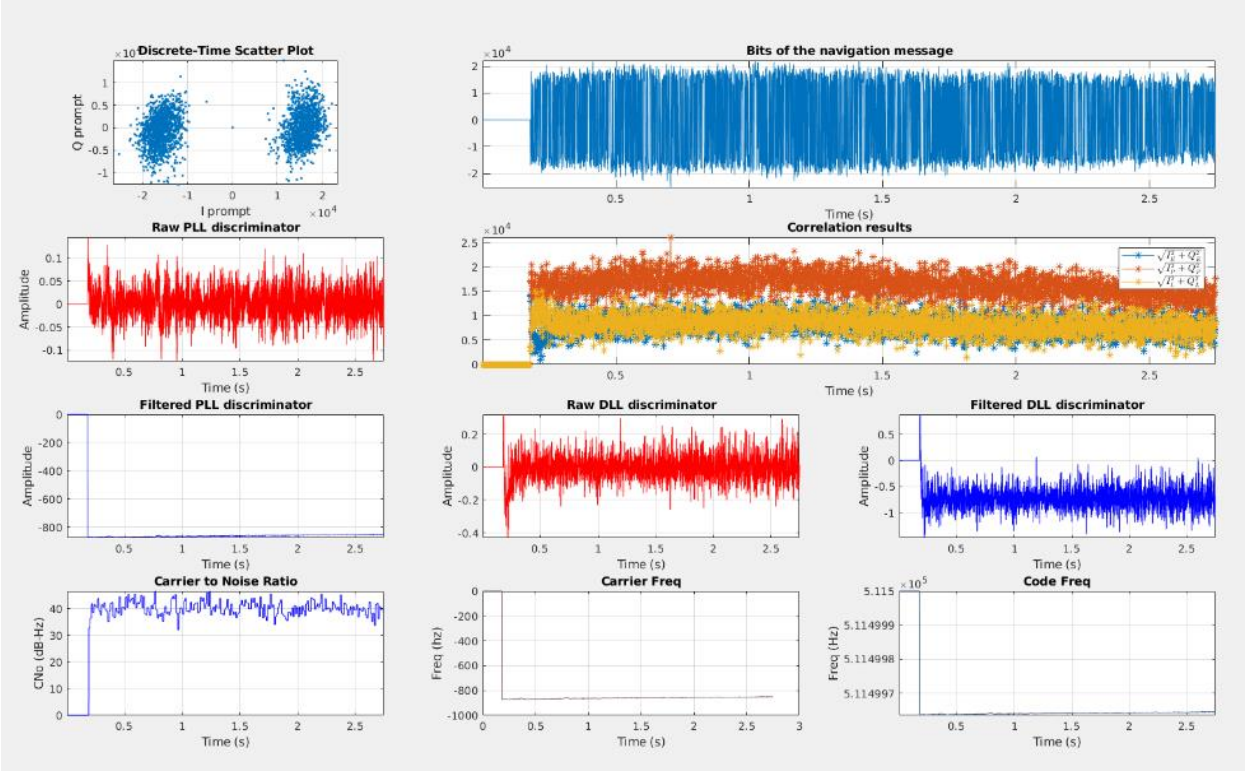

Figure 1.28 Tracking of L2 satellite with configuration #05

1.3.4 Setup 4#: NTLAB Front-end

Due to the limitations of transceiver used in previous setups (in-band spurious, digital and clock related noises, limited NF control, BW configuration limitations for L2&L5) an alternative architecture for the FE was proposed that was not based on the MAX2769 by Maxim. This architecture is based on the integrated GNSS transceiver NT1065 "Nomada" by NTLAB[1], see Figure 1.29, which has the following key features for AUDITOR:

- Single conversion superheterodyne receiver
- 4 independent configurable channels
- Signal output options: 2-bit ADC
- Signal bandwidth up to 31MHz
- FMC interface kit available

[1] http://ntlab.com

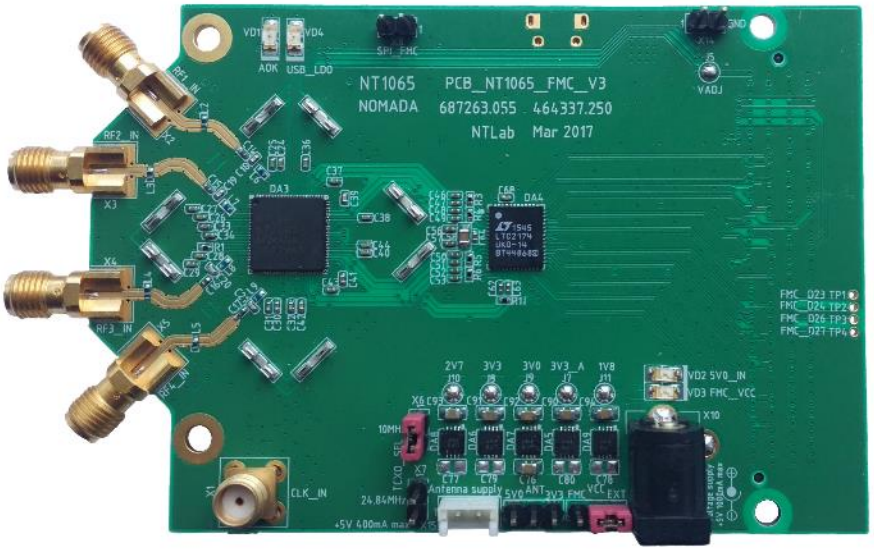

Figure 1.29 NT1065_FMC2

This setup was preliminary tested standalone in the laboratory (offline acquisitions) before the DDM milestone where it was introduced. Outdoor tests were performed with this FE integrated into the final GNSS-receiver (FE + digital platform + GNSS-SDR) which hardware also was upgraded from the initial ZedBoard platform.

The specification of this FE, as is closely validated within the GNSS-SDR receiver, will be included into D3.2 [3].

2 AUDITOR corrections validation

2.1 TOMION working in real-time at the Central Processing Facility side (public)

The real-time implementation of the AUDITOR Central Processing Facility (CPF) has been set up during December 2017. Since then it has been running in different short sessions, and now continuously (after doubling the hard disk capacity of our server chapman.upc.es). The purpose is to characterize the performance in realistic conditions, without depending on the availability of the final AUDITOR hardware and user software versions. In this way we will be able to identify in advance potential improvements for future upgrades of the main elements of TOMION implementing the WARTK technique in the AUDITOR scenario. We are focusing here on a detailed analysis of the first session, run around the Christmas (since afternoon of 24th December to noon of 26th December, days 357 to 359 of year 2017). We have summarized the results obtained at 1 Hz, showing the equivalent ones at 30 seconds rate.

2.1.1 Real-time WARTK network, users and dates

After studying the stability and latency of the GPS measurements provided by available RTCM GNSS streams, the network of permanent receiver has been selected for supporting AUDITOR in Greece, its target region. It consists of 6 permanent receivers supporting the WARTK CPF: MATE, ORID, KTCH, DYNG, ISTA, and SOFI as the reference receiver for satellite clock estimation and carrier phase double differencing. Moreover the observations of two additional permanent receivers, AUT1 and PVOG, are being ingested as "rover-like" receivers (see Figure 2.1), i.e. without significant weight in the CPF, modelling as kinematic user and with its different, WARTK user ambiguity fixing algorithm (see in particular Hernández-Pajares et al. 2000 [7]). This is a simple way of taking and assessing in real-time the fresh WARTK corrections, in particular differential corrections in the original format modelled by the CPF: satellite clock estimation and ionospheric two-layer grid model corrections. The observations are taken at 1 Hz with a maximum tolerance of 2 seconds of latency (see its distributions in form of number of phase arc for the reference and rover-like receivers, SOFI and AUT1, in Figure 2.2).

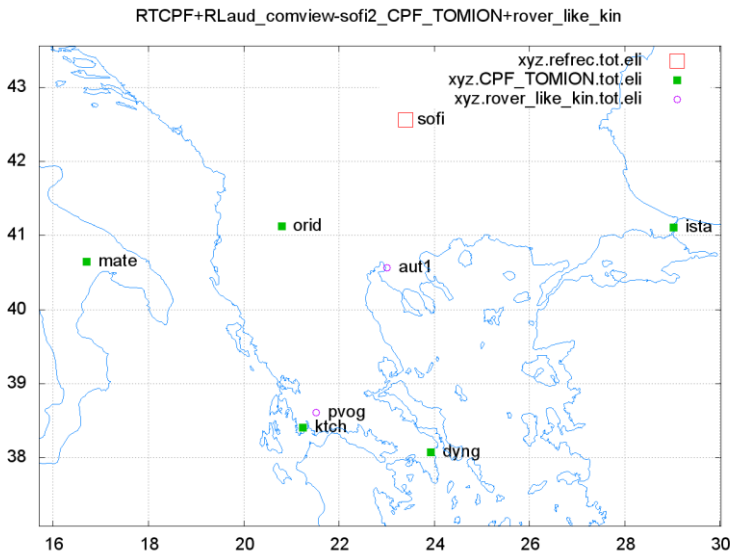

Figure 2.1 Map of the AUDITOR RT permanent GPS stations (green squares), including the reference one (red square) and permanent GPS receivers treated as rover users (magenta circles).

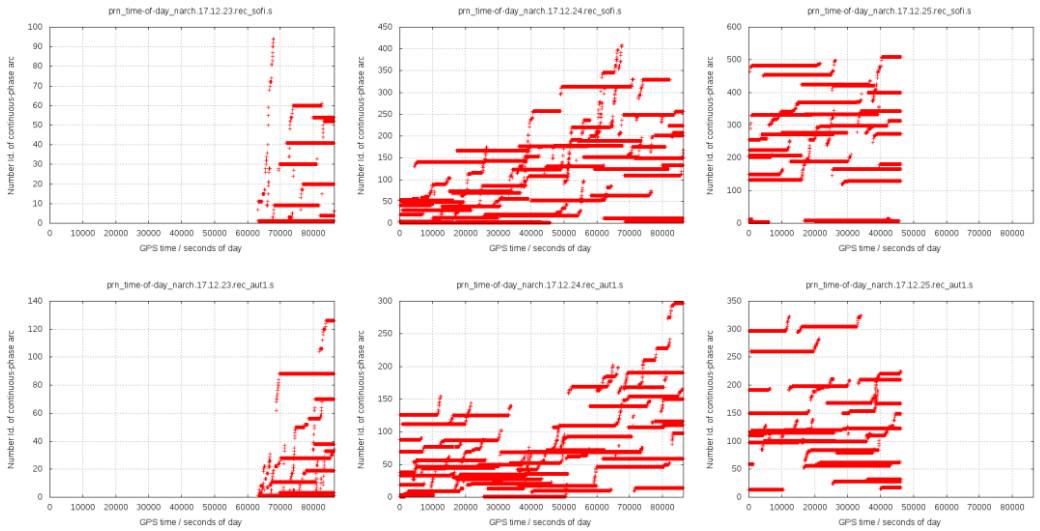

Figure 2.2 Number of continuous arc transmitter-receiver vs time, for the reference GPS receiver SOFI (first row) and for one of the roving users, AUT1 (second row), during the first (starting-up), second and third, and last, days of this RT experiment (days 23, 24 and 25 December 2017, respectively).

2.1.2 Triple differences of prefit residuals

Both the real-time cycle-slip detection (based on the discontinuities of the ionospheric carrier phase and phase-pseudorange Melbourne-Wubbena combinations see for instance Blewitt 1990, [5]) and the modelling of the different observations (first-order-free ionospheric and ionospheric combinations of carrier phase and pseudoranges, Lc, Pc, Li and Pi respectively, and Melbourne-Wubbena combination) can be independently checked by means of the triple differences of Lc (once the receiver positioning is known in advance at cm-error level) regarding to the reference satellite (with highest elevation), reference receiver (SOFI) and consecutive observation times (1 Hz in actual conditions, or 30 seconds in this detailed assessment). Figure 2.3 and Figure 2.4 show that the algorithm works well (just few low elevation observations show undetected cycle-slips).

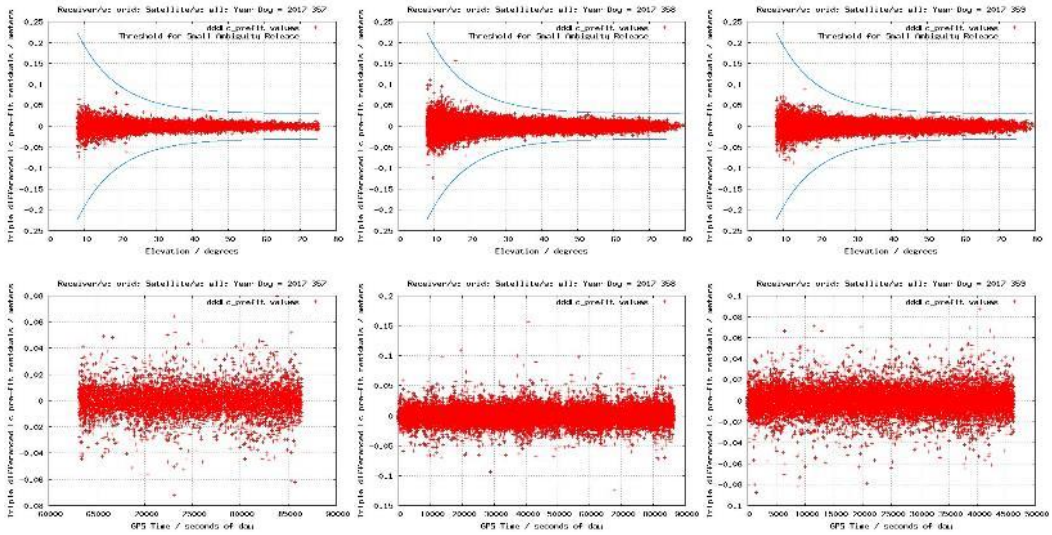

Figure 2.3 Triple differences of ionospheric-free combination of carrier phases for the permanent receiver ORID, vs elevation (first row) and vs time (second row), during the first (starting-up), second and third, and last, days of this RT experiment (days 23, 24 and 25 December 2017, respectively).

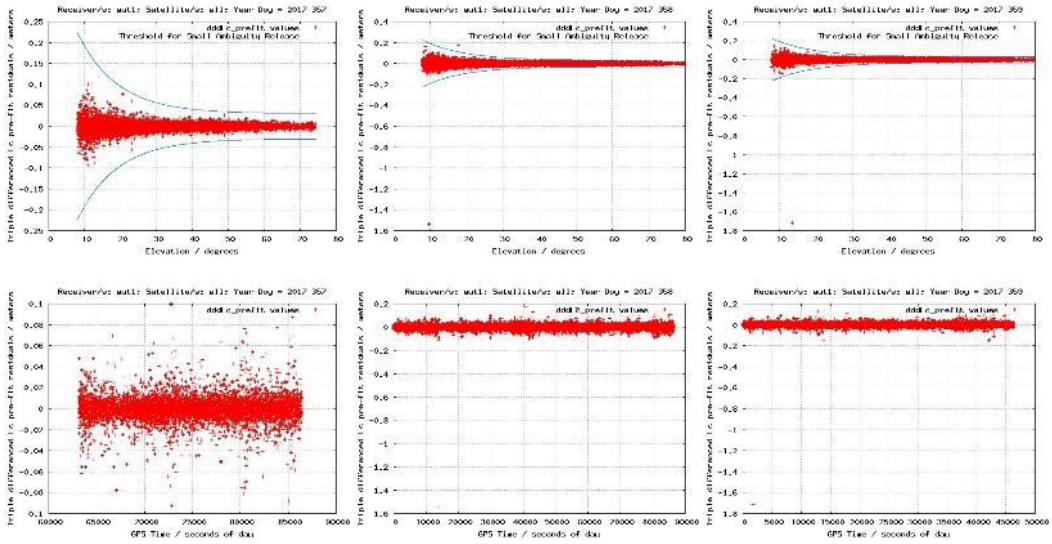

Figure 2.4 Triple differences of ionospheric-free combination of carrier phases for the roving user AUT1, versus elevation (first row) and versus time (second row), during the first (starting-up), second and third, and last, days of this RT experiment (days 23, 24 and 25 December 2017, respectively).

2.1.3 RT GPS satellite clocks estimated by the AUDITOR CPF vs the IGS ones

The implementation of the differential processing is performed by TOMION by means of an undifferenced model, but sharing the receiver clock errors, referred to the permanent receiver clock error, as far as its carrier phase ambiguities, with the users. Then the checking of the satellite clocks estimated by the WARTK CPF is convenient to see the correct functioning of the CPF in spite of this not a target by itself (they should be properly computed from a global GNSS network, not from a regional one). In next figures the real-time satellite clock estimates from AUDITOR WARTK network is compared with the final values estimated globally by the IGS analysis centers. It can be seen in general the remarkable consistency of the results (see Figure 2.5, Figure 2.6, Figure 2.7, Figure 2.8, Figure 2.9 and Figure 2.10).

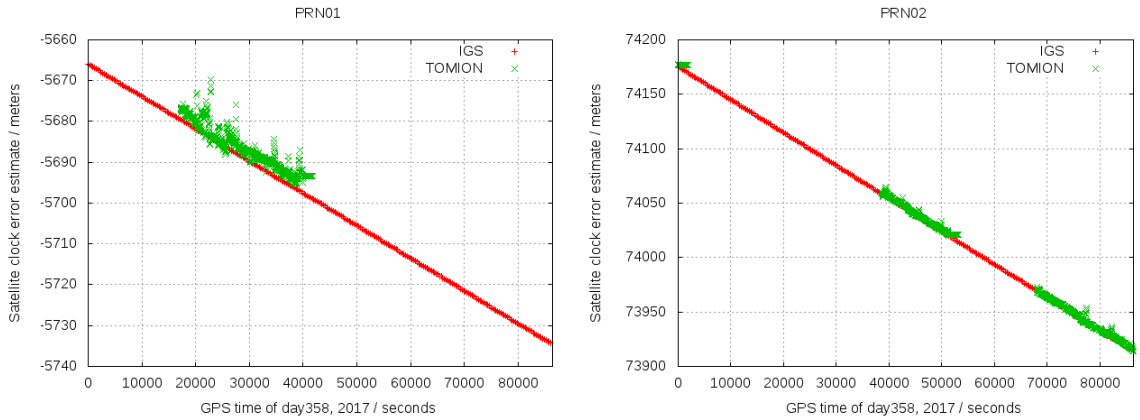

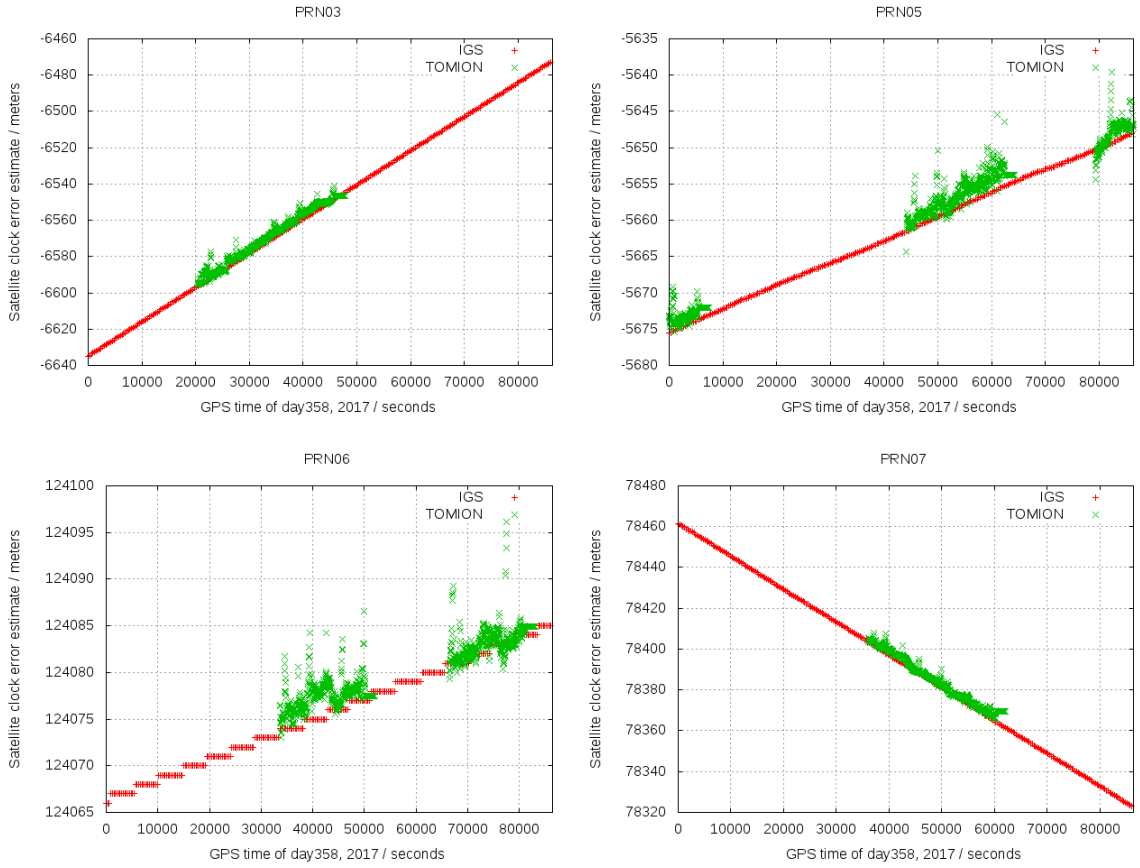

Figure 2.5 Satellite clock offsets for GPS satellites (PRN01, 02, 03, 05, 06 and 07 from left to right and from top to bottom) estimated by the CPF for the different satellites in view (green points) versus the final values computed and combined in post-processed by IGS analysis centers. during the second day of this RT experiment (day 24 December 2017).

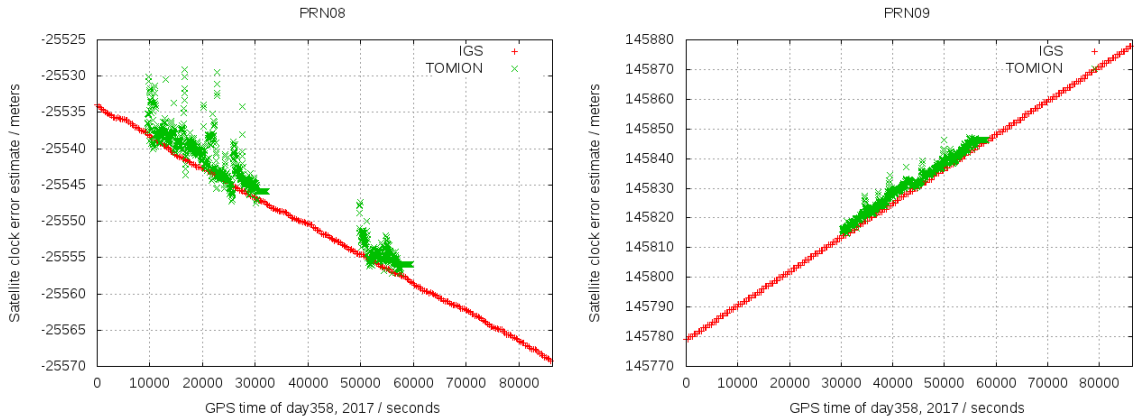

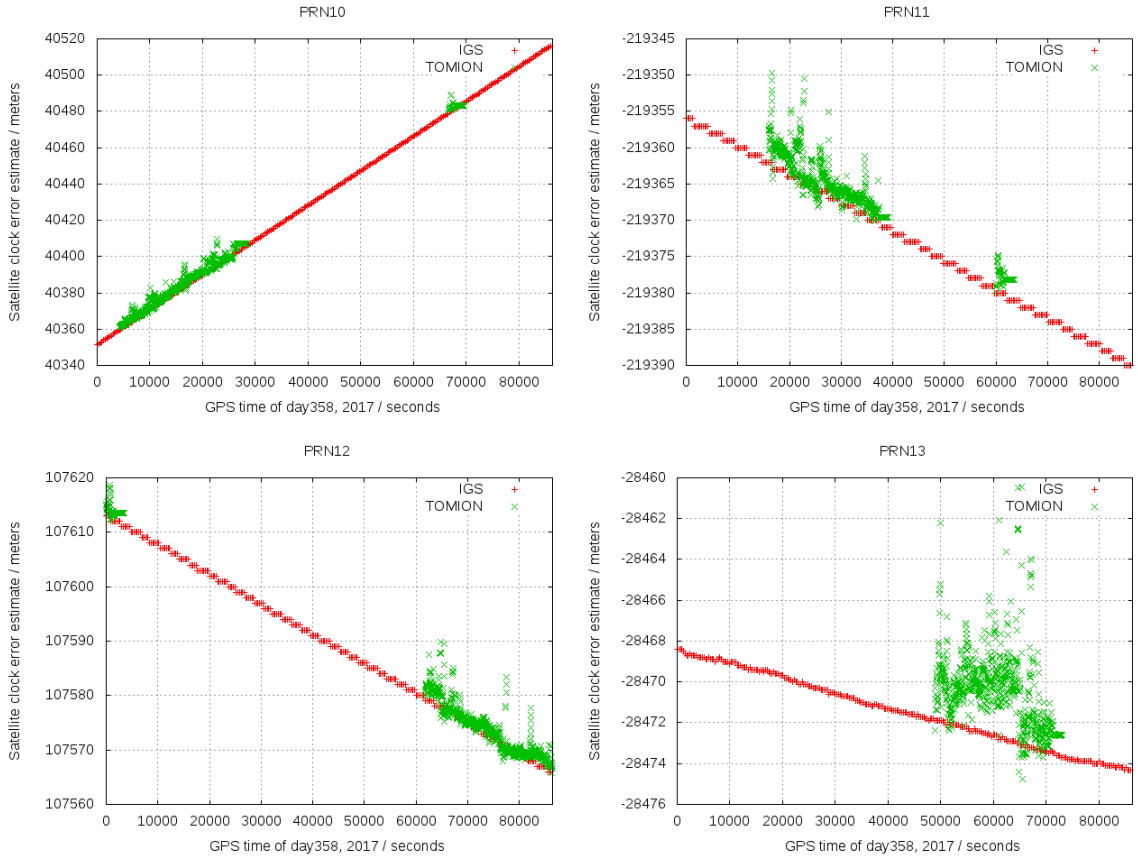

Figure 2.6 Satellite clock offsets for GPS satellites (PRN08, 09, 10, 11, 12 and 13 from left to right and from top to bottom) estimated by the CPF for the different satellites in view (green points) versus the final values computed and combined in post-processed by IGS analysis centers. during the second day of this RT experiment (day 24 December 2017).

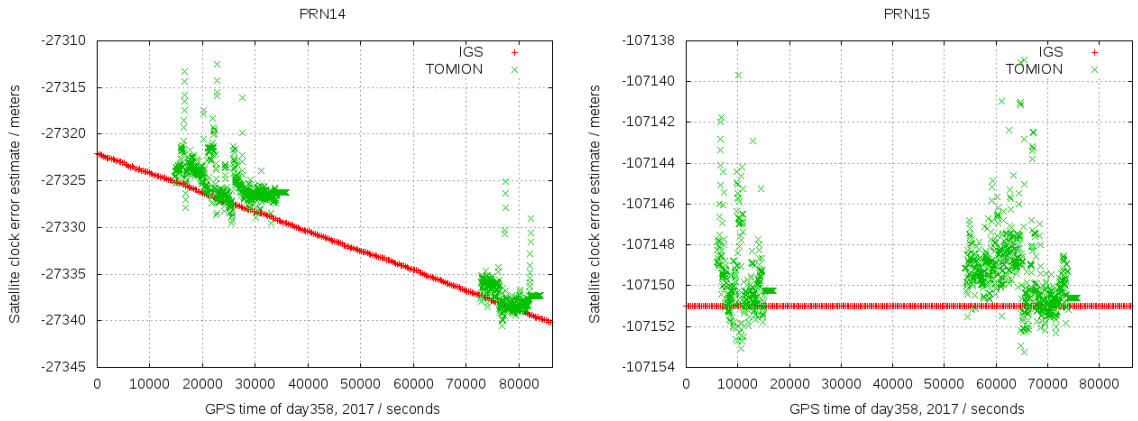

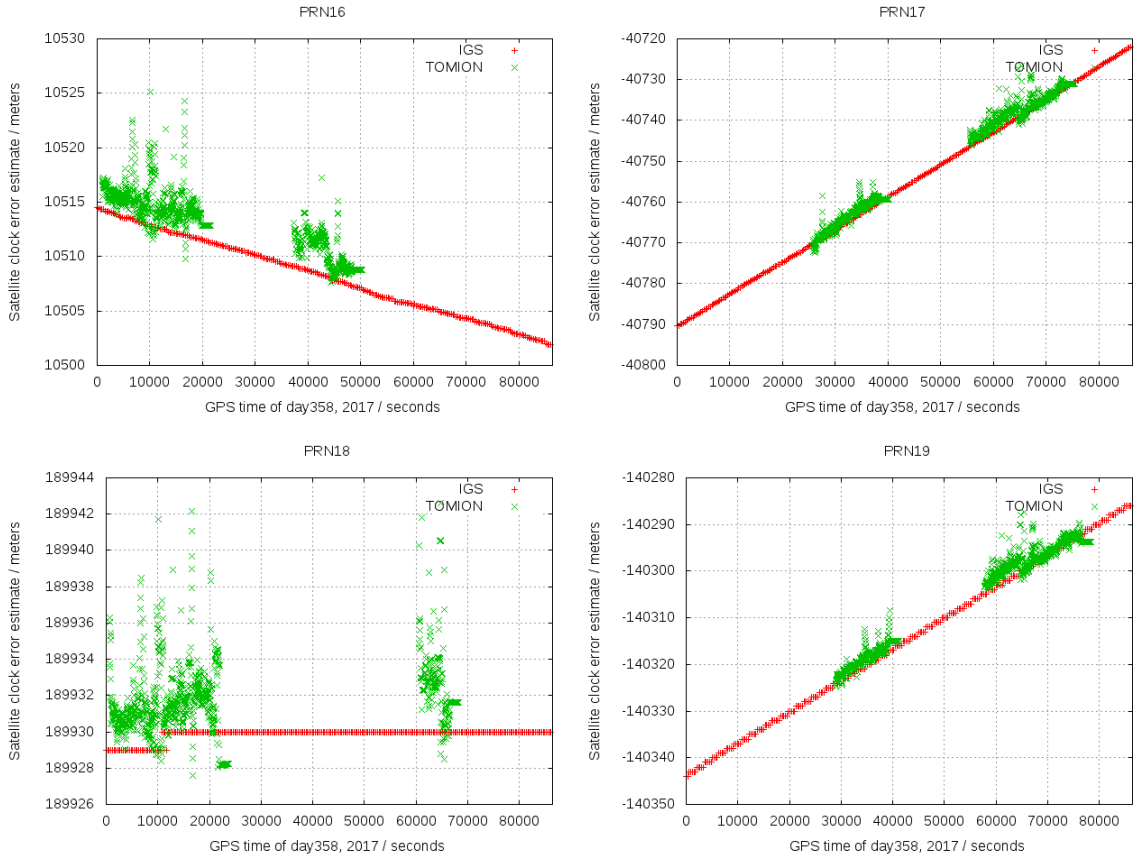

Figure 2.7 Satellite clock offsets for GPS satellites (PRN14, 15, 16, 17, 18 and 19 from left to right and from top to bottom) estimated by the CPF for the different satellites in view (green points) versus the final values computed and combined in post-processed by IGS analysis centers. during the second day of this RT experiment (day 24 December 2017).

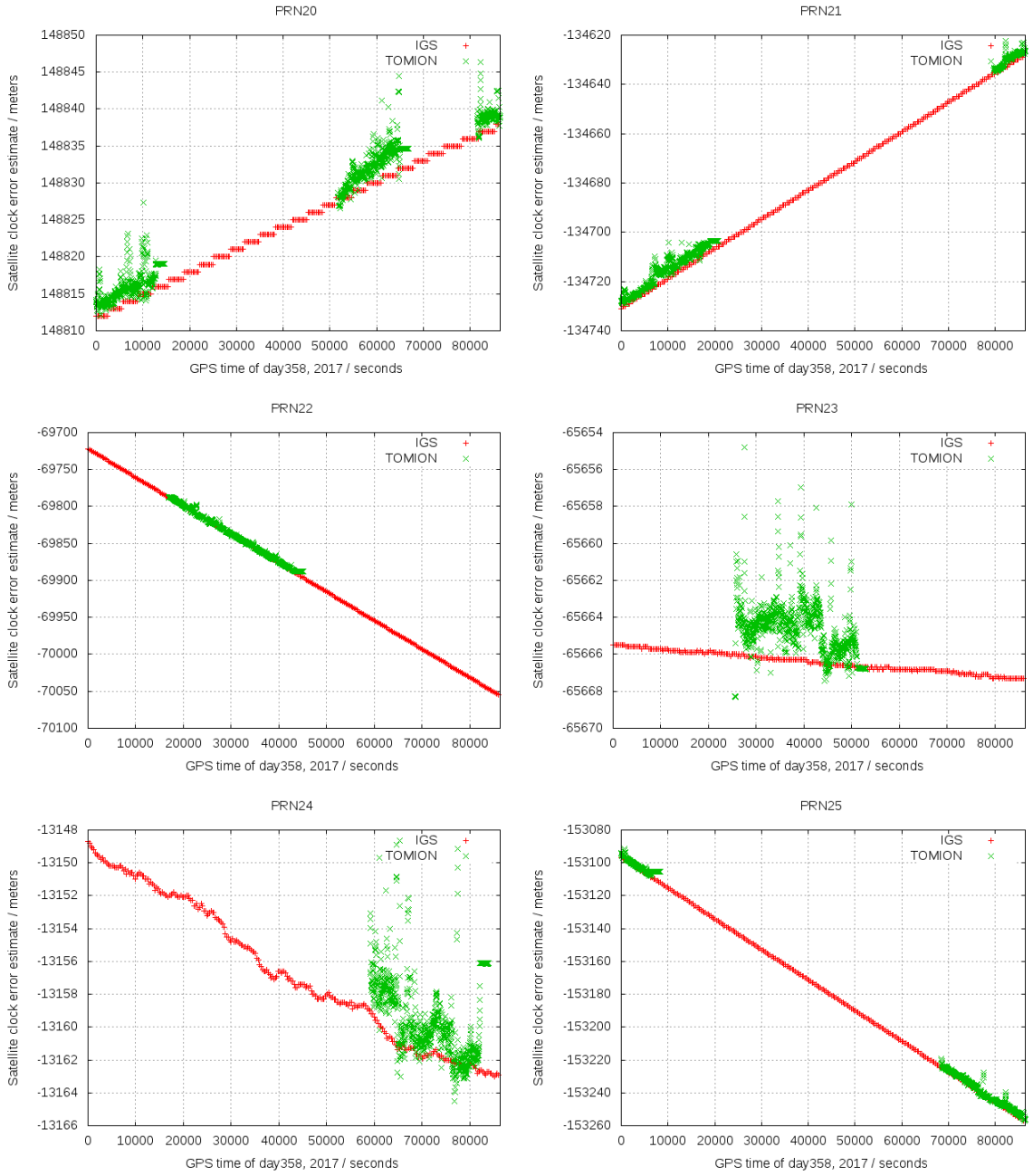

Figure 2.8 Satellite clock offsets for GPS satellites (PRN20, 21, 22, 23, 24 and 25 from left to right and from top to bottom) estimated by the CPF for the different satellites in view (green points) versus the final values computed and combined in post-processed by IGS analysis centers. during the second day of this RT experiment (day 24 December 2017).

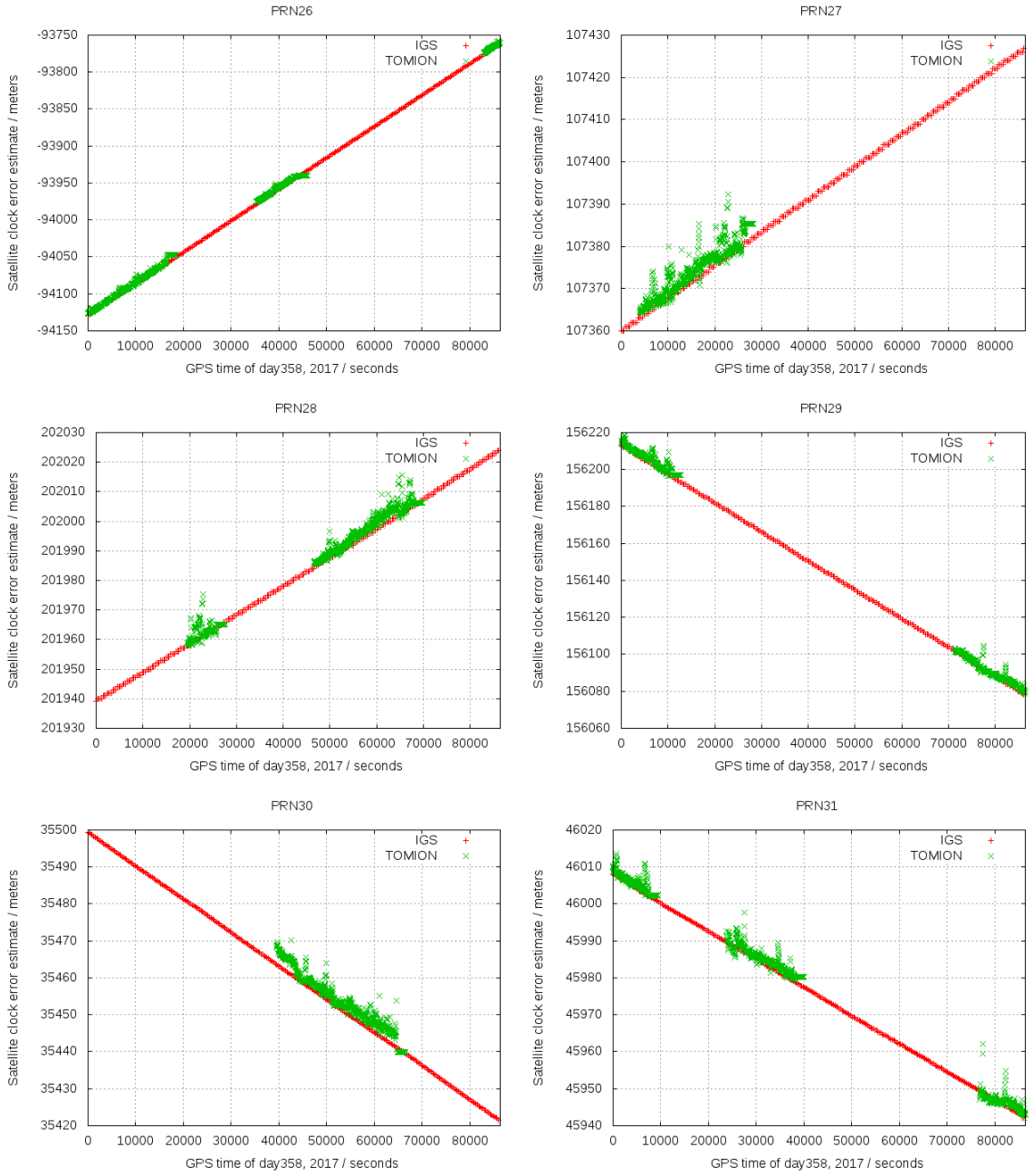

Figure 2.9 Satellite clock offsets for GPS satellites (PRN26, 27, 28, 29, 30 and 31 from left to right and from top to bottom) estimated by the CPF for the different satellites in view (green points) versus the final values computed and combined in post-processed by IGS analysis centers. during the second day of this RT experiment (day 24 December 2017).

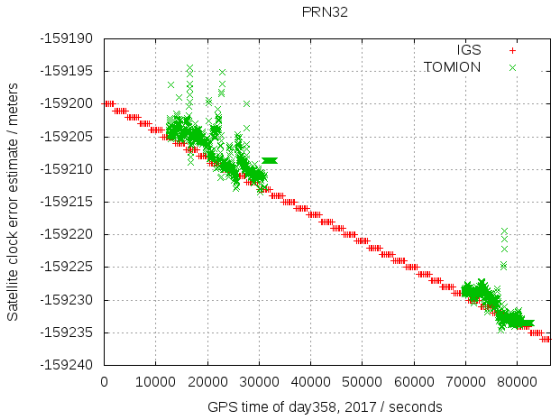

Figure 2.10 Satellite clock offsets for GPS satellites (PRN32 from left to right and from top to bottom) estimated by the CPF for the different satellites in view (green points) versus the final values computed and combined in post-processed by IGS analysis centers. during the second day of this RT experiment (day 24 December 2017).

2.1.4 RT Zenith Tropospheric Delay estimated by the AUDITOR CPF vs the IGS ones

Another real-time product very sensitive to the quality of the CPF processing is the Zenith Tropospheric Delay, estimated as random walk in the CPF filter. It can be seen a noisier but mostly unbiased behavior, when compared with the post-processed global combined solution of IGS (see Figure 2.11) in spite of the limitations in the relative positioning for ZTD determination. On the other hand it can be seen (Figure 2.12) the very challenging ZTD estimation by the two users, where the effect of the warm start of the roving user filter (all the unknowns treated as white noise each 3 hours) is evident, and a first guess of the convergence time can be seen in terms of ZTD.

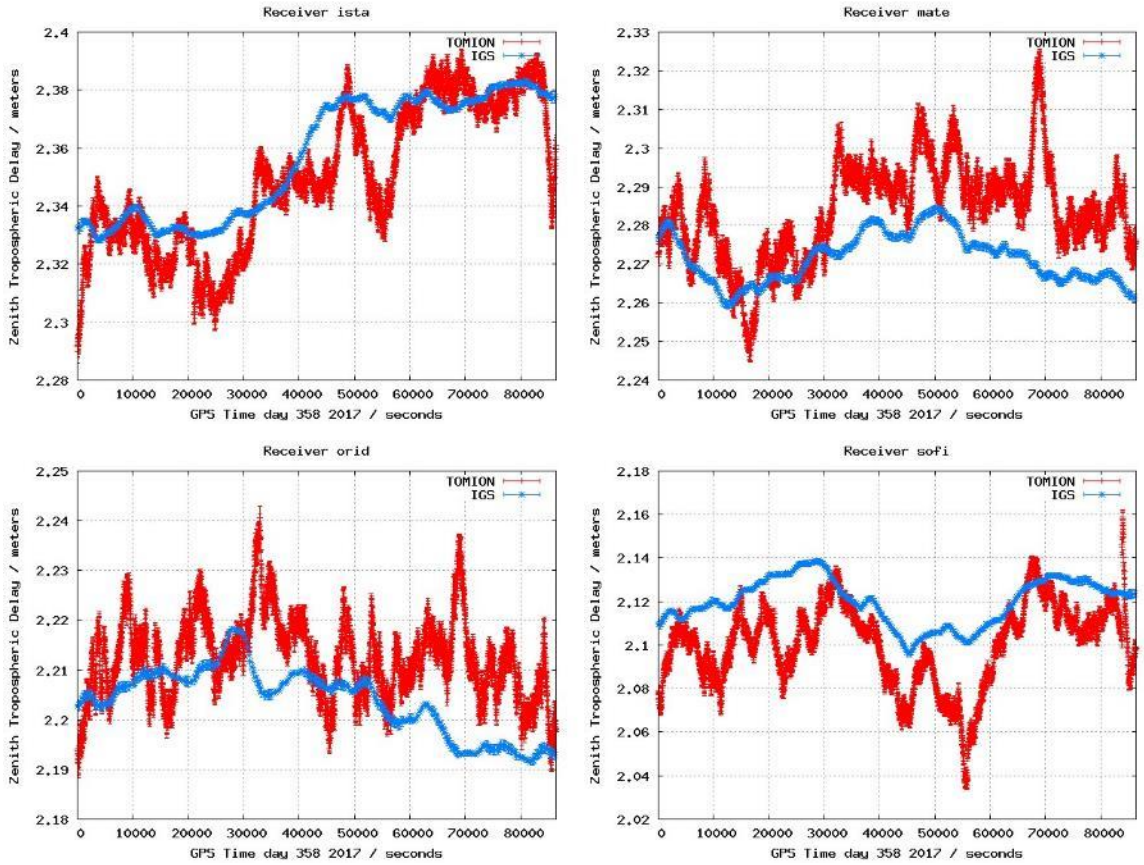

Figure 2.11 Zenith Tropospheric Delay estimated in RT by the AUDITOR CPF (red) for permanent receivers with available final IGS estimation (blue), from left to right and from top to bottom the receivers ISTA, MATE, ORID and SOFI, during the second day of this RT experiment (24 December 2017).

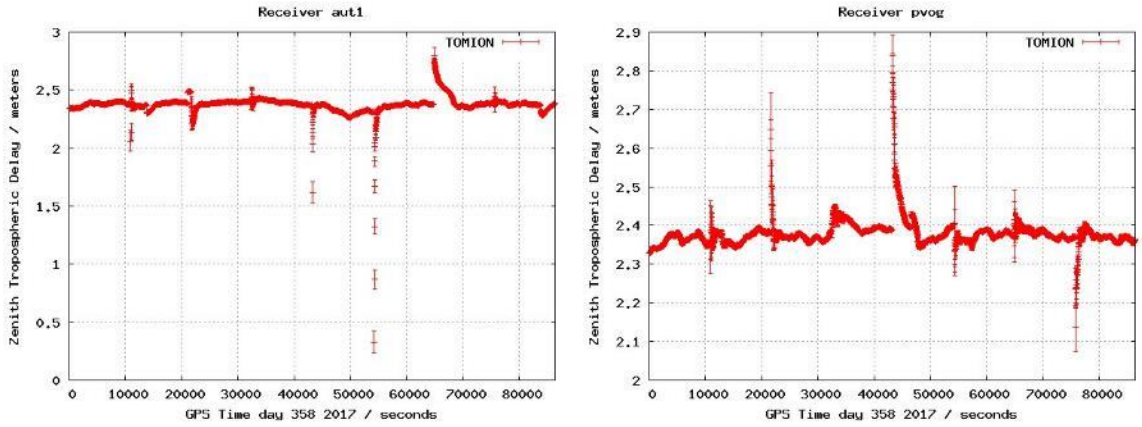

Figure 2.12 Zenith Tropospheric Delay estimated in RT by the WARTK users of AUDITOR, AUT1 (left) and PVOG (right), during the second day of this RT experiment (day 24 December 2017).

2.1.5 RT Vertical Total Electron Content (VTEC) estimated by the AUDITOR CPF vs the presently more accurate IGS GIM (UQRG)

WARTK is a hybrid model combining in a synergic way the "geometric", non-frequency dependent, model and the ionospheric, frequency dependent, one. In order to assess the accuracy of the RT ionospheric determination, a comparison of the RT-VTEC, obtained from vertical summation within the tomographic grid, with the post-processed VTEC provided by one of the best, or the best presently VTEC GIMs in IGS (Roma-Dollase et al. 2017, [11]), is shown in Figure 2.13. This GIM is computed daily by UPC-IonSAT with Id. "UQRG", combining tomography with kriging interpolation, and distributed from IGS servers. The RT STECs vs time and elevation for the overall receivers are shown in Figure 2.14 and Figure 2.15 respectively.

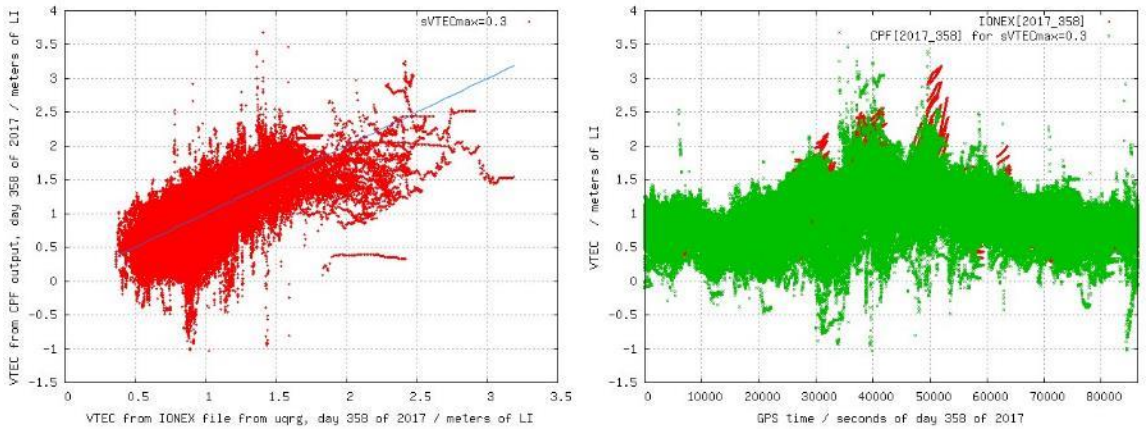

Figure 2.13 In the left-hand plot the VTEC estimated in RT by the CPF (vertical axis) vs the reference value provided by the post-processed Global Ionospheric Map (GIM) UQRG (horizontal axis, both in meters of LI=L1-L2) is represented, and the corresponding time evolution (in green and red, respectively) is shown at the right-hand plot, both during the second day of this RT experiment (day 24 December 2017).

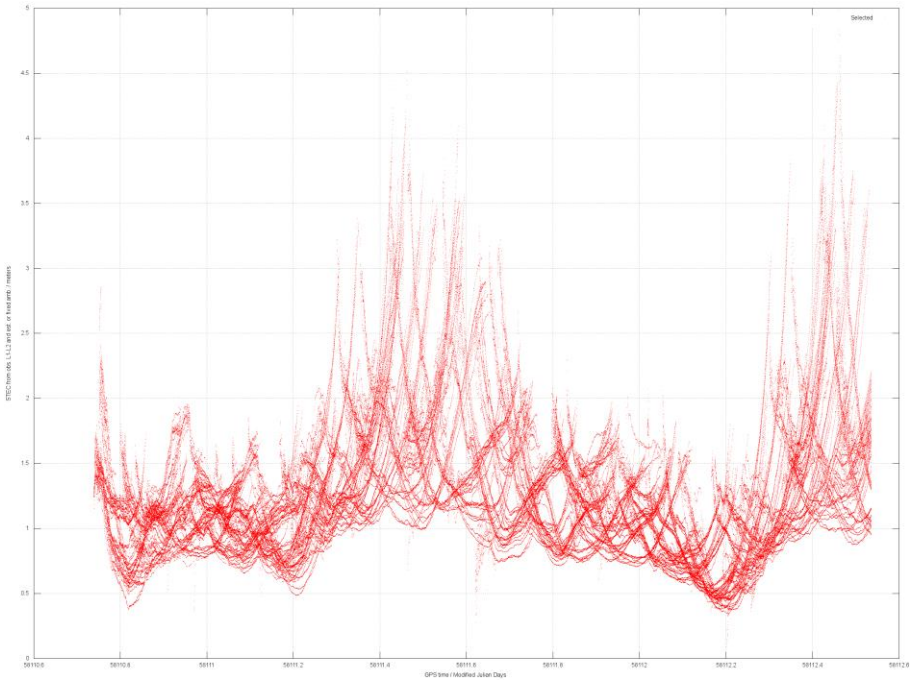

Figure 2.14 STEC estimated in RT by the CPF (vertical axis in meters of LI=L1-L2) vs time (horizontal axis in modified julian days) is represented, during the whole RT experiment (days 23, 24 and 25 December 2017).

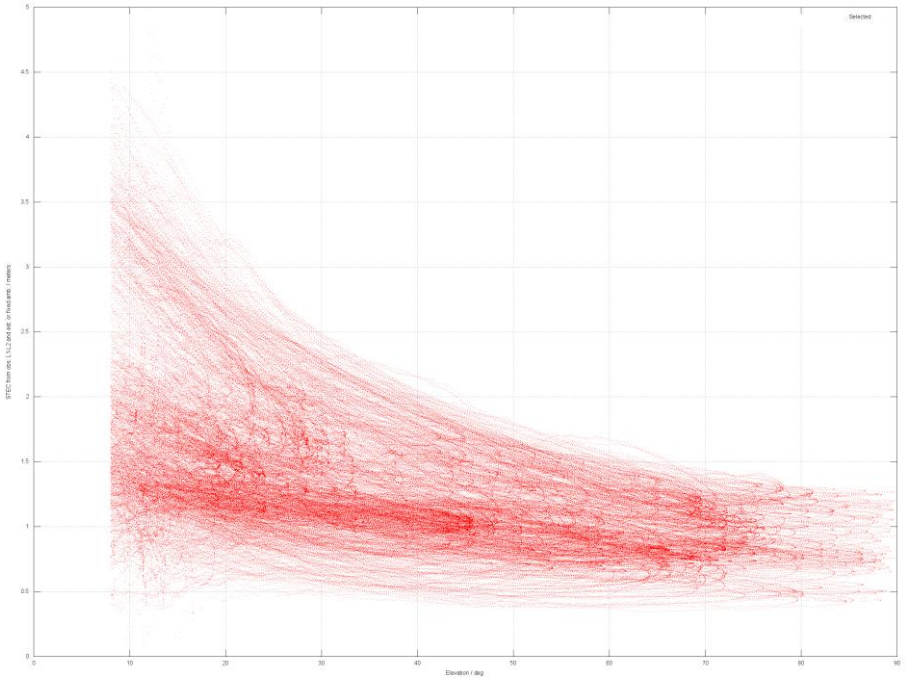

Figure 2.15 STEC estimated in RT by the CPF (vertical axis in meters of LI=L1-L2) vs elevation angle above the horizon (horizontal axis in degrees) is represented, during the whole RT experiment (days 23, 24 and 25 December 2017).

2.1.6 RT VTEC model fitted independently for each satellite in view from the RT WARTK AUDITOR estimation (broadcasted as message DSM)

The ionospheric corrections are broadcast to the users in terms of an independent linear fit of the VTEC per satellite, from the STECs determined in RT for the permanent receivers by the WARTK model (implemented in terms of the DSM message). The bias and RMS of such fitting, and the residuals themselves, are shown in Figure 2.16, Figure 2.17 and Figure 2.18 for the central day. They are reasonable, excepting from 45000 to 60000 seconds (see discussion below). The time evolution of the three coefficients per satellite are also shown in Figure 2.19, Figure 2.20, Figure 2.21, Figure 2.22, Figure 2.23 and Figure 2.24.

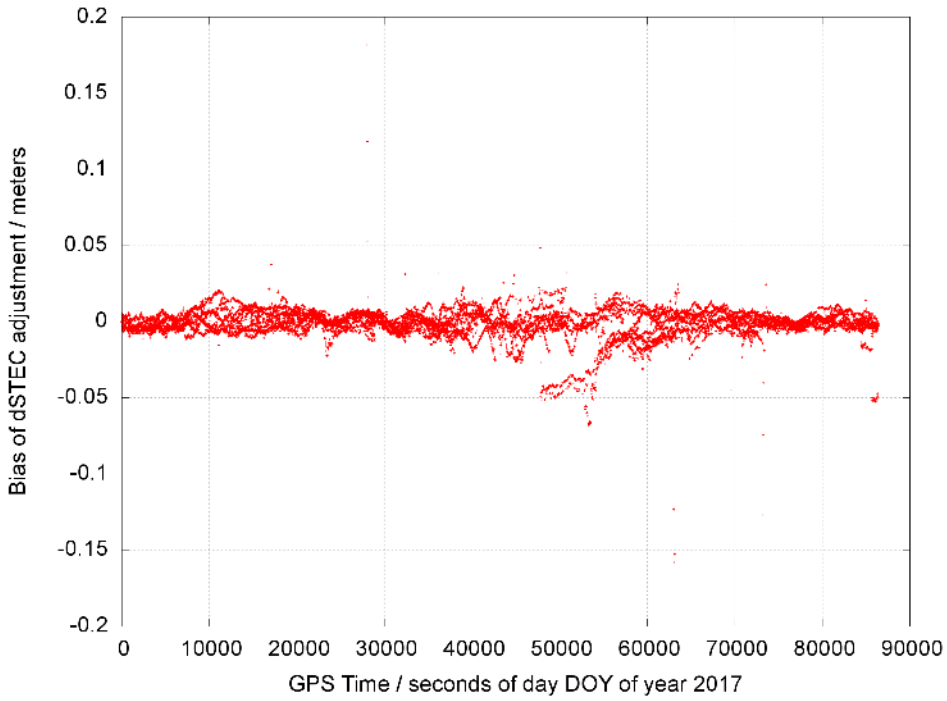

Figure 2.16 The bias of the residuals of the VTEC fitting per satellite (vertical axis in meters of LI=L1-L2) vs time (horizontal axis in seconds of the day) is represented, during the second day of the RT experiment (day 24 December 2017).

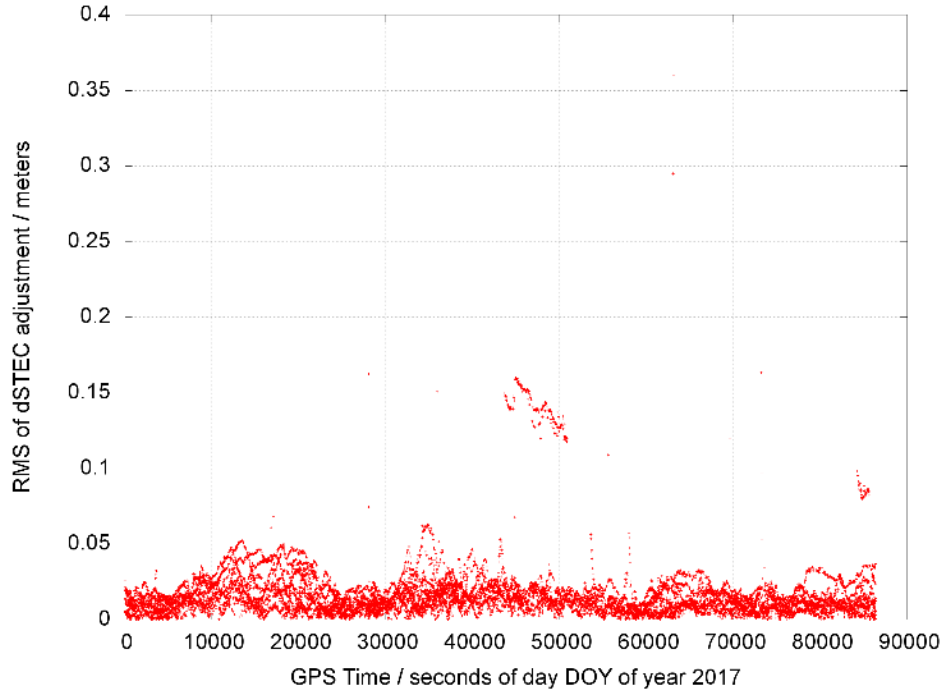

Figure 2.17 The RMS of the residuals of the VTEC fitting per satellite (vertical axis in meters of LI=L1-L2) vs time (horizontal axis in seconds of the day) is represented, during the second day of the RT experiment (day 24 December 2017).

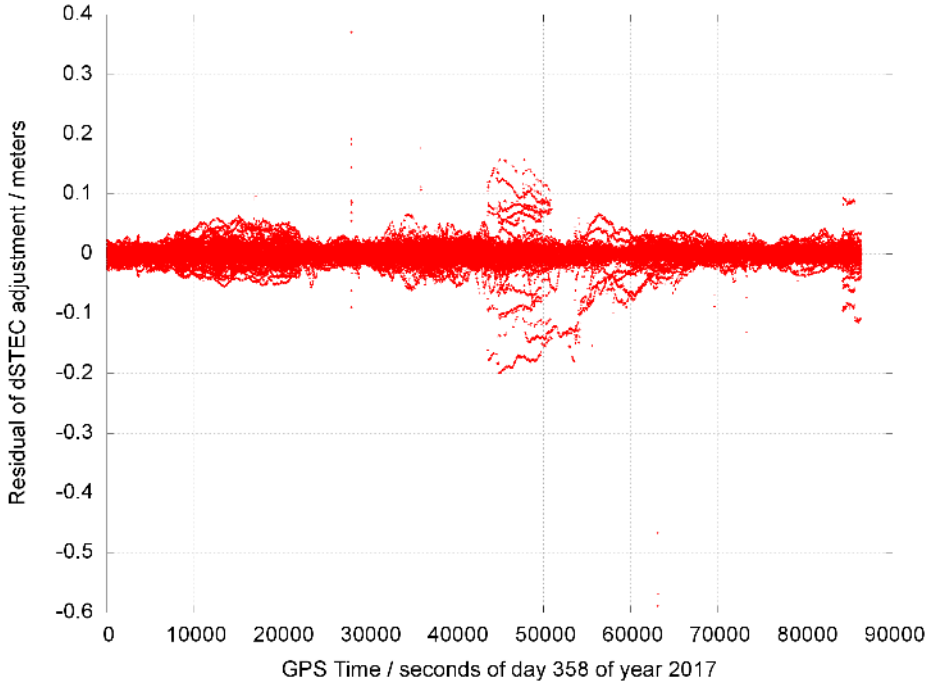

Figure 2.18 Residuals of the VTEC fitting per satellite (vertical axis in meters of LI=L1-L2) vs time (horizontal axis in seconds of the day) is represented, during the second day of the RT experiment (day 24 December 2017).

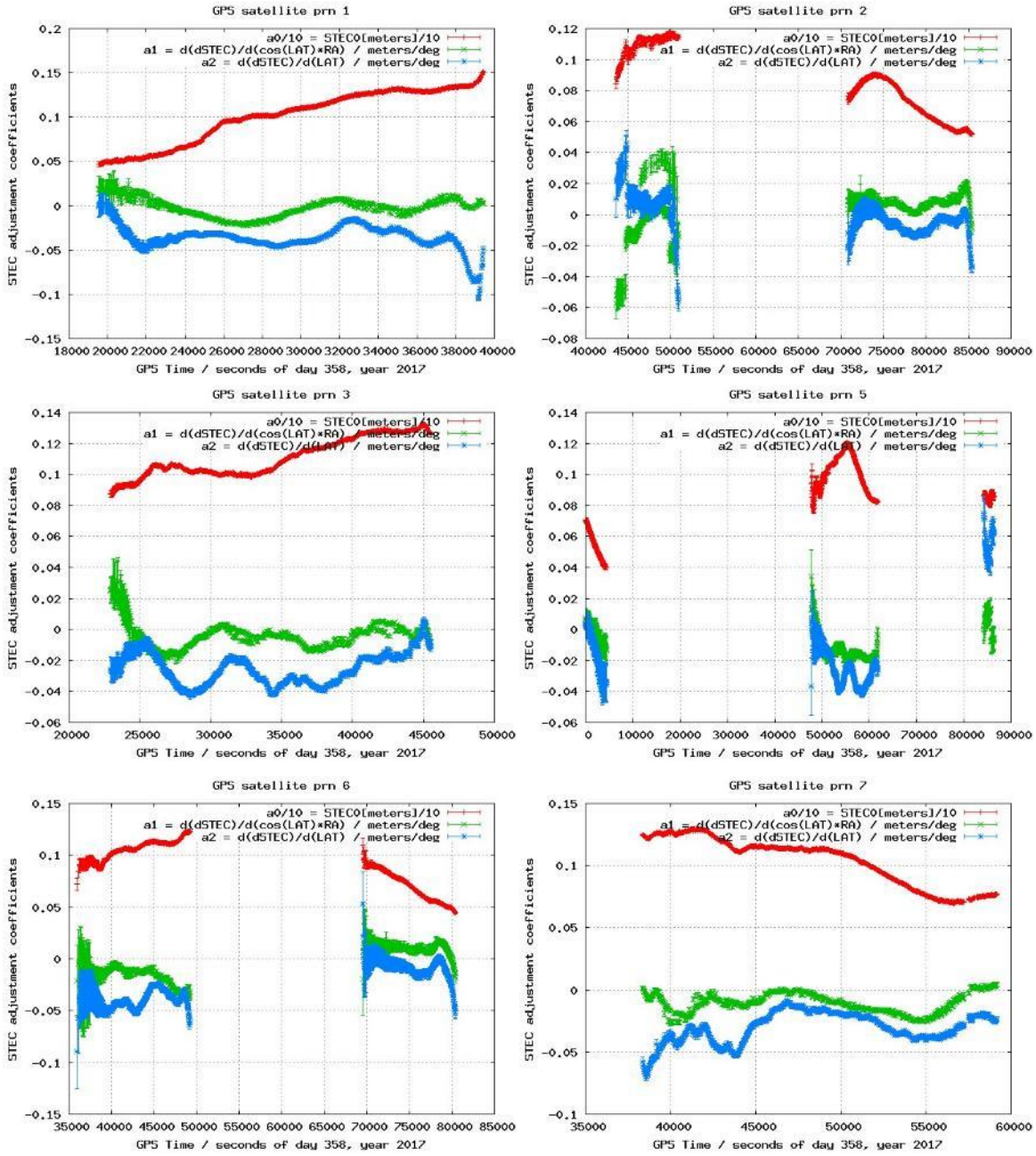

Figure 2.19 Coefficients of the VTEC fitting per satellite (vertical axis) vs time (horizontal axis in seconds of the day) is represented, from left to right and from top to bottom, for satellites PRN01, 02, 03, 05, 06 and 07, during the second day of the RT experiment (day 24 December 2017).

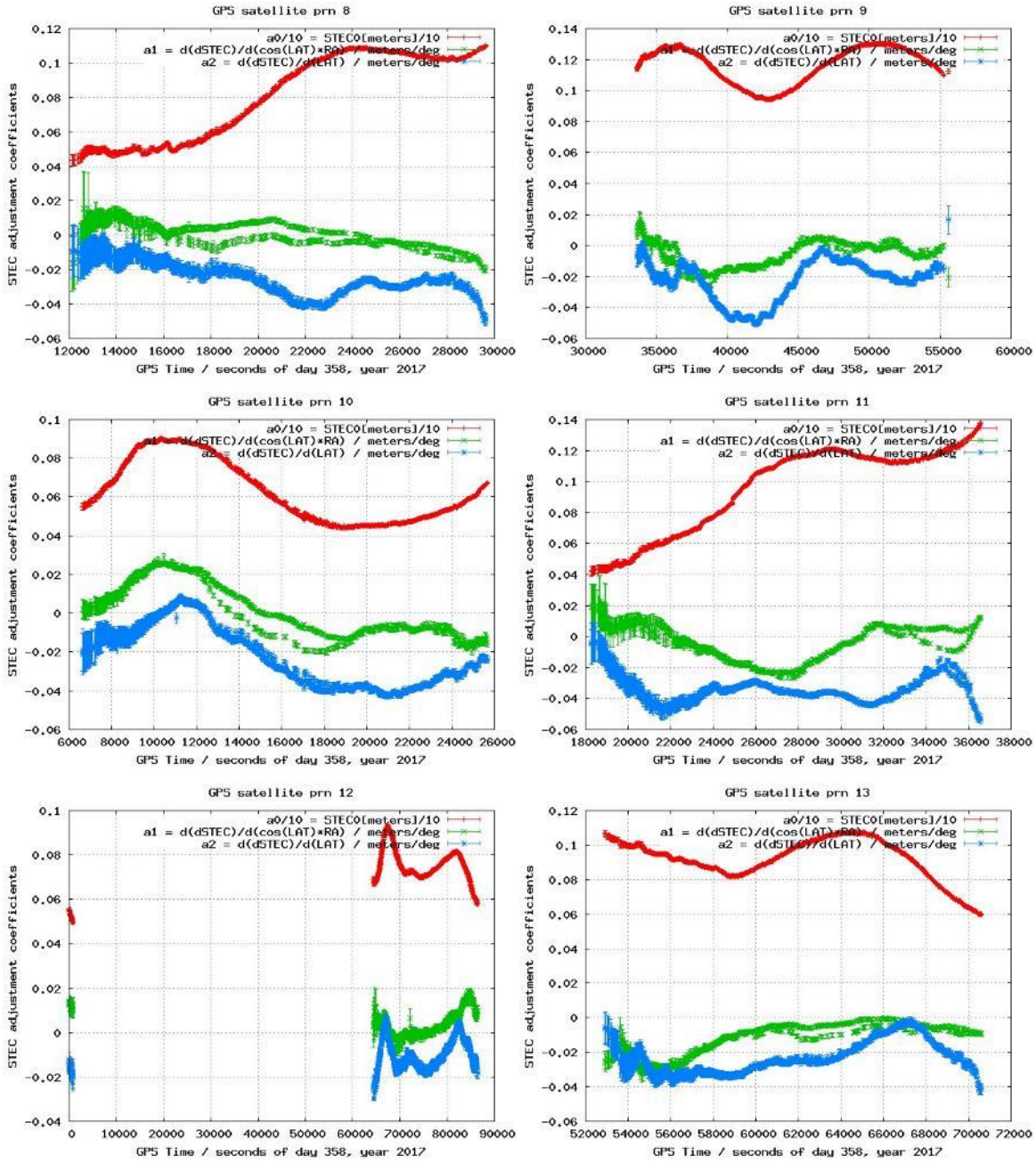

Figure 2.20 Coefficients of the VTEC fitting per satellite (vertical axis) vs time (horizontal axis in seconds of the day) is represented, from left to right and from top to bottom, for satellites PRN08, 09, 10, 11, 12 and 13, during the second day of the RT experiment (day 24 December 2017).

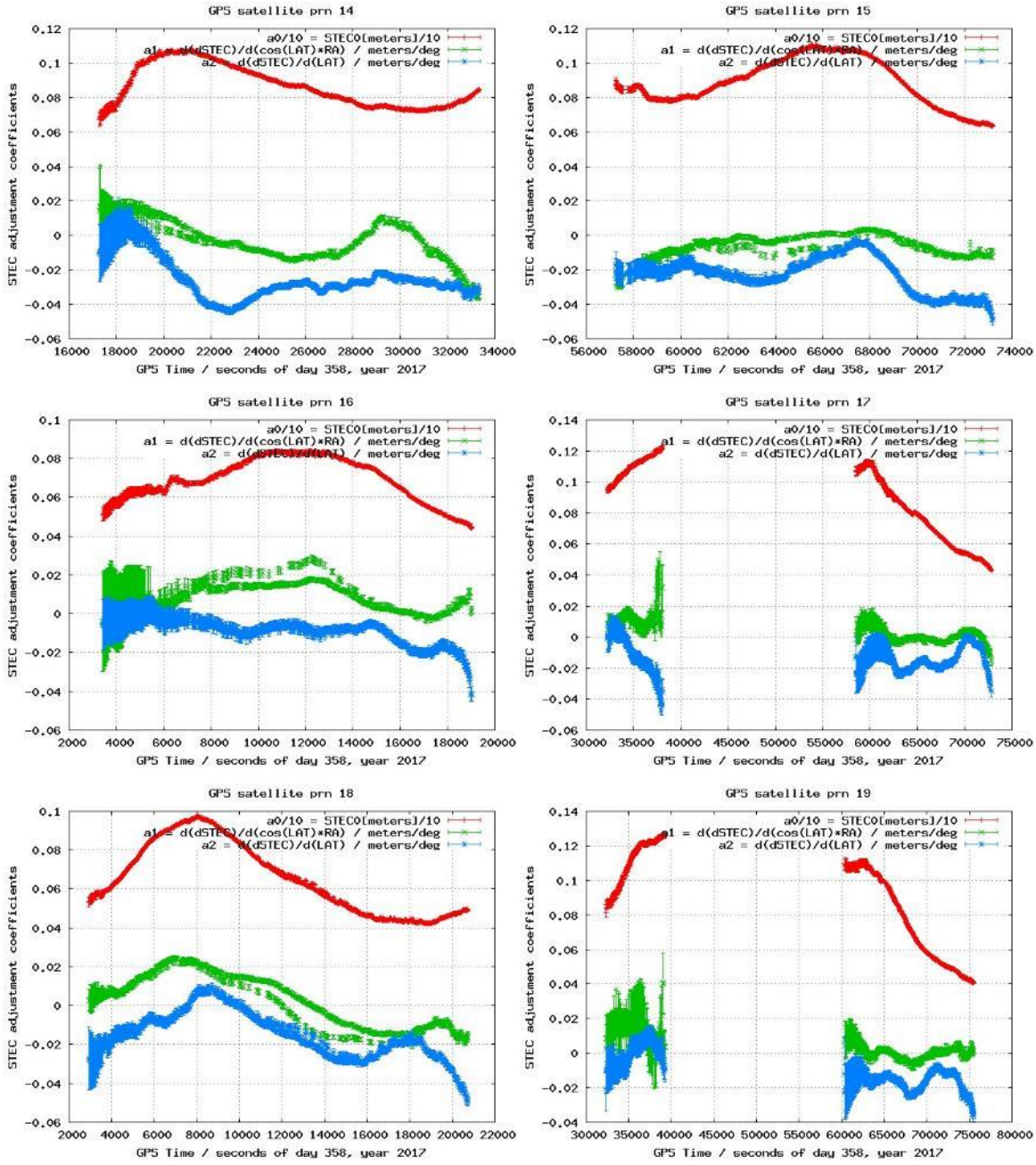

Figure 2.21 Coefficients of the VTEC fitting per satellite (vertical axis) vs time (horizontal axis in seconds of the day) is represented, from left to right and from top to bottom, for satellites PRN14, 15, 16, 17, 18 and 19, during the second day of the RT experiment (day 24 December 2017).

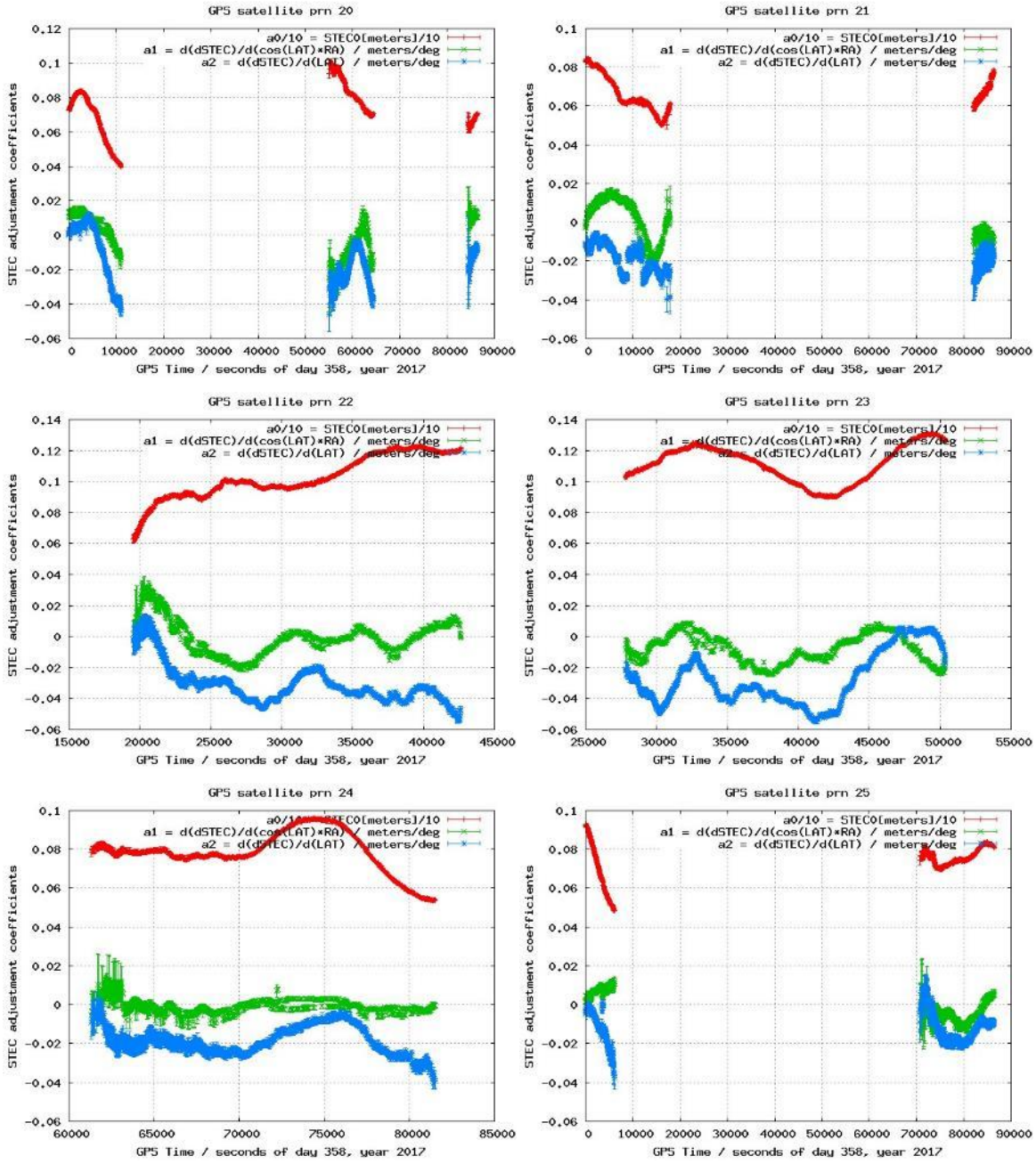

Figure 2.22 Coefficients of the VTEC fitting per satellite (vertical axis) vs time (horizontal axis in seconds of the day) is represented, from left to right and from top to bottom, for satellites PRN20, 21, 22, 23, 24 and 25, during the second day of the RT experiment (day 24 December 2017).

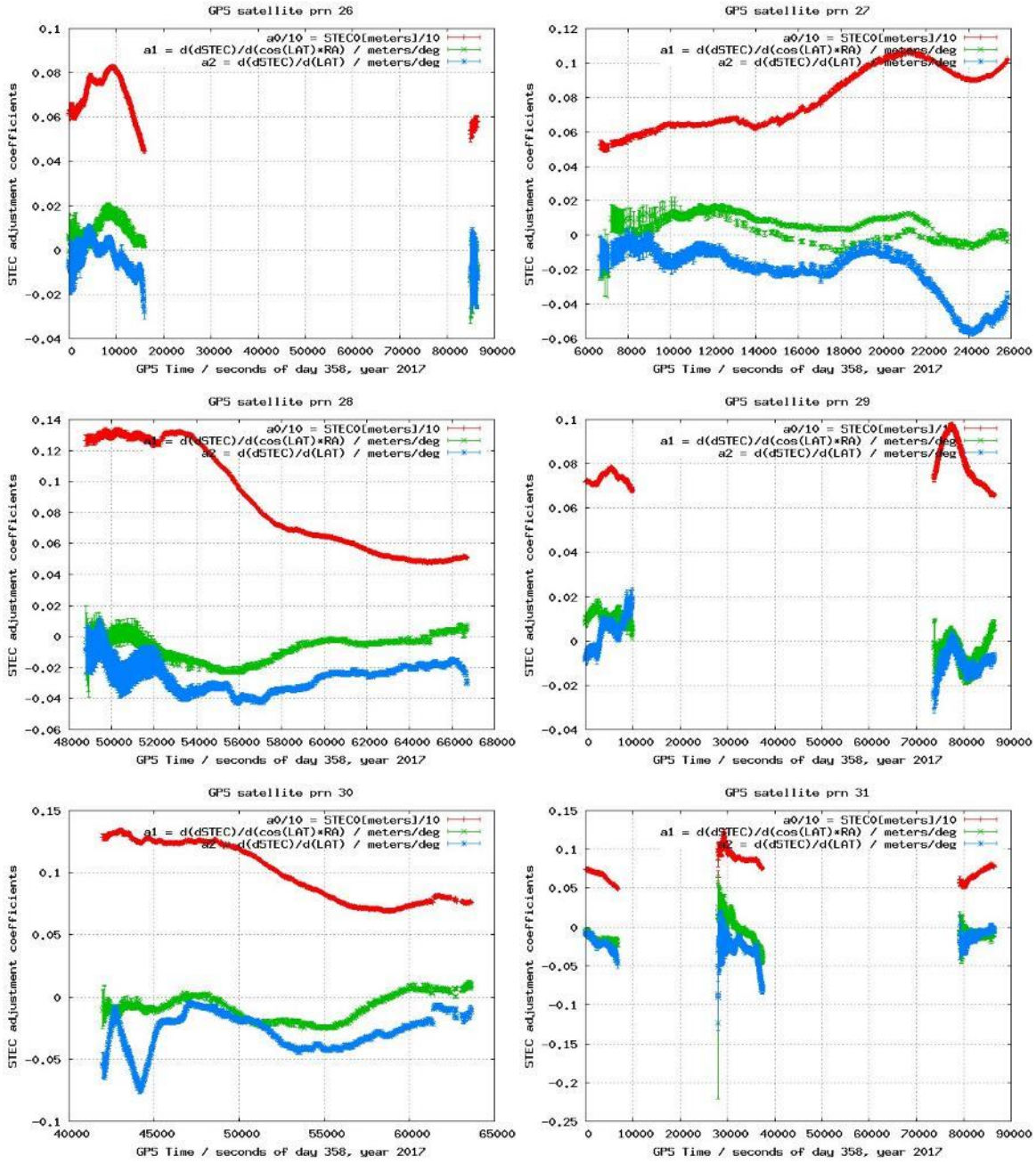

Figure 2.23 Coefficients of the VTEC fitting per satellite (vertical axis) vs time (horizontal axis in seconds of the day) is represented, from left to right and from top to bottom, for satellites PRN26, 27, 28, 29, 30 and 31, during the second day of the RT experiment (day 24 December 2017).

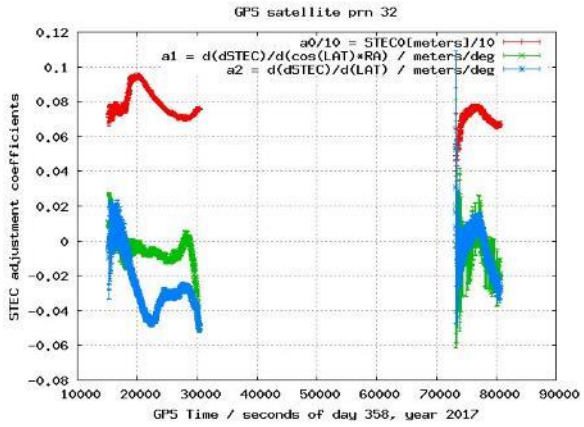

Figure 2.24 Coefficients of the VTEC fitting per satellite (vertical axis) vs time (horizontal axis in seconds of the day) is represented, from left to right and from top to bottom, for satellite PRN32, during the second day of the RT experiment (day 24 December 2017).

2.1.7 RT double-differenced carrier phase ambiguity fixing for the roving user AUT1 and for one typical permanent receiver (ORID)

A summary of the carrier phase ambiguity fixing is provided in this section. In Figure 2.25, the selected reference satellite (the one with highest elevation in the RT implementation) is represented versus time. In Figure 2.26 the double differenced ambiguity determined from the ionospheric-free and ionospheric ambiguities Bc and Bi is represented vs the values directly obtained from the Melbourne-Wübbena combination, for the roving user AUT1 and the permanent receiver ORID. It can be seen a good agreement, especially for the permanent receiver, as expected. The corresponding differences are represented versus elevation in Figure 2.27 and versus time in Figure 2.28. The widelane ambiguity fixing is reached sometimes up to 100%, and the second ambiguity to be fixed (see for instance Hernandez-Pajares et al. 2000), the narrowlane, is fixed up to 60% approximately (Figure 2.29).

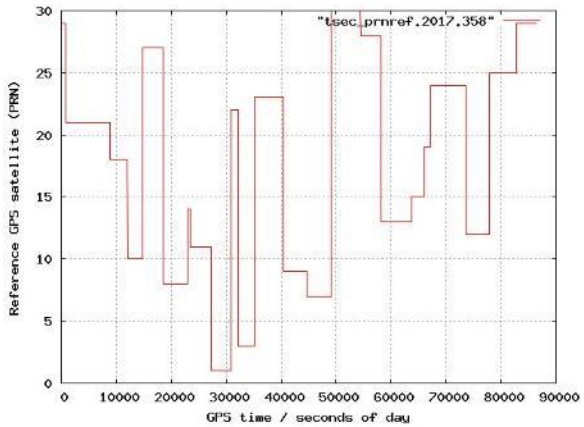

Figure 2.25 PRN of the GPS reference satellite selected in RT to form the double differences (the one available with maximum elevation seen from the reference receiver SOFI) versus time during the second day of the RT experiment (day 24 December 2017).

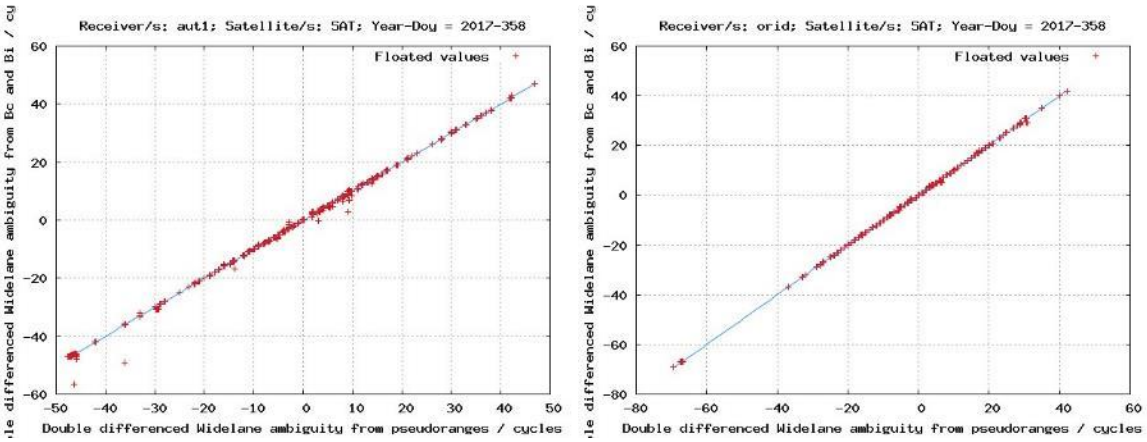

Figure 2.26 Double differenced widelane ambiguity, derived from the ionospheric-free and geometric-free double-differenced ambiguities, versus the value provided by the double-differenced ionospheric and geometric-free Melbourne-Wübbena combination, in cycles: left-hand plot correspond to the roving receiver AUT1 and the right-hand plot to the permanent receiver ORID, both during the second day of the RT experiment (day 24 December 2017).

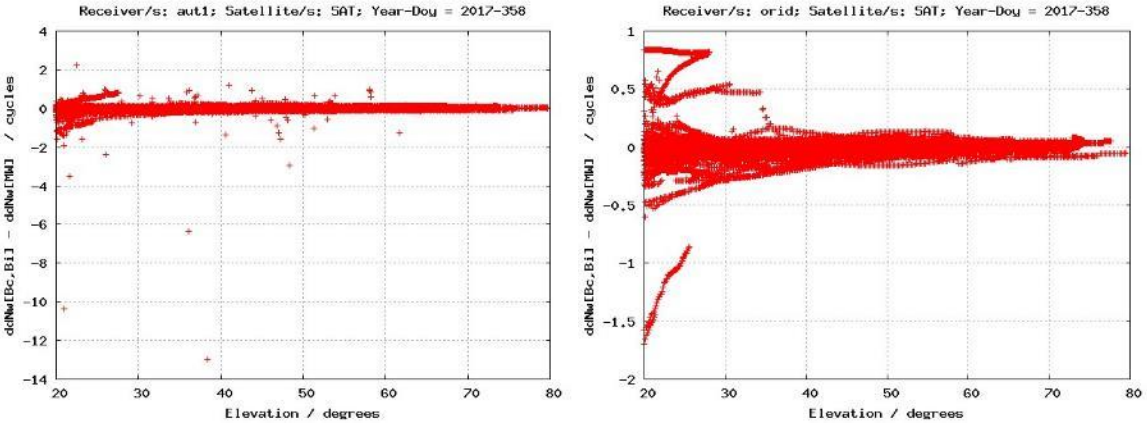

Figure 2.27 Difference of the double differenced widelane ambiguity, derived from the ionospheric-free and geometric-free double-differenced ambiguities, minus the value provided by the double-differenced ionospheric and geometric-free Melbourne-Wübbena combination, in cycles, versus elevation angle: left-hand plot correspond to the roving receiver AUT1 and the right-hand plot to the permanent receiver ORID, both during the second day of the RT experiment (day 24 December 2017).

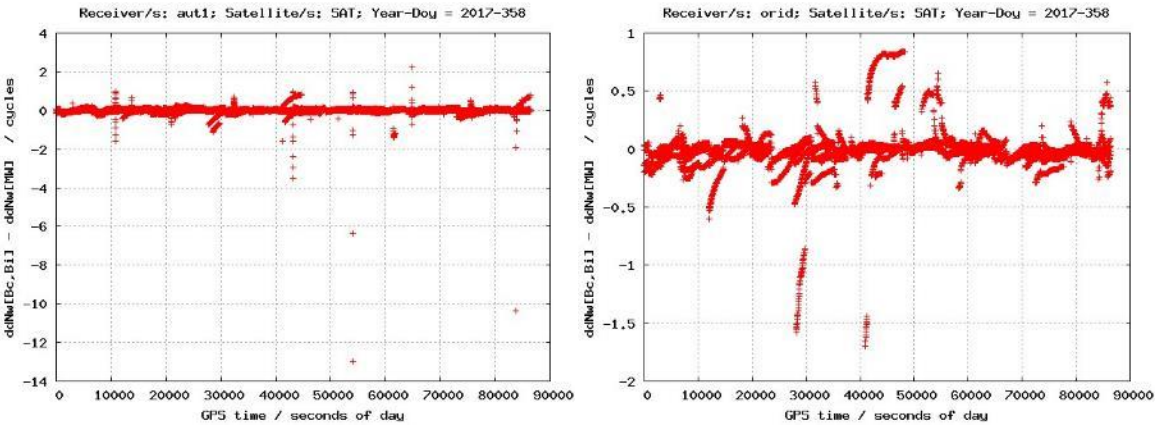

Figure 2.28 Difference of the double differenced widelane ambiguity, derived from the ionospheric-free and geometric-free double-differenced ambiguities, minus the value provided by the double-differenced ionospheric and geometric-free Melbourne-Wübbena combination, in cycles, versus time: left-hand plot correspond to the roving receiver AUT1 and the right-hand plot to the permanent receiver ORID, both during the second day of the RT experiment (day 24 December 2017).

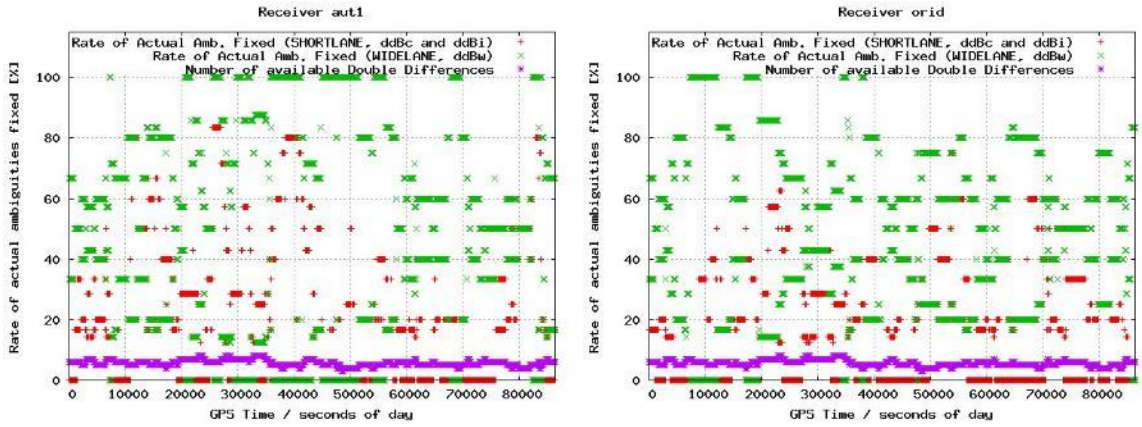

Figure 2.29 Percentage of RT double differenced carrier phase ambiguity fixing (widelane in green, narrowlane in red), and number of available double-differences (in magenta) are represented versus time: left-hand plot correspond to the roving receiver AUT1 and the right-hand plot to the permanent receiver ORID, both during the second day of the RT experiment (day 24 December 2017). Notice that the ambiguity fixing rate correspond just to the ambiguities which are questioned by the CPF (not previously fixed or becoming doubtful). The ambiguities already fixed and not doubtful, are not accounted for.

2.1.8 RT 3D-positioning error for the roving users (AUT1 and PVOG)

The positioning performance of both roving receivers, AUT1 and PVOG at 223 km and 465 km of the reference receiver SOFI (and at 196 km and 33 km from the closer reference receivers, respectively, ORID and KTCH) is shown in Figure 2.30, which can be compared when no ionospheric corrections and no corresponding user ambiguity fixing are used, in Figure 2.31. It is evident the much better performance of WARTK for both users, in general, in terms of convergence time (and final accuracy achieved) after each user cold start, compared when the ionospheric information is not used by the users. carrier-phase relative positioning technique. The exception happens since 43000 to about 70000 seconds for AUT1 (and up to 54000 for PVOG), coinciding with the anomalous high residuals in the spatially linear VTEC fitting per satellite (Figure 2.18), but not clearly seen in the ambiguity fixing information shown in Figure 2.28 and Figure 2.29. A summary of the performance in convergence time and final accuracy, achieved when using or not ionospheric corrections, can be seen in Figure 2.33 (AUT1) and Figure 2.34 (PVOG). It can be seen that the most part of the convergence time happens before 600 seconds, and a majority before 200 seconds, versus 5500 and 2000 seconds respectively without ionospheric corrections. This means one order of magnitude in the reduction of the convergence time. The final accuracy is typically below 5 cm with WARTK and below 15 cm for the most distant roving user AUT1 (and below 10 cm for PVOG) without ionospheric corrections.

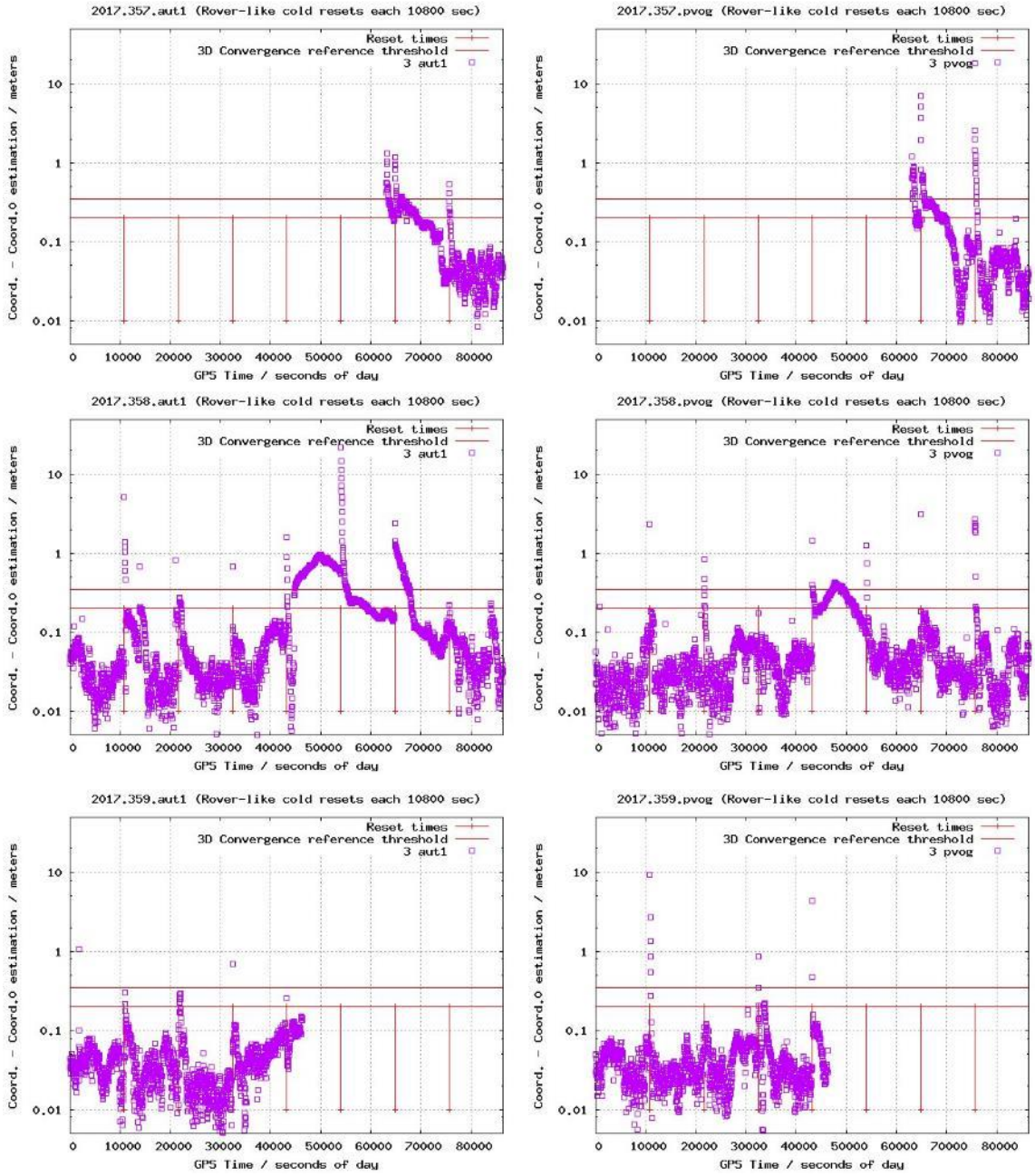

Figure 2.30 3D RT positioning error of the WARTK (i.e. fixing wide- and narrow-lane ambiguities) roving GPS receivers AUT1 (first column) and PVOG (second column) during the overall Christmas days experiment (days 23, 24 and 25 December 2017, in first, second and third row respectively).

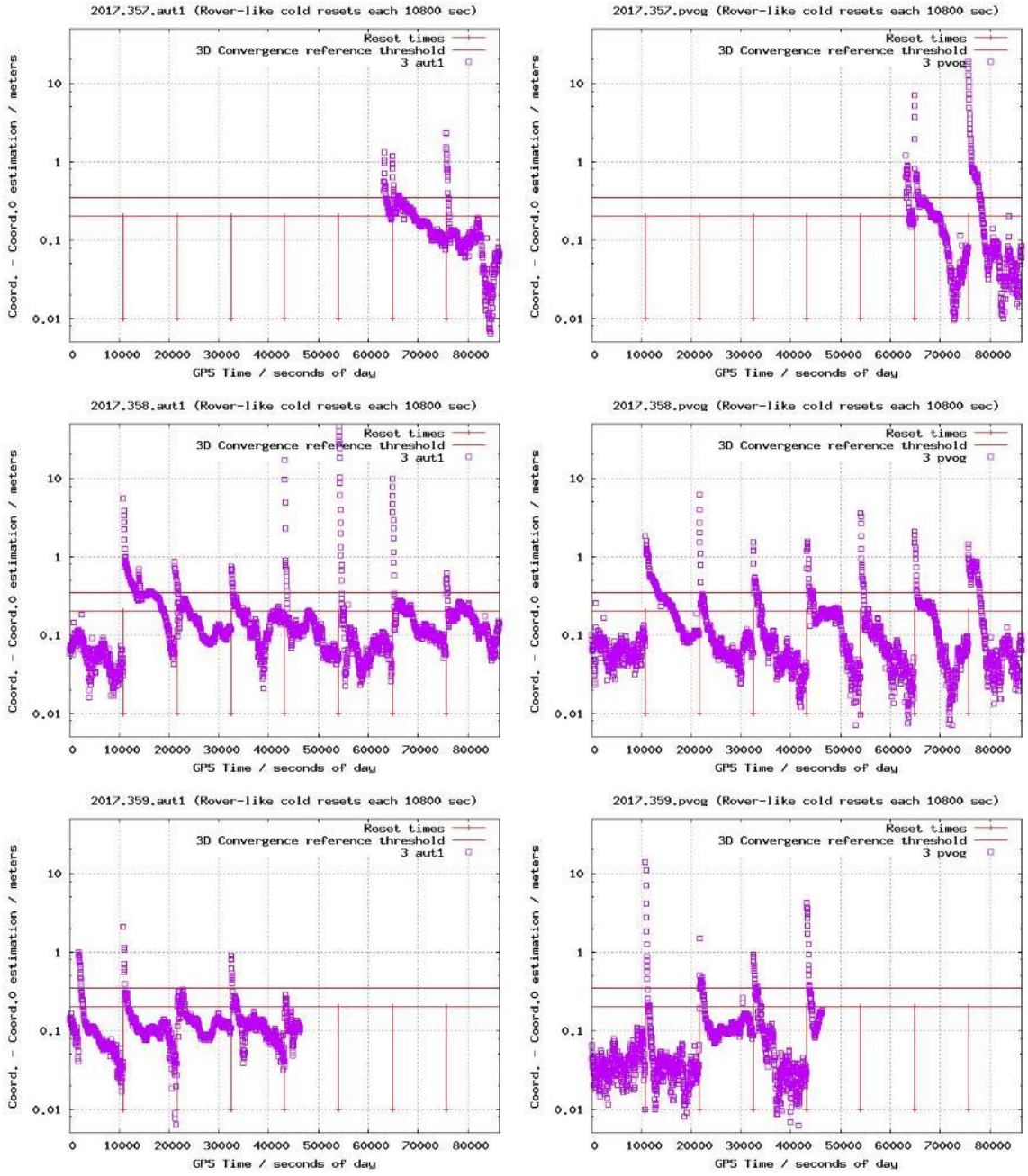

Figure 2.31 3D RT carrier-phase based differential positioning error (i.e. no fixing carrier phase ambiguities) for the roving GPS receivers AUT1 (first column) and PVOG (second column) during the overall Christmas days experiment (days 23, 24 and 25 December 2017, in first, second and third row respectively).

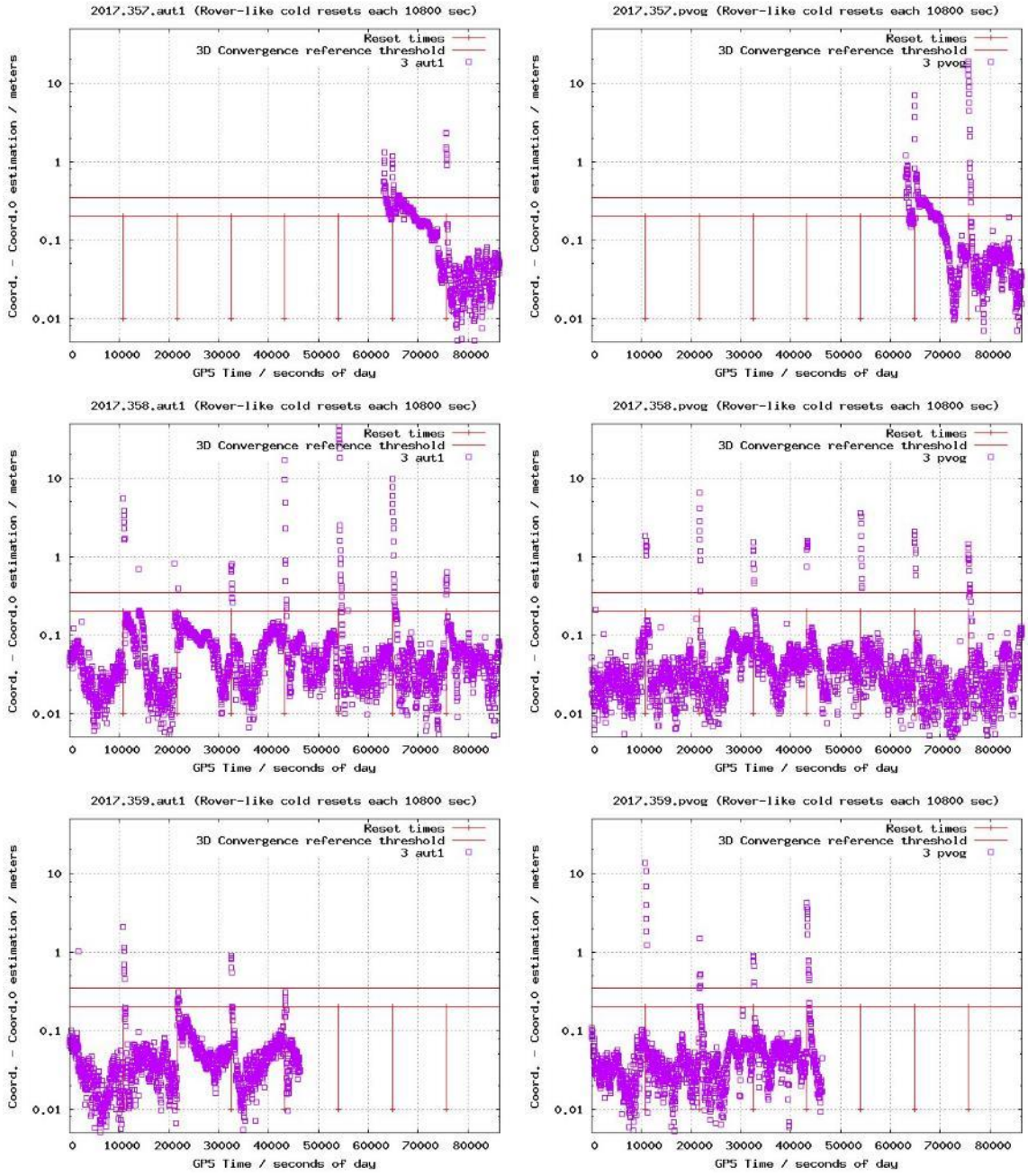

Figure 2.32 3D RT carrier-phase based differential positioning error (i.e. fixing wide- and narrow-lane ambiguities, with higher requirements of bias error estimates to fix both double-differences) for the roving GPS receivers AUT1 (first column) and PVOG (second column) during the overall Christmas days experiment (days 23, 24 and 25 December 2017, in first, second and third row respectively).

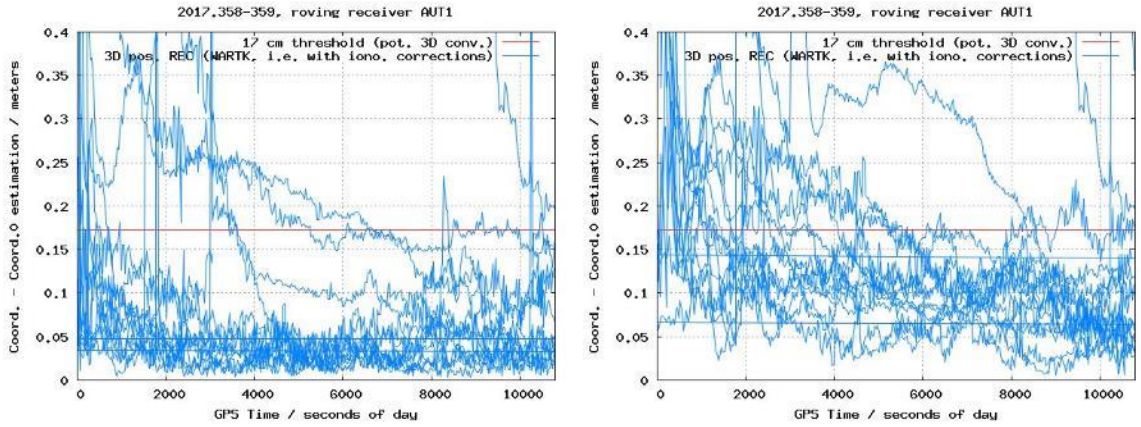

Figure 2.33 3D RT positioning error for roving receiver AUT1 with WARTK (i.e. constraining the wide- and narrow-lane ambiguities with the ionospheric corrections, left) and without ionospheric corrections, i.e. without constraining the ambiguities (right), during the overall Christmas days experiment (days 23, 24 and 25 December 2017).

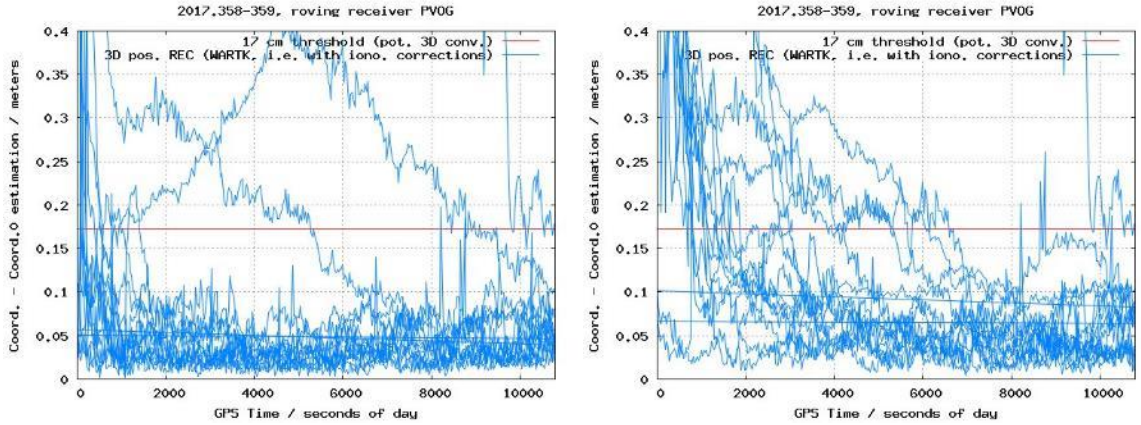

Figure 2.34 3D RT positioning error for roving receiver PVOG with WARTK (i.e. constraining the wide- and narrow-lane ambiguities with the ionospheric corrections, left) and without ionospheric corrections, i.e. without constraining the ambiguities (right), during the overall Christmas days experiment (days 23, 24 and 25 December 2017).

2.1.9 Trying to clarify the reason of the temporarily WARTK worsening starting 43200 sec of day 358, 2017: Single Receiver MSTID Index and MSTID footprints

In order to try to identify and understand the potential reasons of the RT positioning performance decrease for roving users during the central day (since 43000 to about 70000 seconds for AUT1, and up to 54000 for PVOG, day 358, 2017), coinciding with the sudden increase of CPF ionospheric planar fit residuals per satellite, as shown above, we have computed the Single Receiver MSTID activity index, SRMTID. This has been done after performing a first analysis of the post-fit residuals of the five measurements without providing new insights (see Appendix). Indeed, the SRMTID index will help us to confirm the suspicious of significant activity coinciding with the period of WARTK poorest performance, based in some of our previous works (such as Hernández-Pajares et al. 2012). Indeed, it can be seen in Figure 2.35 that this is the case, coinciding with the climatic occurrence of MSTID at mid

latitudes studied in the above mentioned reference (happening mainly on fall and winter daylight time, equatorward, and spring and summer night time, westward). A zoom showing up the effect of the MSTIDs around 42000-44000 seconds can be seen in Figure 2.36 with oscillations of about 10 cm in different phase for the four carrier phase measurements involved in the double-differenced, i.e. not cancelling, on the contrary when the double-differences of the ionospheric delays are considered. This non-linear of up to few decimeters is much larger than the maximum allowable error of the ionospheric correction (about 1.3 cm when the ambiguity parity check is used), strongly suggesting the possibility of bad ambiguity fixing behind such worse WARTK behaviour during day time coinciding with the MSTID activity. In order to mitigate this effect different techniques can be applied in future updates of the CPF, depending on the density of the network, being Hadasz et al. 2017 or Hernández-Pajares et al. 2012 ([13], [8]) more suitable for our sparse network, compared with Yang et al. 2017 for dense networks. In the mean time we have applied a more demanding condition to fix ambiguities, in terms of a reduction of the maximum allowable estimated error for Bi, ddBi, MW and ddMW, and it works quite well, eliminating the bad fixing during the center of day 358.

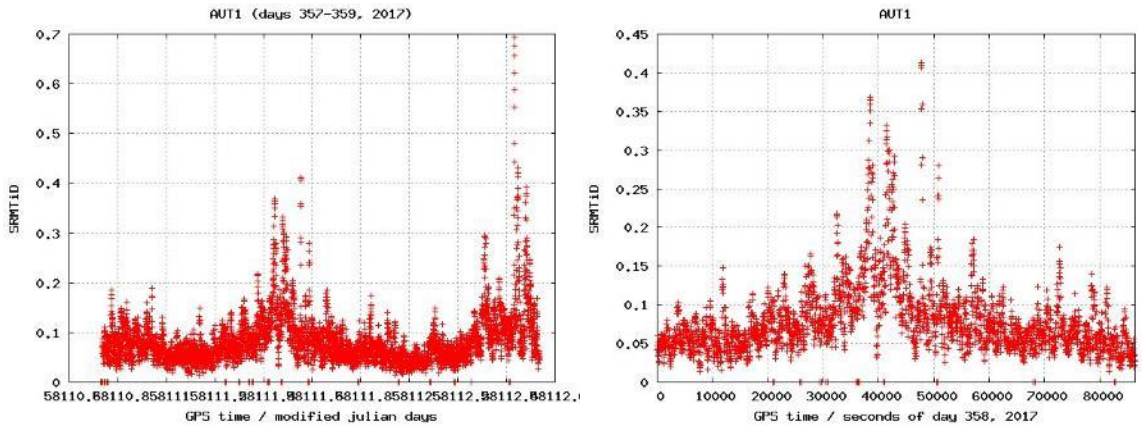

Figure 2.35 Single Receiver MSTID Index for roving receiver AUT1, versus time in Julian days for the overall RT experiment (left-hand plot) and versus seconds of day 358, 2017 (central day of the RT experiment).

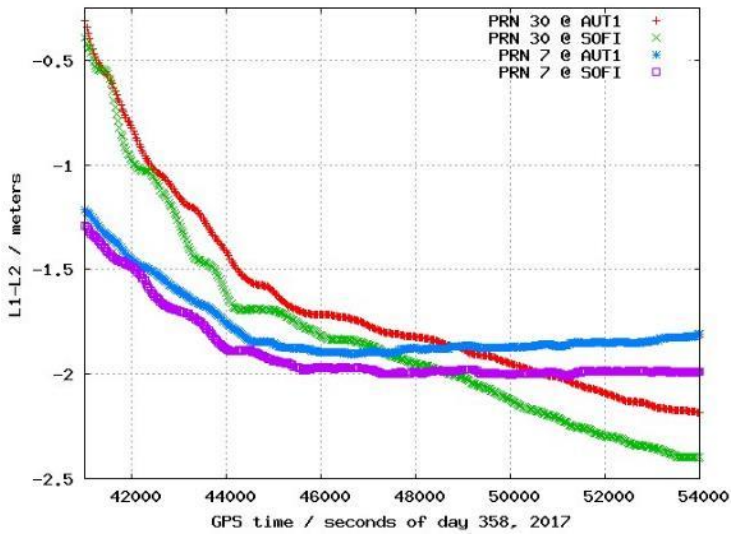

Figure 2.36 Zoom of Li=L1-L2 carrier phase measurements in length units for satellite PRN07 and PRN30 taken from receivers AUT1 and SOFI during 24 December, 2017.

2.1.10 Reprocessing by mitigating the MSTID effect on the temporarily WARTK worsening starting 43200 sec of day 358, 2017, by means of a more exigent threshold for the estimated standard deviation of the computed ionospheric carrier phase ambiguity corresponding to the WARTK user.

In order to improve the user RT positioning performance during the noon of the second day, when MSTID activity is important, we have implemented a simple update in the real-time filter: to be much more exigent to fix the ambiguities. Indeed, the maximum allowed standard deviation to fix has been change to, simultaneously, 15 cm, 25 cm and 2.7 cm for undifferenced widelane estimated ambiguity, the corresponding double differenced one, and the undifferenced ionospheric-combination ambiguity respectively (instead of 1m, 2m and 20cm respectively, as before). The improvement is clear: the long lasting time with high residuals of STEC planar fit per satellite during noon time go down to normal values (see Figure 2.37 and Figure 2.38) and the positioning error go down to normal values after convergence (typically below 10 cm, see Figure 2.39 and Figure 2.40). The "price to pay" is a not so strong reduction of the convergence time: the most part of ambiguities for WARTK user further from the permanent receivers, AUT1, need up to ~4000 seconds to convergence with no ionospheric corrections / ambiguity fixing; up to ~200 seconds with the previous most relaxed ambiguity fixing threshold; and up to ~500 seconds with the new parameters fixing the problems during the noon (see Figure 2.41). A similar relative situation is shown in the same figure for closer receiver PVOG, but with convergence values smaller as expected (especially in the case of non-use of ionospheric corrections).

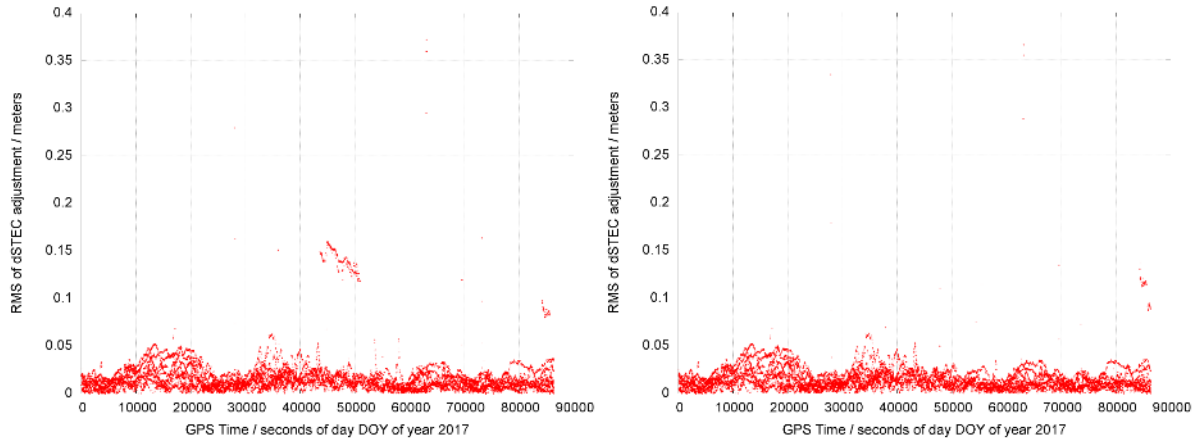

Figure 2.37 The RMS of the residuals of the VTEC fitting per satellite (vertical axis in meters of LI=L1-L2) vs time (horizontal axis in seconds of the day) is represented, during the second day of the RT experiment (day 24 December 2017), with the initial set of thresholds for user carrier phase ambiguity fixing (left) and with a more exigent one (right).

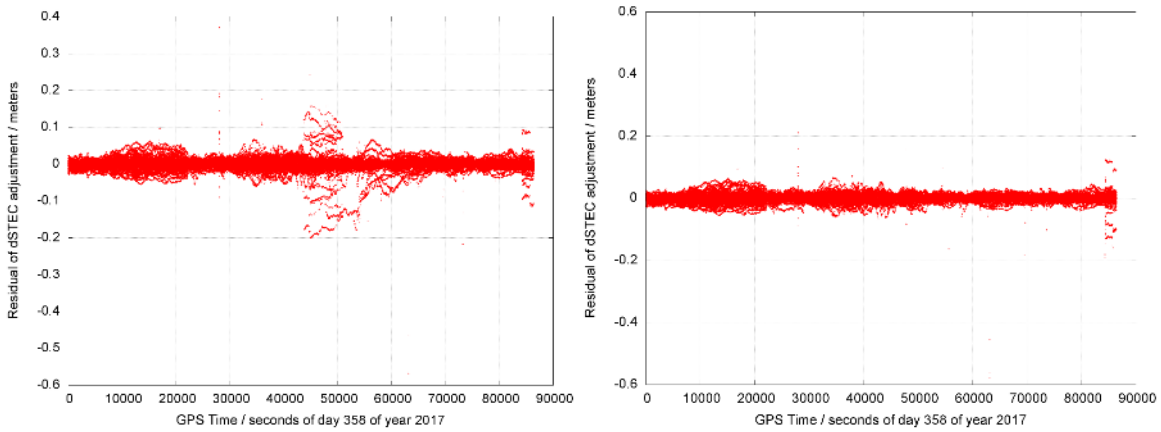

Figure 2.38 Residuals of the VTEC fitting per satellite (vertical axis in meters of LI=L1-L2) vs time (horizontal axis in seconds of the day) is represented, during the second day of the RT experiment (day 24 December 2017), with the initial set of thresholds for user carrier phase ambiguity fixing (left) and with a more exigent one (right).

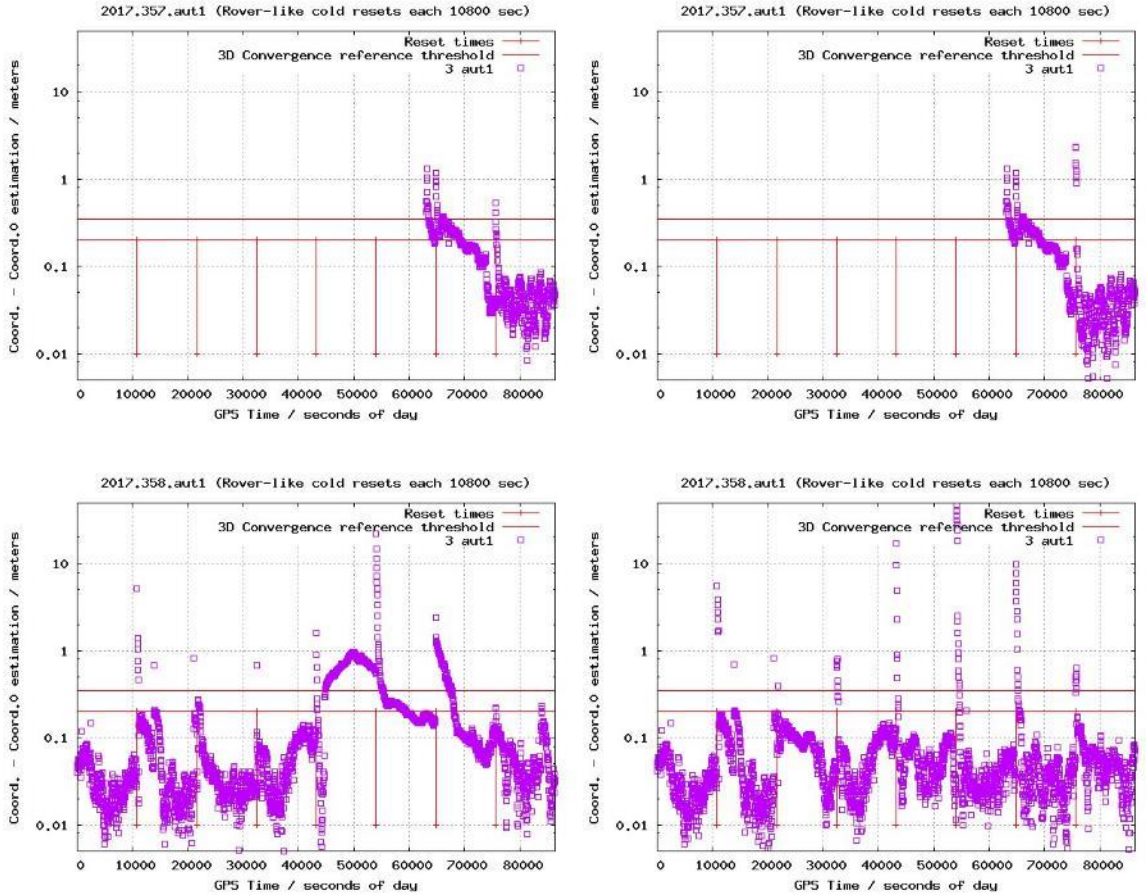

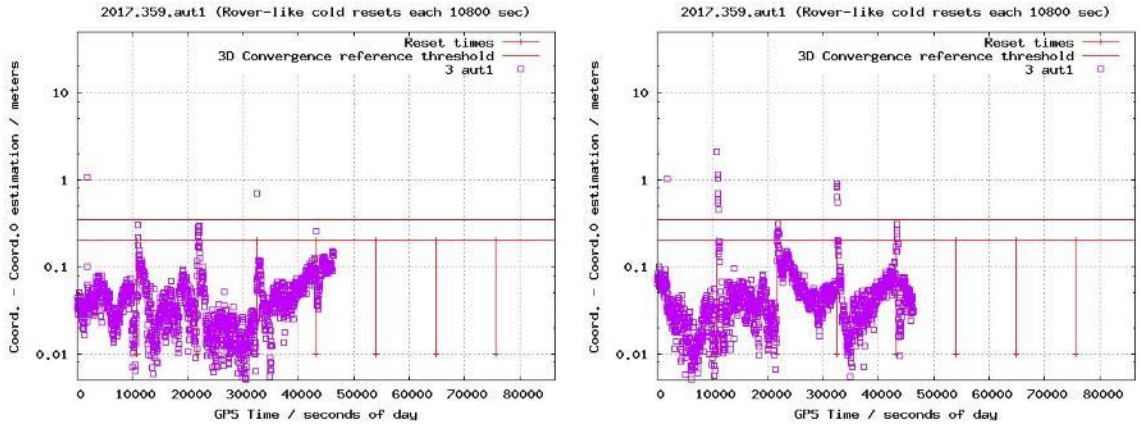

Figure 2.39 3D RT positioning error of the WARTK (i.e. fixing wide- and narrow-lane ambiguities) roving GPS receivers for AUT1 with previous threshold for ambiguity fixing (first column) and with the most exigent one (second column) during the overall Christmas days experiment (days 23, 24 and 25 December 2017, in first, second and third row respectively).

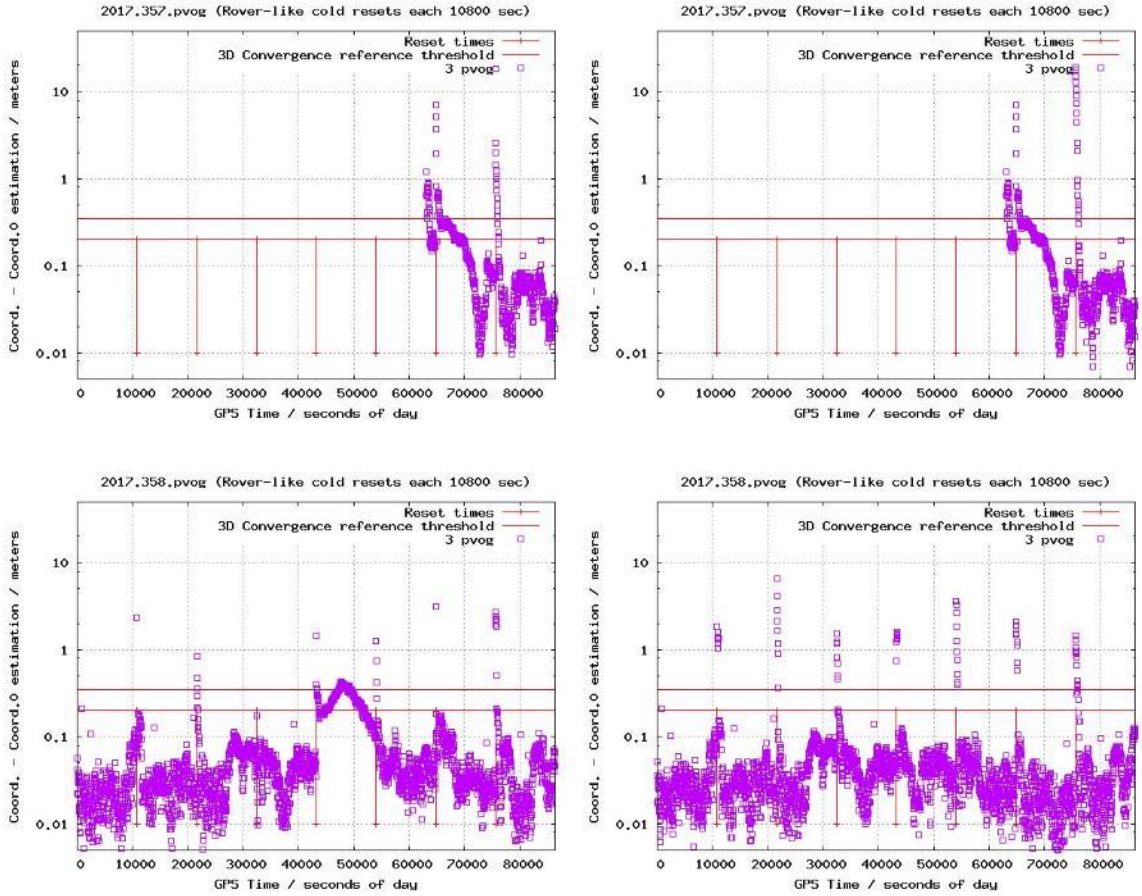

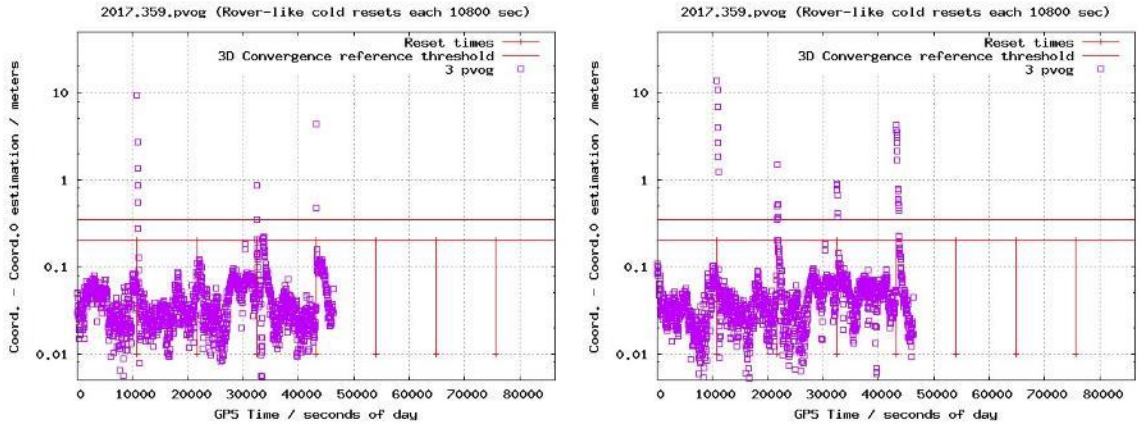

Figure 2.40 3D RT positioning error of the WARTK (i.e. fixing wide- and narrow-lane ambiguities) roving GPS receivers for AUT1 with previous threshold for ambiguity fixing (first column) and with the most exigent one (second column) during the overall Christmas days experiment (days 23, 24 and 25 December 2017, in first, second and third row respectively).

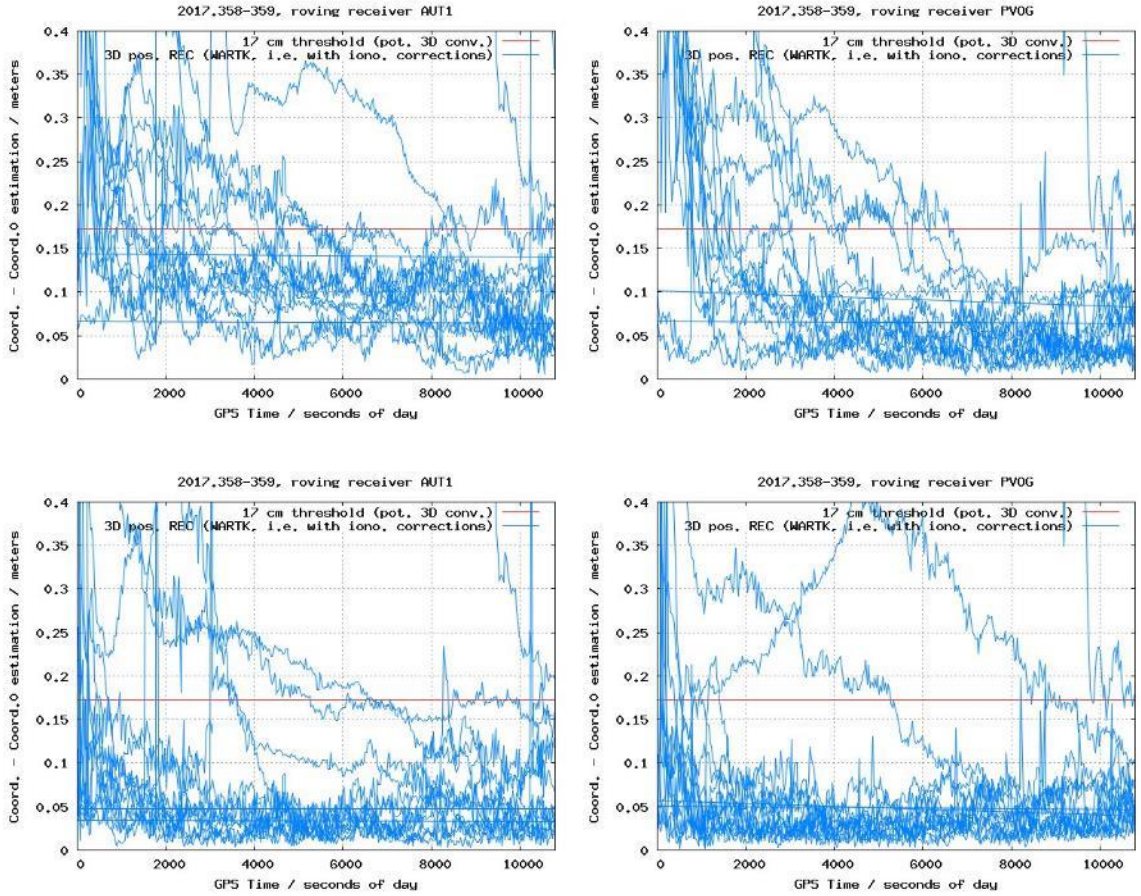

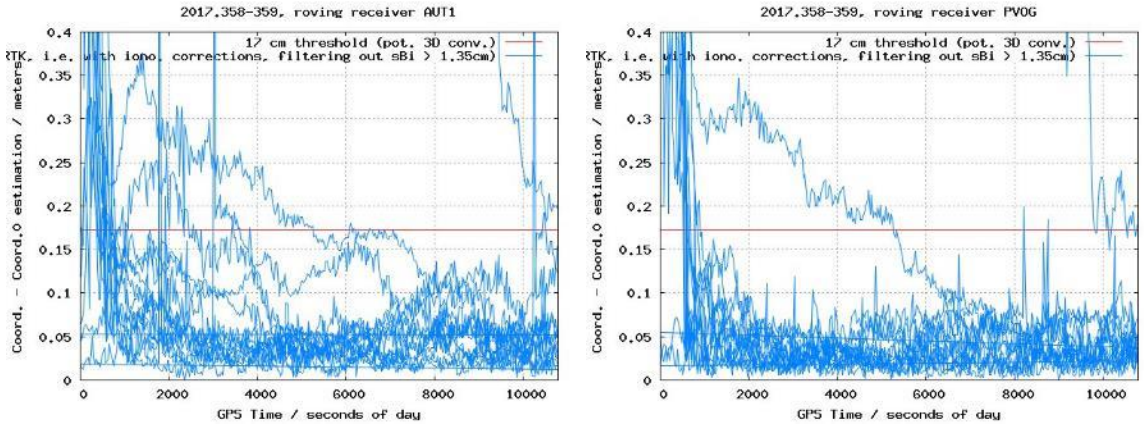

Figure 2.41 3D RT positioning error for roving receiver AUT1 (first column) and PVOG (second column), without ionospheric corrections i.e. without constraining the ambiguities (first row), with WARTK (i.e. constraining the wide- and narrow-lane ambiguities with the ionospheric corrections) in second row (former threshold for widelane and narrowlane ambiguity fixing) and in third row (for new more exigent ambiguity fixing thresholds), during the overall Christmas days experiment (days 23, 24 and 25 December 2017).

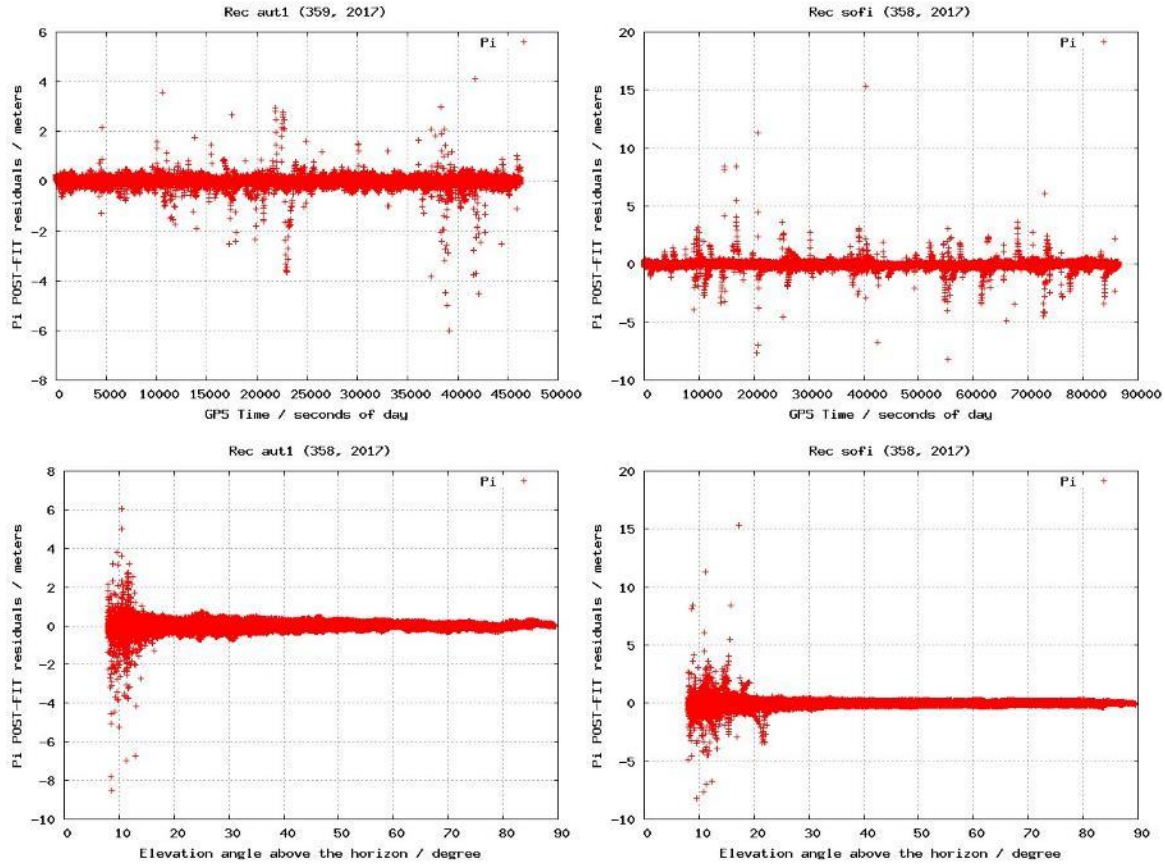

Figure 2.42 Post-fit residual for the ionospheric combination of the pseudoranges corresponding to the roving receiver AUT1 (first column) and the reference receiver SOFI (second column), versus time (first row) and versus elevation (second row), during day 25 December 2017.

3 AUDITOR corrections dissemination

3.1 VTEC dissemination via RTCM 1264

3.1.1 Process overview

As defined in D6.1 [1], the implemented VTEC dissemination data flow is as shown in Figure 3.1.

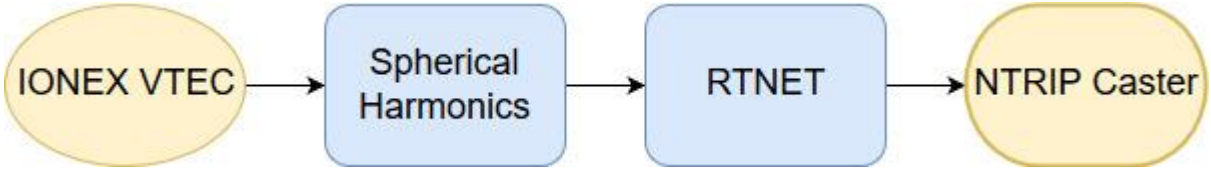

Figure 3.1 VTEC dissemination flow chart

The process uses as input a VTEC map in IONEX format [reference]. This map is then transformed in spherical harmonics to be compatible with the RTCM standard 1264 message. Afterwards, these data are transformed to a RTNET message. This is done because in this way we could use the BNC (BKG NTRIP Client) software to encode and send RTCM 1264 messages to a NTRIP caster. Doing so we could use this well-known, extensively tested and used software to manage the connection with the NTRIP caster. The VTEC data is then sent continuously at a 10 seconds period rate, to lower the wait time for a cold-start client.

3.1.2 Implementation description

All the process is done by a single python script (*ionex_2_bnc_rtnet.py*). Still, a set of bash scripts have been created to manage some system-related functions, configure the entire process and perform some minor system-related functions.

In this sense, the main bash script (*ionex_2_rtcm.sh*) consists of three sub-processes:

- Link creation: a first process is launched to continuously create a soft-link to the latest available IONEX file.
- IONEX to RTNET: a second process configures and launches the python script responsible of performing the tasks described earlier in this section: checking the IONEX file for updates, translating the VTEC data to RTNET and sending it in each configured time interval to the BNC software.
- BNC NTRIP server: a third process launches a BNC instance, which receives through an IP port the RTNET data and relies it to the NTRIP caster. In case the BNC process dies, it is automatically restarted again.

This main script also stores the PID (Process IDentifiers) in a file to make it easier to stop the entire chain and sends the output of all the processes in a single log file.

The following configuration parameters have been defined (inside the *config.sh* file, see Figure 3.2):

- `ionex_file_path`: Path to the directory where the different IONEX files are generated.
- `ionex_iaac_name`: Name of the IAAC responsible to generate the ionex file. Used to find the correct ionex file to distribute.

- `spherical_harmonics_degree` and `spherical_harmonics_order`: Maximum degree and order used for the spherical harmonics expansion. Must be equal or less than 15 to be compatible with RTCM 1264.
- `rtcm_message_period`: Time interval to send again the latest VTEC data.
- `bnc_ip`: IP used for the local bnc process acting as BNC server to receive the VTEC data to send to the caster.
- `bnc_port`: Port used for the local bnc process acting as BNC server. If set to 0, a random free port higher than 1024 (unprivileged ports) is used.
- `bnc_mountpoint`: Mountpoint name to transmit to the caster.
- `ntrip_server_*`: Various information sent to the caster about the NTRIP server. Some casters, like SNIP, do not implement sharing information about the server this way and then it will be simply ignored.
- `caster_ip`: IP of the NTRIP caster where to send the VTEC data.
- `caster_port`: Port of the NTRIP caster.
- `caster_password`: Password used to authenticate to the NTRIP caster.

```
ionex_file_path=/var/www/tomion/real-time/quick/last_results/
ionex_iaac_name="urtg"

spherical_harmonics_degree=15
spherical_harmonics_order=15

rtcm_message_period=10      #In seconds

bnc_ip='127.0.0.1'
bnc_port=0                  #0 to get a dynamically generated port
bnc_mountpoint="URTG"

ntrip_server_latitude=41.39
ntrip_server_longitude=2.15
ntrip_server_city="Barcelona"
ntrip_server_country="ESP"

caster_ip='127.0.0.1'
caster_port=2101
caster_password="<DELETED>"
```

Figure 3.2: Configuration used in the implementation of the VTEC dissemination

3.1.2.1 IONEX to RTNET processing

This is the process that performs all the computations. An overall flow chart can be seen at Figure 3.3. The process opens a TCP/IP socket and waits until the BNC client connects. Afterwards it enters an infinite loop, updating and sending the data.

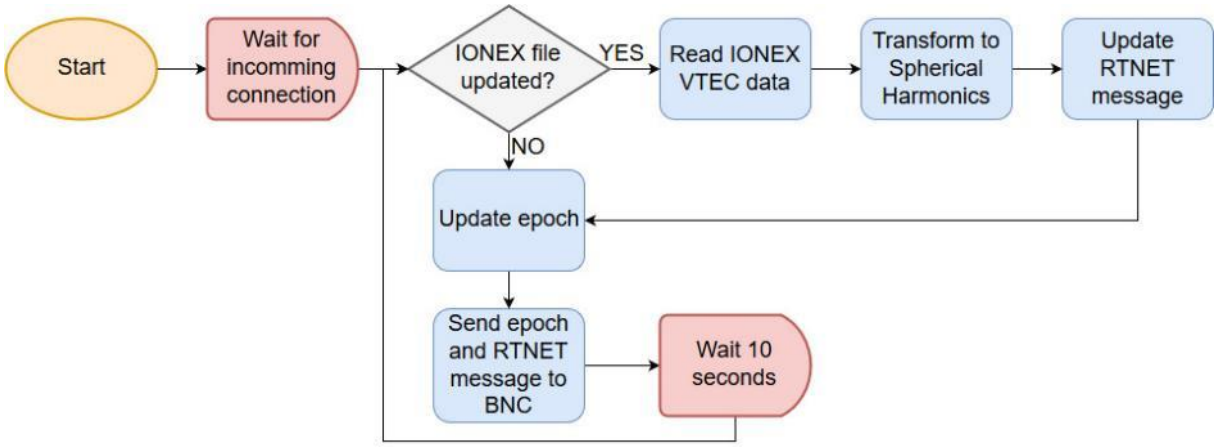

Figure 3.3 IONEX to BNC RTNET flow chart

The process uses as input a VTEC map in IONEX format. The MD5 hash is continuously computed over this file and when its value changes, the file is parsed again and the VTEC data of the last map available is used as the current map to be distributed to the clients. In the current tested implementation this map is the URTG (UPC Real-Time Global) GIM (Global Ionospheric Map). This GIM is computed by UPC and made publicly available free of charge through FTP on UPC servers and NASA's CDDIS, among others. Due to the computation time of the GIM, a latency of about 9 minutes exists between the station observables used as input for the GIM and the VTEC map. The effect of this delay on the quality of the VTEC data is considered negligible.

In case the IONEX file has been updated, two transformations are done. The first computational step of the implemented solution consists in transforming the VTEC map in an expansion of harmonics to be compatible with the RTCM standard 1264 message. The standard limits the maximum order and degree of the spherical harmonics to 15 both. This is currently the main source of error producing a smoothing of the VTEC map. The relative error of this step has been assessed to be around 6 % (see Roma-Dollase et al., 2017 [11], and next Section 3.2).

The second step consists in transforming the spherical harmonics to a RTNET message. In this step, an additional rounding to the nearest even value is performed following the IEEE floating point standard. This rounding is needed since the RTCM 1264 standard has a resolution for the coefficients of 0.005 TECU. The error introduced by this step is considered negligible since the dominant lower order and degree coefficients have much larger values and hence it only affects the less important coefficients with small values.

Finally, every 10 seconds, the epoch information of the RTNET message is updated and the latest RTNET message is sent to the BNC socket.

3.1.3 Execution

The entire process has been running in production at a server in UPC. During the tests of this implementation some issues have been raised and solved, all of them related to the asynchrony

between the GIM generation and the dissemination process. For example, when the day changes the file of the previous date is moved to another location and some time passes before the new file is available. In this case, the hash computation of the file failed since the file did not exist and the updating of the VTEC data was halted until the new file appeared. In another case, it was detected that sometimes the IONEX file parsing failed. This was since the IONEX file was read while the GIM generation process was still writing it. This was also solved, and now in case the IONEX file parsing fails the previous VTEC data is also used. It is to notice that in both cases only the updating of the VTEC data sent to BNC is halted, the sending of the data itself still is done at the frequency defined.

The full chain has been validated using SNIP software (Figure 3.4) as NTRIP caster and another BNC instance as NTRIP client. This has been running, once the previous issues were solved, for more than 10 days uninterruptedly without any issue. It was also tested that even in the case that the NTRIP caster is not reachable, the dissemination process will automatically reconnect to the caster once it is working again.

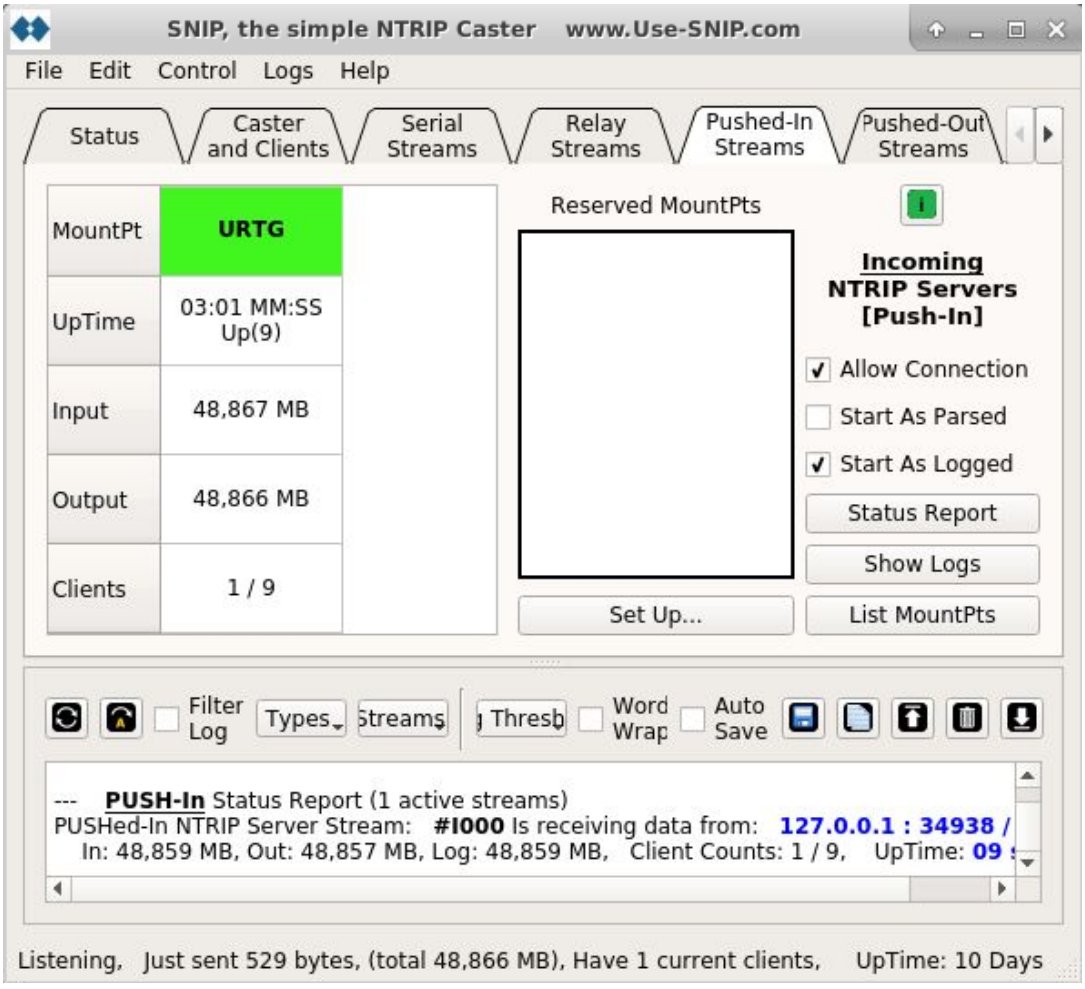

Figure 3.4 SNIP Caster used for testing the VTEC dissemination distributing URTG GIMs uninterruptedly for more than 10 days.

3.2 Study on RTCM 1264 messages (public)

At the moment, RTCM only defines one way to provide VTEC information to users: as a spherical harmonic series of a given order and degree (message type 1264). To our knowledge, the maximum

order and degree allowed by the standard is 16. The possibility to consider an RTCM message type with ionospheric data representing a grid has been under discussion by the RTCM working group, though seems not envisaged for the near future.

In this context, a study on the apparent limitation of these messages has been carried out by analyzing the loss of precision for the end user when using spherical harmonics instead of the IONEX content directly (Hernández-Pajares et al. 2017b [10]).

For this purpose, UQRG GIMs for one specific day have been encapsulated in spherical harmonics considering different degree/order. The results in Figure 3.5, Figure 3.6, Figure 3.7 and Figure 3.8 show the original VTEC GIM and the reconstructed VTEC GIMs for several spherical harmonics configurations.

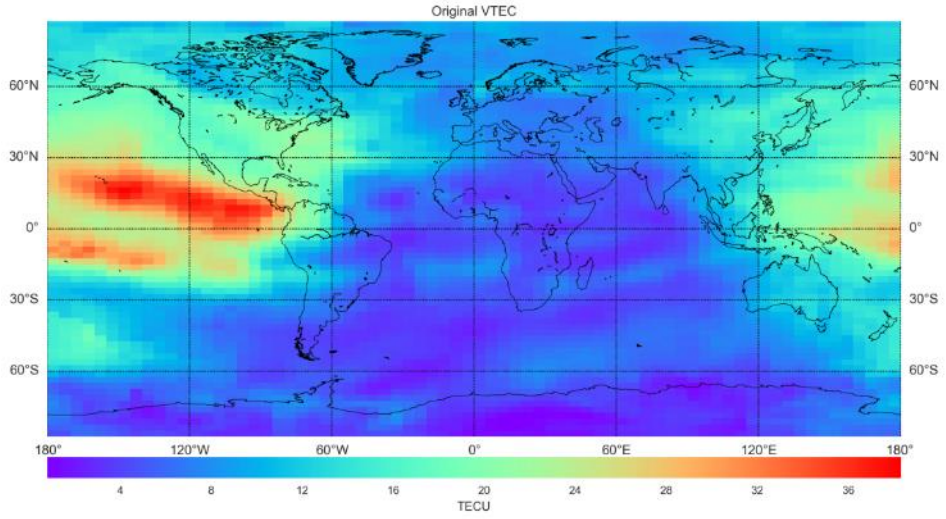

Figure 3.5 Original UQRG 15-minute VTEC GIM (UQRG1480.17i, 00UT)

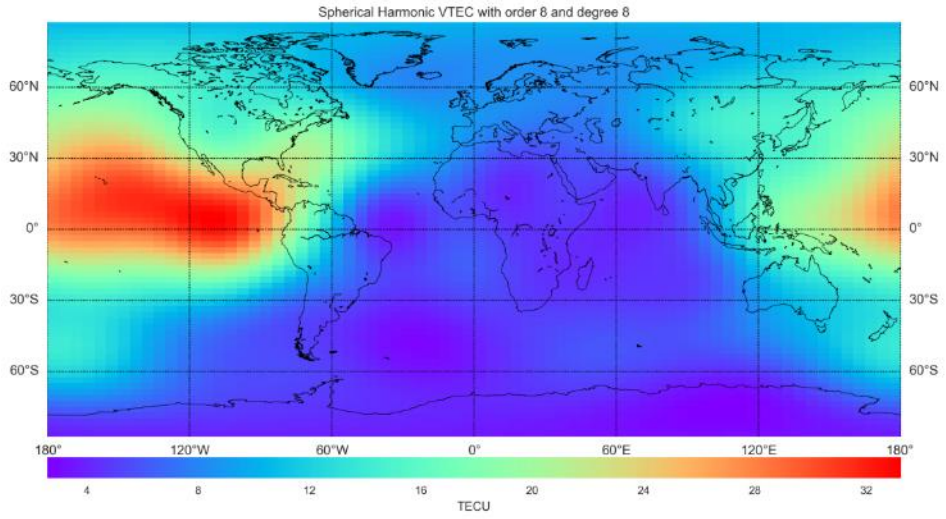

Figure 3.6 Reconstructed UQRG GIM considering SH of degree 8 and order 8, of day of year 148, 2017. Accounting for 13% RMS relative error.

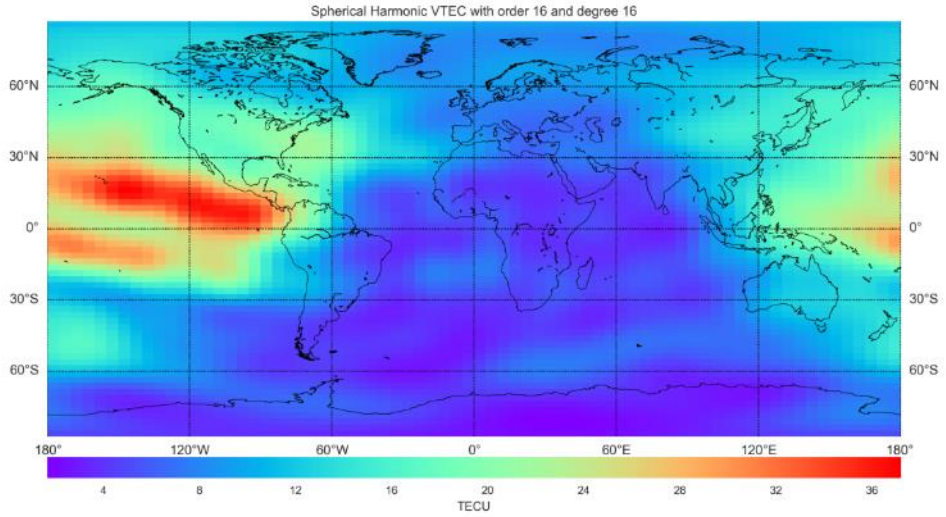

Figure 3.7 Reconstructed UQRG GIM considering SH of degree 16 and order 16, of day of year 148, 2017. Accounting for 5.8% RMS relative error.

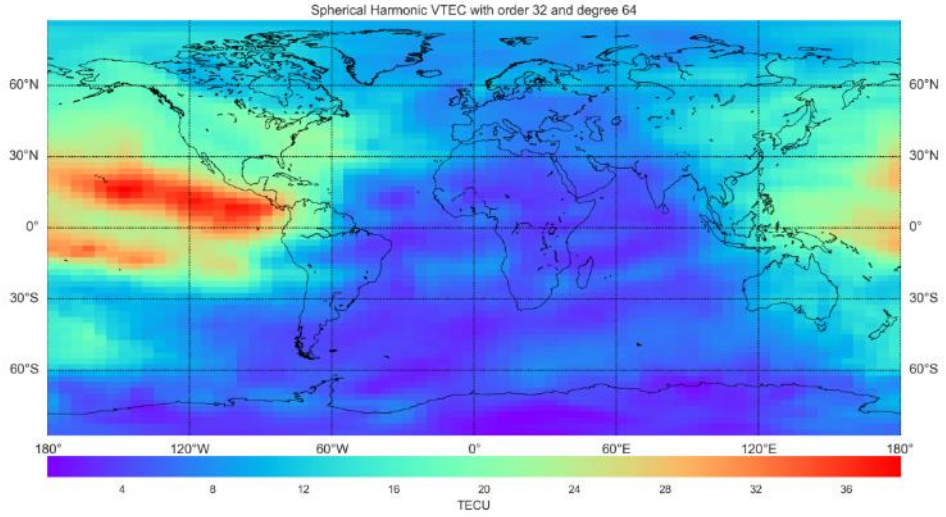

Figure 3.8 Reconstructed UQRG GIM considering SH of degree 64 and order 32, of day of year 148, 2017. Accounting for 1.8% RMS relative error.

3.2.1 Distribution of relative errors

More in detail, the following table provides the results for the multiple SH configurations (including the ones in the above Figures).

Table 3-1 RMS relative error in function of the SH degree/order for UQRG VTEC in day of year 148, 2017

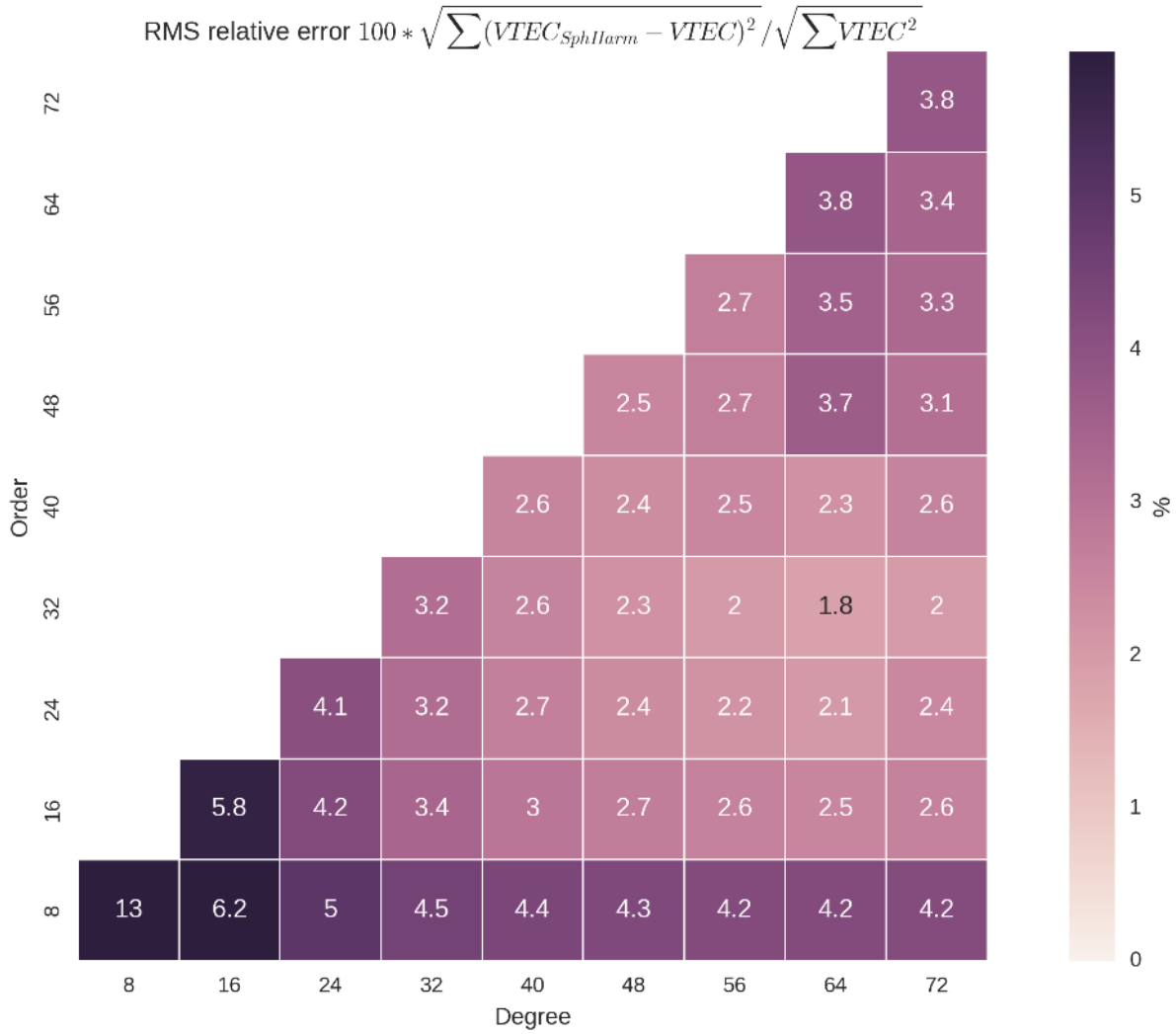

3.3 DSM corrections / User observations dissemination via netcat

The possibility to disseminate DSM corrections has been finally tested using netcat as file server. Note that this approach is also valid for the dissemination of other types of information, such as the user observations to the CPF and backwards, which will be implemented in AUDITOR.

For this purpose, we have considered the following Linux aliases to distinguish from other equivalent processes that could run in both the CPF server providing the corrections and another server emulating the user side.

alias AUDITORnc nc

alias AUDITORtail tail

In addition, we have defined a dedicated port for the dissemination of the corrections via netcat in both sides of the communication channel:

set AUDITORncport = 22216

On the sending end, located at chapman.upc.es server, it was required to run the following command lines:

cd ~/AUDITOR_DSM_netcat

alias AUDITORnc nc

alias AUDITORtail tail

AUDITORtail -f ~ionex4/art/AUDITOR-RT/messages1.output | grep ^DSM | AUDITORnc newg1.upc.es 22116 &

Note that the netcat execution at both sides is done as background processes so this allows to generate a permanent link between CPF and user sides.

On the destination end, which was tested at newg1.upc.es server, the following command lines were executed to validate the correct reception:

cd /d2/home/ionex4/AUDITOR_DSM_netcat

alias AUDITORnc nc

AUDITORnc -dlk 22116 > & DSM_incoming &

On the receiving end side, we are also listening on port 22116.

This concept was tested for the real-time distribution of DSM corrections in real-time, as provided by the CPF. The receiving end could receive the corrections without disruptions for 5 recent consecutive days. This approach will be implemented to establish the communication channel between the prototype AUDITOR receiver and the CPF.

4 AUDITOR GNSS-SDR with RTKLIB integration validation

GNSS-SDR now integrates the core RTKLIB libraries for Single Point Positioning and Precise Point Positioning. The user can configure the processing block in charge of PVT computation with a number of options, detailed hereafter:

Table 4-1 Configuration options for PVT computation in GNSS-SDR

Parameter	Description	Required
`implementation`	`RTKLIB_PVT`	Mandatory
`output_rate_ms`	Rate at which PVT solutions will be computed, in ms. It defaults to 500 ms.	Optional
`display_rate_ms`	Rate at which PVT solutions will be displayed in the terminal, in ms. It defaults to 500 ms.	Optional
`positioning_mode`	[`Single`, `PPP_Static`, `PPP_Kinematic`] Set positioning mode. `Single`: Single point positioning.`PPP_Static`: Precise Point Positioning with static mode. `PPP_Kinematic`: Precise Point Positioning for a moving receiver. It defaults to `Single`.	Optional
`num_bands`	[`1`: L1 Single frequency, `2`: L1 and L2 Dual-frequency, `3`: L1, L2 and L5 Triple-frequency] This option is automatically configured according to the Channels configuration. This option can be useful to force some configuration (*e.g.*, single-band solution in a dual frequency receiver).	Optional
`elevation_mask`	Set the elevation mask angle, in degrees. It defaults to $15º$	Optional
`dynamics_model`	[`0`: Off, `1`: On] Set the dynamics model of the receiver. If set to 1 and `PVT.positioning_mode=PPP_Kinematic`, the receiver position is predicted with the estimated velocity and acceleration. It defaults to 0 (no dynamics model).	Optional
`iono_model`	[`OFF`, `Broadcast`, `Iono-Free-LC`]. Set ionospheric correction options. `OFF`: Not apply ionospheric correction. `Broadcast`: Apply broadcast ionospheric model. `Iono-Free-LC`: Ionosphere-free linear combination with dual frequency (L1-L2 for GPS or L1-L5 for Galileo) measurements is used for ionospheric correction. It defaults to `OFF` (no ionospheric correction)	Optional

Parameter	Description	Required
`trop_model`	[`OFF`, `Saastamoinen`, `Estimate_ZTD`, `Estimate_ZTD_Grad`]. Set whether tropospheric parameters (zenith total delay at rover and base-station positions) are estimated or not. `OFF`: Not apply troposphere correction. `Saastamoinen`: Apply Saastamoinen model. `Estimate_ZTD`: Estimate ZTD (zenith total delay) parameters as EKF states. `Estimate_ZTD_Grad`: Estimate ZTD and horizontal gradient parameters as EKF states. If defaults to `OFF` (no troposphere correction).	Optional
`code_phase_error_ratio_l1`	Code/phase error ratio R_r for the L1 band. It defaults to 100.	Optional
`carrier_phase_error_factor_a`	Carier phase error factor $a_{2\sigma}$. It defaults to 0.003 m.	Optional
`carrier_phase_error_factor_b`	Carier phase error factor $b_{2\sigma}$. It defaults to 0.003 m.	Optional
`slip_threshold`	Set the cycle-slip threshold (m) of geometry-free LC carrier-phase difference between epochs. It defaults to 0.05.	Optional
`threshold_reject_GDOP`	Set the reject threshold of GDOP. If the GDOP is over the value, the observable is excluded for the estimation process as an outlier. It defaults to 30.0.	Optional
`threshold_reject_innovation`	Set the reject threshold of innovation (pre-fit residual) (m). If the innovation is over the value, the observable is excluded for the estimation process as an outlier. It defaults to 30.0 m.	Optional
`number_filter_iter`	Set the number of iteration in the measurement update of the estimation filter. If the baseline length is very short like 1 m, the iteration may be effective to handle the nonlinearity of measurement equation. It defaults to 1.	Optional
`sigma_bias`	Set the process noise standard deviation of carrier-phase bias σ_{bias}, in cycles/$\sqrt{s}$. It defaults to 0.0001 cycles/$\sqrt{s}$.	Optional
`sigma_trop`	Set the process noise standard deviation of zenith tropospheric delay σ_z, in m/$\sqrt{s}$. It defaults to 0.0001 m/$\sqrt{s}$.	Optional
`raim_fde`	[`0`, `1`]: Set whether RAIM (receiver autonomous integrity monitoring) FDE (fault detection and exclusion) feature is enabled or not. It defaults to 0 (RAIM not enabled)	Optional

Parameter	Description	Required
`reject_GPS_IIA`	[`0`, `1`]: Set whether the GPS Block IIA satellites are excluded or not. Those satellites often degrade the PPP solutions due to unpredicted behavior of yaw-attitude. It defaults to 0 (no rejection).	Optional
`phwindup`	[`0`, `1`]: Set whether the phase windup correction ϕ_{pw} for PPP modes is applied or not. It defaults to 0 (no phase windup correction).	Optional
`earth_tide`	[`0`, `1`]: Set whether earth tides correction is applied or not. If set to 1, the solid earth tides correction $\mathrm{d}_{r,disp}$ is applied to the PPP solution, following the description in IERS Technical Note No. 323, Chapter 7. It defaults to 0 (no Earth tide correction).	Optional
`rinex_version`	[`2`: version 2.11, `3`: version 3.02] Version of the generated RINEX files. It defaults to 3.	Optional
`nmea_dump_filename`	Name of the file containing the generated NMEA sentences in ASCII format. It defaults to `./nmea_pvt.nmea`.	Optional
`flag_nmea_tty_port`	[`true`, `false`]: If set to `true`, the NMEA sentences are also sent to a serial port device. It defaults to `false`.	Optional
`nmea_dump_devname`	If `flag_nmea_tty_port` is set to `true`, descriptor of the serial port device. It defaults to `/dev/tty1`.	Optional
`flag_rtcm_server`	[`true`, `false`]: If set to `true`, it runs up a TCP server that is serving RTCM messages to the connected clients during the execution of the software receiver. It defaults to `false`.	Optional
`rtcm_tcp_port`	If `flag_rtcm_server` is set to `true`, TCP port from which the RTCM messages will be served. It defaults to 2101.	Optional
`rtcm_station_id`	Station ID reported in the generated RTCM messages. It defaults to 1234.	Optional
`rtcm_MT1045_rate_ms`	Rate at which RTCM Message Type 1045 (Galileo Ephemeris data) will be generated, in ms. If set to `0`, mutes this message. It defaults to 5000 ms.	Optional
`rtcm_MT1019_rate_ms`	Rate at which RTCM Message Type 1019 (GPS Ephemeris data) will be generated, in ms. If set to `0`, mutes this message. It defaults to 5000 ms.	Optional
`rtcm_MSM_rate_ms`	Default rate at which RTCM Multiple Signal Messages will be generated. It defaults to 1000 ms.	Optional

Parameter	Description	Required
`rtcm_MT1077_rate_ms`	Rate at which RTCM Multiple Signal Messages GPS MSM7 (MT1077 - Full GPS observations) will be generated, in ms. If set to `0`, mutes this message. It defaults to `rtcm_MSM_rate_ms`.	Optional
`rtcm_MT1097_rate_ms`	Rate at which RTCM Multiple Signal Messages Galileo MSM7 (MT1097 - Full Galileo observations) will be generated, in ms. If set to `0`, mutes this message. It defaults to `rtcm_MSM_rate_ms`.	Optional
`flag_rtcm_tty_port`	[`true`, `false`]: If set to `true`, the generated RTCM messages are also sent to a serial port device. It defaults to `false`.	Optional
`rtcm_dump_devname`	If `flag_rtcm_tty_port` is set to `true`, descriptor of the serial port device. It defaults to `/dev/pts/1`.	Optional
`dump`	[`true`, `false`]: If set to `true`, it enables the PVT internal binary data file logging. It defaults to `false`.	Optional
`dump_filename`	If `dump` is set to `true`, name of the file in which internal data will be stored. It defaults to `./pvt.dat`.	Optional

The list of parameters in Table 4-1 includes those offered by RTKLIB's Graphical User Interface. Thus, users can make use of RTKLIB libraries for obtaining position fixes from GNSS-SDR without the need of installing both programs. The license in which the RTKLIB library is released (BSD 2-clause license) allows the integration of the core library files into the GNSS-SDR source tree. Some modifications were made for the sake of code correctness and the easier integration within GNSS-SDR source tree structure and coding style, but in essence it is the same source code that comes with RTKLIB, and it obtains the same numerical results from the same input data.

5 Conclusions

5.1 Conclusions on Front-end and Software-receiver validation (confidential)

Two versions of the FE were designed, implemented and validated. The second version FE v2.0 offered additional design benefits to overcome the interference issues of FE v1.0. The raw data stream provided by the FE required additional hardware/software support tools in order to properly capture heavy data streams (~200MBits) for enough time to perform the actual assessment (>1min). Several support tools were evaluated (ZedBoard, Logic Analyzer, custom USB capturer) and additional software was required in order to successfully perform the capture an ease the validation phase activities. Taking into account the maximum raw data stream for both channels, data reduction strategies needed to be apply in order to analyze multiple and long captures in a convenient way.

The analysis of multiple laboratory and indoor measurements lead to an optimal configuration of the PLL/OL settings and validation of the designed performance parameters of the RF L2/L5 additional downconversion.

Several issues were identified related to the microcontroller noise and spurious frequencies that required the full suspension of this chip. This lead to an evolution using the internal AGC (2-bit), that offers no information of the current applied gain.

Additional issues were identified with the stability of the main reference clock and its distribution to the PCB PLLs/OL. Other TCXO were evaluated using an external adapter that lead to successful outdoor L2 captures.

However, to perform the validations tests and solve the issues mentioned in previous sections, some modifications and additions to the FE have been implemented, suitable for a laboratory environment, which cannot be used in a field test due to the lack of robustness. A new board, FE v3.0 with the needed modifications should be manufactured and tested. This activity would take some additional months, that will block other tasks within the project timeframe. To perform the tests and finalize the project with successful results, a heavy search was performed to select an existing commercially available FE chip that can be used to integrate AUDITOR capabilities.

5.2 Conclusions on AUDITOR corrections validation (public)

A full and very realistic analysis of the performance of the AUDITOR WARTK CPF and user algorithms in actual real-time conditions during 23 to 25 December 2018, including two permanent receivers up to few hundred kilometres far treated as rover users with a cold starting up every 3 hours, is presented. The main conclusions are:

- The RT results obtained initially in actual real-time were quite good, especially in terms of a convergence time. This value is typically smaller than ~200 seconds, less than one order of magnitude smaller than the convergence time without ionospheric corrections (typically up to 4000 seconds). But there appear a significant positioning performance worsening at the noon of the second day.
- This user RT positioning worsening is coinciding with the existence of MSTIDs, the most frequent source of non-linearity affecting the precise ionospheric modelling in real-time.

- The problem in terms of positioning error is eliminated when the maximum formal ambiguity error threshold for user ambiguity fixing is strongly reduced, as a simple mitigation way of the MSTID effect in particular when the estimated error of the user' ionospheric-combination phase ambiguities are considered.

  A slight worsening found in term of user precise positioning convergence time with the new user ambiguity thresholds (about double, up to ~400 seconds typically of convergence time) might be mitigated in the future by adopting some of the RT MSTID modelling techniques conceived by the authors of this report (Hernández-Pajares et al. 2012 [8], Hadas et al. 2017 [13], Yang et al. 2017 [12]).

5.3 Conclusions on dissemination corrections and RTKLIB integration (public)

Firstly, we have implemented a VTEC dissemination data flow by means of the standard RTCM message type 1264, which is based on Spherical Harmonics of a given order and degree. In this context, a study was conducted on the loss of precision for the end user when using spherical harmonics instead of the IONEX content directly.

Secondly, the possibility to transmit STEC correction messages from the CPF (in DSM format) without any loss of precision has been tested using netcat (nc) computer networking utility as file server. This approach can also be suitable to transmit the observations from the user side to the CPF in case of considering an active system, as presented in Section 2.

GNSS-SDR has evolved to integrate the core RTKLIB libraries for Single Point Positioning and Precise Point Positioning. The possibility to add the newly developed RTKLIB routines for WARTK DSM messages applicability is feasible but a consolidation of the results is needed beforehand. These aspects, and potential back-up options, will be discussed in next DDM meeting.

6 References

[1] D6.1, AUDITOR Deliverable, 2017

[2] D3.1, AUDITOR Deliverable, 2017

[3] D3.2, AUDITOR Deliverable, 2018

[4] D3.3, AUDITOR Deliverable, 2018

[5] Blewitt, G. (1990). An automatic editing algorithm for GPS data. Geophysical research letters, 17(3), 199-202

[6] Hernández-Pajares, M., Roma-Dollase, D., Krankowski, A., García-Rigo, A., & Orús-Pérez, R. (2017). Methodology and consistency of slant and vertical assessments for ionospheric electron content models. Journal of Geodesy, 91(12), 1405-1414.

[7] Hernández-Pajares, M., Juan, J. M., Sanz, J., & Colombo, O. L. (2000). Application of ionospheric tomography to real-time GPS carrier-phase ambiguities resolution, at scales of 400–1000 km and with high geomagnetic activity. Geophysical Research Letters, 27(13), 2009-2012.

[8] Hernández-Pajares, M., Juan, J. M., Sanz, J., & Aragón-Àngel, A. (2012). Propagation of medium scale traveling ionospheric disturbances at different latitudes and solar cycle conditions. Radio Science, 47(6).

[9] Hernández-Pajares, M., Wielgosz, P., Paziewski, J., Krypiak-Gregorczyk, A., Krukowska, M., Stepniak, K., ... & Orus-Perez, R. (2017). Direct MSTID mitigation in precise GPS processing. Radio Science, 52(3), 321-337.

[10] Hernández-Pajares, M., Roma-Dollase, D., Garcia-Rigo, A. (2017b). Examples of IGS real-time Ionospheric information benefits: Space Weather monitoring, precise farming and RT-GIMs. Oral presentation at IGS Workshop 2017, Paris, France.

[11] Roma-Dollase, D., Hernández-Pajares, M., Krankowski, A., Kotulak, K., Ghoddousi-Fard, R., Yuan, Y., ... & Feltens, J. (2017). Consistency of seven different GNSS globl ionospheric mpping techniques during one solr cycle. Journal of Geodesy, 1-16.

[12] Yang, H., Monte-Moreno, E., & Hernández-Pajares, M. (2017). Multi-TID detection and characterization in a dense Global Navigation Satellite System receiver network. Journal of Geophysical Research: Space Physics, 122(9), 9554-9575.

[13] Hadas, T., Krypiak-Gregorczyk, A., Hernández-Pajares, M., Kaplon, J., Paziewski, J., Wielgosz, P., …, Orus-Perez, R. (2017). Impact and implementation of higher-order ionospheric effects on precise GNSS applications. Journal of Geophysical Research: Solid Earth, 122. https://doi.org/10.1002/2017JB014750

7 Appendix

7.1 Post-fit residuals for the roving user AUT1 and the reference receiver SOFI (public)

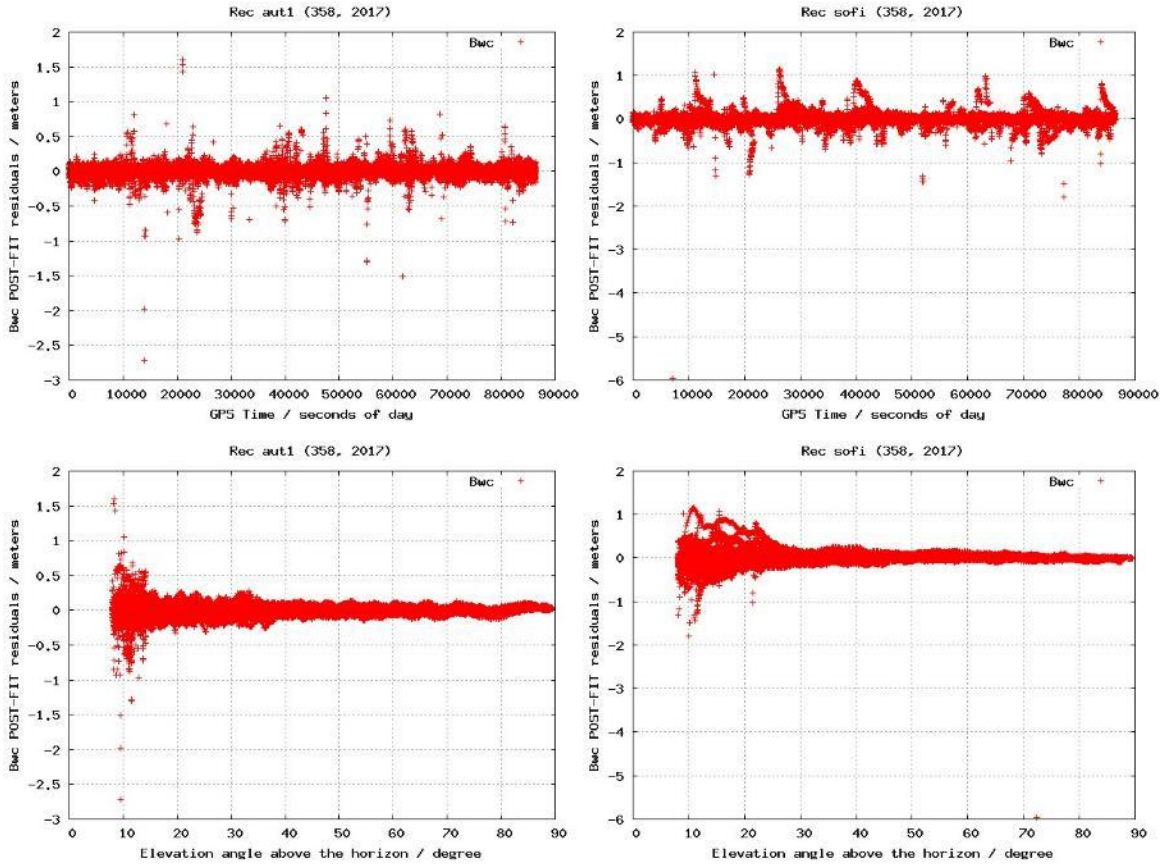

Figure 7.1 Post-fit residual for the Melbourne-Wübbena combination corresponding to the roving receiver AUT1 (first column) and the reference receiver SOFI (second column), versus time (first row) and versus elevation (second row), during day 25 December 2017.

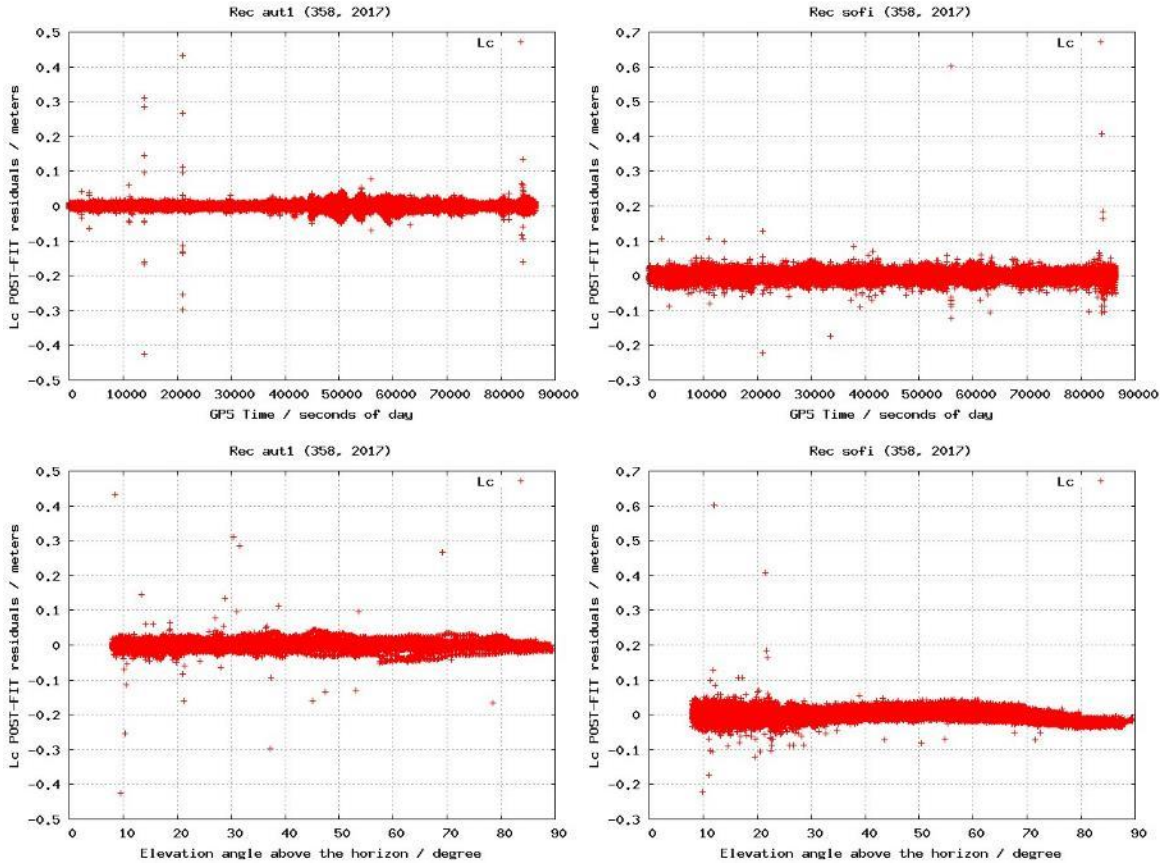

Figure 7.2 Post-fit residual for the ionospheric-free combination of the carrier phases corresponding to the roving receiver AUT1 (first column) and the reference receiver SOFI (second column), versus time (first row) and versus elevation (second row), during day 25 December 2017.

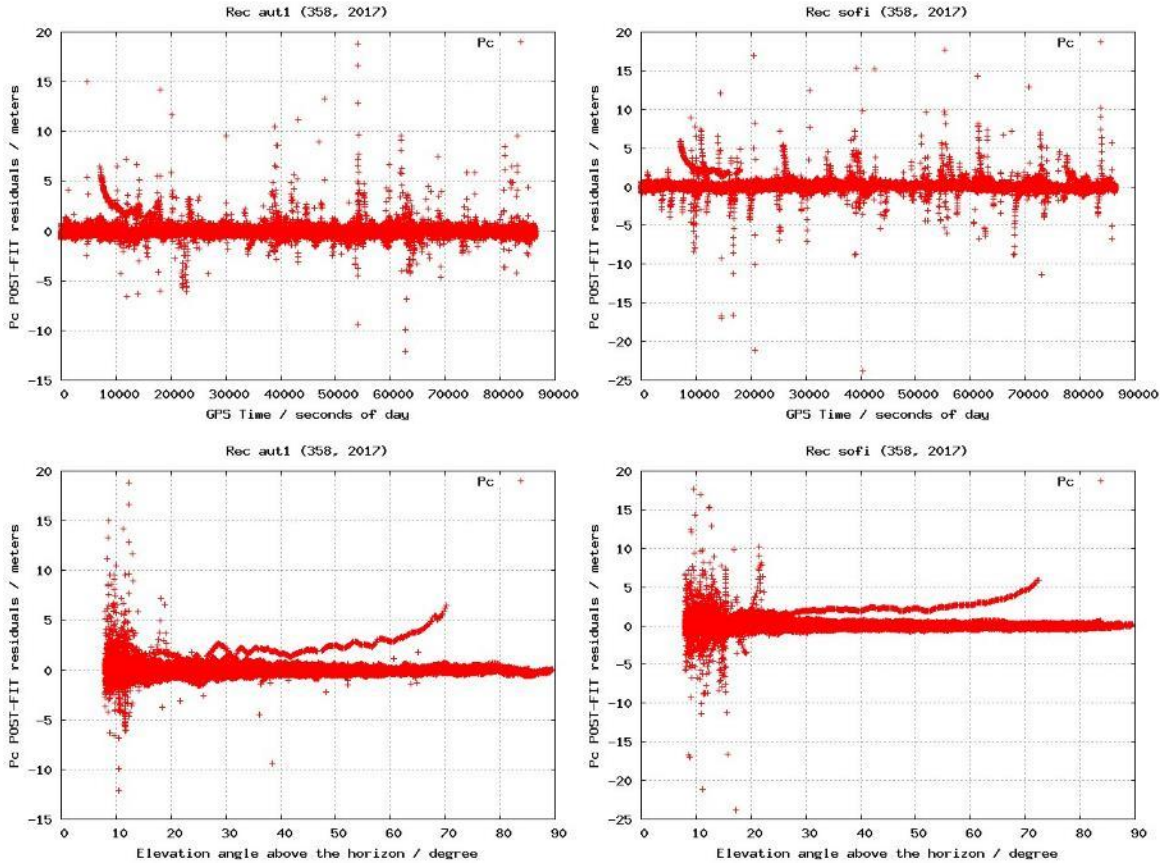

Figure 7.3 Post-fit residual for the ionospheric-free combination of the pseudoranges corresponding to the roving receiver AUT1 (first column) and the reference receiver SOFI (second column), versus time (first row) and versus elevation (second row), during day 25 December 2017.

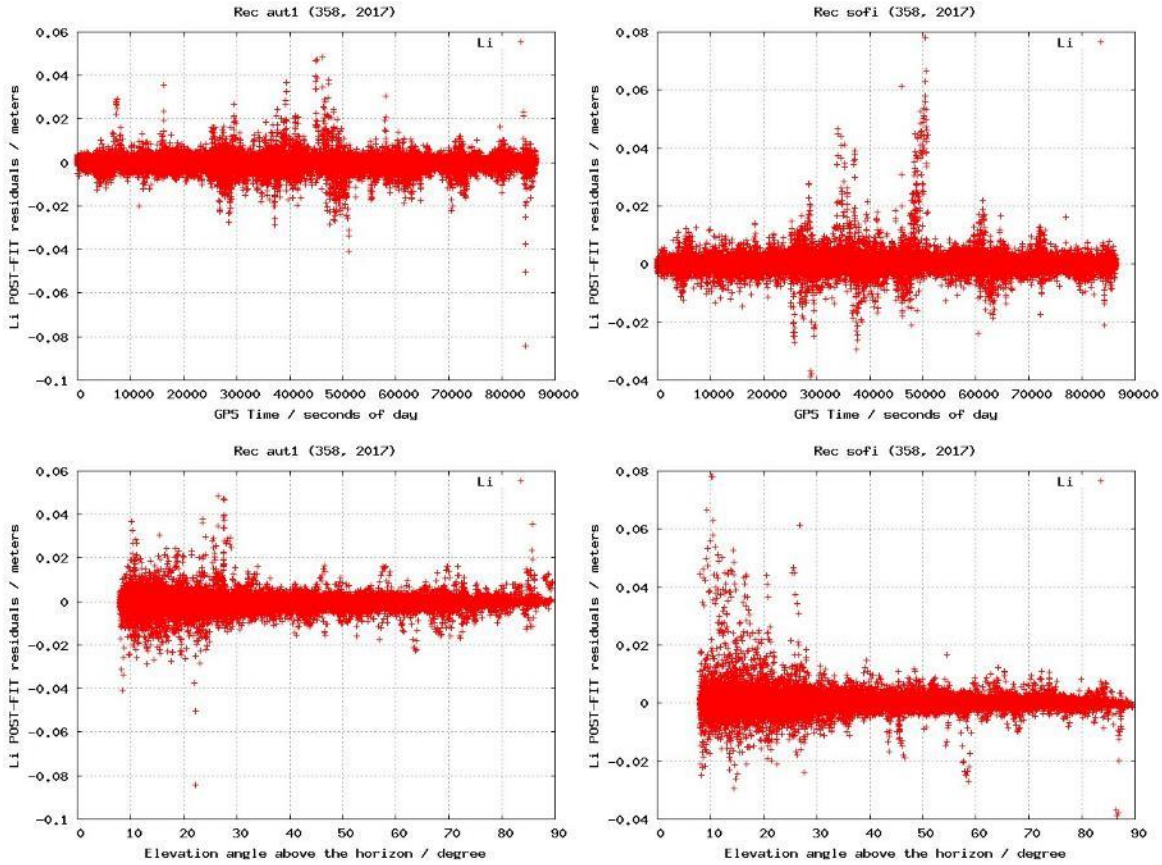

Figure 7.4 Post-fit residual for the ionospheric combination of the carrier phases corresponding to the roving receiver AUT1 (first column) and the reference receiver SOFI (second column), versus time (first row) and versus elevation (second row), during day 25 December 2017.